The Self-Assembly of Bidisperse Colloids

by

Ronald Allen LaCour

A dissertation submitted in partial fulfillment
of the requirements for the degree of
Doctor of Philosophy
(Chemical Engineering)
in The University of Michigan
2022

Doctoral Committee:

Professor Sharon C. Glotzer, Chair
Professor Nicholas A. Kotov
Professor Ronald G. Larson
Professor Ashwin J. Shahani

Ronald Allen LaCour

alacour@umich.edu

ORCID iD: 0000-0002-0572-2286

To Mom and Dad

ACKNOWLEDGEMENTS

First, I would like to thank my advisor Sharon Glotzer. You gave me lots of opportunities to do exciting work, and I learned a lot working with you and grew as a scientist. Because of you I will feel more confident wherever my next steps lead me.

I would like to thank other members of the Glotzer group, especially Timothy C. Moore and Carl Simon Adorf who provided mentorship on many different projects. In particular I would like to thank Karen Coulter, who supported me in many endeavors. I would also like to thank my collaborators, including Chris Murray, Shengsong Yang, and Emanuele Marino. Over countless meetings, I learned a lot from you.

Lastly, I would like to thank my family and friends. Mom and Dad, thanks for supporting me over the pandemic; it made my life a lot easier. Also thanks to my siblings Christalin, Kimber, and Bryan; you made my life more fun. I was fortunate to have many friends over the course of my studies. I doubt I would be here without you.

TABLE OF CONTENTS

LIST OF FIGURES

Figure

LIST OF TABLES

Table

ABSTRACT

New technologies call for the development of new materials. One new type of material with exciting electronic, magnetic and optical properties are colloidal crystals. Binary colloidal crystals, which incorporate two different types of colloidal particle into the same structure, promise opportunities in designing multifunctional materials. In this thesis we investigate the self-assembly of bidispere colloids into colloidal crystals. Despite the simplicity of such colloids, they self-assemble into diverse colloidal crystals in experiment.

The primary focus of this thesis is to address the fact that much of the experimentally reported behavior is not understood theoretically, limiting us from using simulation to guide experiments. Here we seek to improve our understanding by finding the important factors for the self-assembly of bidisperse colloids.

In the first project, we explore the influence of interaction softness on the stability of binary crystals, finding that a minimal amount of softness will destabilize several dense packings and promote the formation of experimentally observed crystals. In the second project, we demonstrate that the stoichiometry of a binary colloidal mixture can be tuned to promote self-assembly, finding that adding an excess of the smaller component can enable self-assembly. In the third project, in collaboration with Chris Murray's group at the University of Pennsylvania, we demonstrate the short-ranged attraction enables the self-assembly of binary nanoparticle superlattices, finding attraction necessary for obtaining the structures observed experimentally by our collaborators. In the fourth project, we construct a guide for the self-assembly of non-specifically interacting particles, characterizing the phases (including a quasicrystal) that self-assemble from hard sphere-like and attractive particles. In the fifth project, again in collaboration with the Murray

group, we explore the self-assembly of heterodimer nanoparticles, finding that they can self-assemble into a colloidal crystal exhibiting alignment between the atomic lattices of neighboring nanoparticles, which can lead to unique material properties.

In these projects, we uncovered many important factors for self-assembly in bidisperse systems, including interaction softness, stoichoimetry, and short-ranged attraction. In doing so, we substantially pushed forward our ability to conduct self-assembly with bidisperse colloids.

CHAPTER I

Introduction

The design of new materials is critical for technological advancements. One relatively new class of materials are colloidal crystals, which are solids composed of colloidal particles arranged in a periodic manner. A diverse array of colloids have been incorporated into these "colloidal crystals," including various types of nanoparticles[1, 2, 3, 4, 5, 6] (distinguished by having diameters in between 1 and 100 nm), polymer beads[7] and microgels[8, 9], natural silica spheres[10], and even virus particles[11, 12]. The properties of the colloidal particles in combination with their arrangement in the crystal can give rise to materials with unique electronic[13], magnetic[5, 14], and optical properties[15].

Multicomponent colloidal crystals have also been synthesized [16, 17, 18, 19, 20, 21, 22, 23, 24, 25, 26] and, like in atomic systems systems[27], tend to exhibit greater structural diversity than in single-component systems. Particularly high structural diversity has been observed in binary colloidal crystals[28], which incorporate two different types of colloids into their structures. The two types of particles can be made of different materials, which can lead to even more unique material properties[29, 30, 31, 32, 33].

Self-assembly, in which the constituents of a system organize themselves into ordered structures, is a useful way to prepare colloidal crystals from a colloidal dispersion. A key advantage of self-assembly is its simplicity. Frequently evaporation of the solvent suffices to induce self-assembly[34, 35], and evaporation of a multicomponent colloidal solution suffices to produces multicomponent colloidal crystals[22].

The structure of the colloidal crystals obtained from self-assembly depends upon the interactions between the colloidal particles and environmental conditions. Because the structure exerts a strong influence on material properties[29, 15, 30, 31, 32, 33, 36] much effort has been devoted to understanding how colloidal particles may be engineered to self-assemble into a particular structure. Simulations have played an important role in this effort, as they enable us to predict the self-assembly behavior of particles interacting with exactly specified interparticle forces, like screened electric charges[37, 38] or bonding between surface-bound strands of DNA[39, 40, 41, 42]. Furthermore, because simulations enable interactions like dipole moments and charge[43, 44] to be tuned until the experimentally observed behavior is reproduced, simulations can be used to infer the interactions of experimental colloids.

Much progress has been had in understanding and predicting the self-assembly behavior of single-component systems. These include forward studies[45, 46, 47, 42, 48] in which self-assembly is attempted with many different types of colloids, and inverse design strategies[49, 50, 51, 52] where one searches for particles that self-assemble into a particular structure. Some key successes are understanding how attractive patches[45, 53] and particle shape[47, 49] can lead to diverse self-assembly behavior.

Less progress has been had in understanding and predicting the self-assembly behavior of binary systems. There are many reports of binary colloidal self-assembly in experiment[17, 18, 19, 21, 22, 23, 24, 25, 26], but, with notable exceptions like 2-dimensional systems[54, 55] and systems in which unlike particles attract each other[39, 42], attempts to simulate the self-assembly of binary colloidal systems frequently fail to replicate experiments or self-assemble at all. This inability extends to bidisperse mixtures of particles, in which the two types of particles are distinguished by their size. Our inability to model the self-assembly behavior of even these simple particles, who exhibit diverse self-assembly behavior in experiment[18, 22, 56] indicates that we are missing key contributions to self-assembly in binary systems.

In this thesis we examine the self-assembly of bidisperse mixtures of particles, focusing on revealing the missing contributions that have stymied previous progress. In chapter II, we review how thermodynamics and kinetics are used to explain and predict self-assembly. In chapter III, we discuss the methods used in this thesis. In chapter IV, we examine the influence of interaction softness on the stability of different binary crystals, finding that a slight amount of softness can thermodynamically destablize many phases. In chapter V, we demonstrate that the stoichiometry of binary mixtures can be tuned to enhance self-assembly kinetics. In chapter VI, we, in collaboration with the Murray group at the University of Pennsylvania, demonstrate the importance of short-range interactions in the self-assembly of binary nanoparticle superlattices. In chapter VII, we present a guide to the self-assembly of nonspecifically interacting particles developed by conducting a large exploration of simulation conditions. In chapter VIII, we, again in collaboration with the Murray group, show that a nanoparticle superlattice exhibiting atomic alignment can be obtained through the self-assembly of heterodimer nanoparticles. Finally, we conclude in chapter IX by discussing our current outlook on binary colloidal self-assembly.

1.1 Definitions

We use a variety of abbreviations throughout this work. We list commons ones in Table 1.1.

Table 1.1: Abbreviations

IPL	inverse power law potential
WCA	Weeks-Chandler-Anderson potential
MD	molecular dynamics
MC	Monte Carlo
E	total energy
T	temperature
P	pressure
V	volume
μ	chemical potential
N	particle number
A	Helmholtz free energy
H	enthalpy
G	Gibbs free energy
ρ	number density; N/V
ϕ	packing fraction
ϕ_m	maximum packing fraction that a crystal can have
k	Boltzmann constant
NVT	the thermodynamic ensemble in which N, V, and T are kept constant
NPT	the thermodynamic ensemble in which N, P, and T are kept constant
Ω	microcannonical partition function
FCC	face-centered cubic crystal
BCC	body-centered cubic crystal
BNSL	Binary nanoparticle superlattice (In Ch.6 we use "nanocrystal" instead of "nanoparticle")
x_s	fraction of small particles
x_a	fraction of particles of type a
μ_F^a	chemical potential of a particles in the fluid
μ_C	chemical potential of particles in a crystal phase
σ_{ij}	length scale of interaction between two particles i and j; depends on pair potential
σ	length scale used in the simulations; typically set to σ_{LL} where L indicates large particles
ϵ	energy scale of interaction between two particles, dependd on pair potential
γ	size ratio between two particles in a binary mixture
N_L:N_S	stoichiometry of a system in terms of the number ratio of large to small particles
m	typically particle mass, but also parameter for attractive well range in Mie potential (Ch. 6)
τ	units of time; typically $\tau = \sigma(m/\epsilon)^{1/2}$
F_{LL}	intermediate scattering function between large particles
q_i	Steinhardt order parameter with $\ell = i$
$S(q)$	structure factor
s	separation between lobes in a heterodimer

CHAPTER II

Thermodynamics and Kinetics

According to second law of thermodynamics[57], the entropy of an isolated thermodynamic system cannot decrease. Thus, entropy must increase during colloidal self-assembly. In a system at constant volume, number of particles, and energy, the entropy (S) can be written as:

$$S = \frac{1}{T}\Big(E + PV - \sum \mu_i N_i\Big) \tag{2.1}$$

where T is the temperature, E is the energy, P is the pressure, V is the volume, μ_i is the chemical potential of species i, and N_i is the number of particles of species i. Because entropy can only increase, an isolated system tends towards the state with the highest entropy.

Specifying E and V is generally not the most convenient way to parameterize a system. Instead, if the more convenient variables P and T are specified, the system tends towards the state with the lowest Gibb's free energy:

$$G = E + PV - TS. \tag{2.2}$$

G accounts for the entropy of the environment (which may change due exchanging energy and volume) in addition to the entropy of the system. G also isolates the chemical potential of different species, as can be shown by substituting equation 2.1 into 2.2:

$$G = \sum \mu_i N_i. \tag{2.3}$$

Statistical mechanics explores how the properties and interactions of individual particles (like atoms or colloidal particles) give rise to macroscopic quantities like S and P. Specifically, S is related to the number of microstates (unique configurations of particles) that a system can take:

$$S = k \ln \Omega \tag{2.4}$$

where k is Boltzmann's constant and Ω is the number of microstates. This formulation provides another understanding of the second law: the system moves towards macrostates (the macroscopic state of system; *e.g*, gas or liquid) with more microstates. For example, if in an isolated system at -1 °C there are 10^{10} microstates associated with liquid water and 10^{500} associated with ice, ice has a higher entropy than the liquid. If we assume that each microstate is equally probable (as is done for isolated systems in equilibrium statistical mechanics), we conclude that the system is $10^{500}/10^{10} = 10^{490}$ times likelier to be ice than liquid. The most probable phase is deemed the equilibrium phase and "thermodynamically stable." The most probable phase at constant T and P is computed similarly, except the probability of each microstate must be weighted by the appropriate Boltzmann factor[58].

In colloidal systems, the initial dispersion is analogous to a conventional fluid phase, and the colloidal crystal is analogous to a solid phase. Thermodynamic calculations (see chapter III) enable precise estimates at what density and temperature the crystal becomes favored over the dispersion. Multiple solid phases can exist, each distinguished by their own crystal structure. By computing the G of the competing solid phases, we can determine which is the equilibrium phase. For these reasons, thermodynamics underpins many methodologies for designing particles with desirable self-assembly behaviors. These methodologies include forward explorations of parameter space[59], in which the equilibrium structure is evaluated for many types of particles, and inverse techniques like digital alchemy[49], in which the particles who possess the highest entropy for a given structure is sought.

However, deviations from equilibrium predictions are often observed. For example, Lennard-Jones particles can self-assemble into a BCC phase under conditions where FCC is the stable phase[60], and some liquids form glasses instead of equilibrium solid phases[61]. These are not violations of the second law of thermodynamics, because there is no upper limit on the time required to reach the equilibrium phase and thus non-equilibrium phases may persist far longer than the time scales of interest. Additionally, there is no guarantee that a system first transitions into the equilibrium phase; another non-equilibrium phase may form instead[60, 62, 63]. These non-equilibrium phases are called "metastable," and their persistence hinders methodologies using thermodynamics to predict self-assembly behavior.

The rate at which phase transitions occur is governed by their reaction kinetics. The liquid-solid transition underpinning colloidal self-assembly generally begins with nucleation, in which a small nucleus of the new phase forms and grows within the old[64]. The nucleation rate depends strongly on the degree of supercooling. At low supercooling, nucleation is slow due to large energy barriers separating the phases, but at high supercooling it can be slowed by low particle mobility because high supercooling tends to correspond to high pressure or low temperature. Therefore an optimal supercooling exists, intermediate between low and high, where the nucleation rate goes through a maximum. In many systems, nucleation is rapid enough to occur at supercoolings far away from the maximum; however, in binary colloidal mixtures, where self-assembly may take minutes to months[18, 26], proximity to the maximum can be a necessity.

Throughout this thesis, reaction kinetics play a role in determining the phases we get from our self-assembly simulations. In Chapters V and VI, we will use the degree of supercooling to explain why the self-assembly kinetics are affected by system stoichiometry and interparticle attractive forces.

CHAPTER III

Methods

In this thesis we use a wide array of computational methods to characterize the behavior of colloidal particles. These include molecular dynamics simulations (MD), Monte Carlo simulations, order parameter calculations, and free energy calculations. We discuss these in this chapter, but include more chapter-specific methods within the respective chapter.

According to Newton's second law, a particle's acceleration equals the force applied to it divided by its mass. Therefore, if we know the force on every particle in a system, we can compute the particles' future trajectory. In many body systems, we must numerically solve for the trajectory, as no analytical solution exists. This is the basis of molecular dynamics. In this thesis, we specify force fields between colloidal particles in terms of a pair potential. We use the HOOMD-blue simulation toolkit to conduct MD simulations[65, 66].

According to equilibrium statistical mechanics, the probability of a given microstate is proportional to $e^{-E/kT}$, where E is the microstate's energy as determined by a given pair potential. Using Monte Carlo with the Metropolis-Hastings algorithm[67], one can draw a chain of system configurations where the probability of each is proportional to $e^{-E/kT}$. If the chain is long enough, it represents the equilibrium distribution of system configurations, and thus can be used to compute quantities like pressure and energy. This is the basis of molecular simulation with Monte Carlo. Importantly, Monte Carlo

provides a way to simulate hard (impenetrable), anisotropic particles, and we do so here using HOOMD-blue.

To determine whether self-assembly is occurring, one must be able to classify particles in the simulation as belonging to a fluid phase or a solid phase. We do so using Steinhardt order parameters[68]. They are constructed for each particle by evaluating several spherical harmonics over the relative positions of that particle's neighbors and then combining the spherical harmonics in a rotationally invariant fashion. Different coordination shells return different values of the order parameters. Because solids tend to have very specific coordination shells, Steinhardt order parameters can distinguish solid-like particles from the fluid. An important application is tracking a solid's growth with time. We use the *freud* software package[69] to compute Steinhardt order parameters.

In Chapter II, we discussed the usefulness of the Gibb's free energy (G) in predicting phase behavior. Using thermodynamic integration, we can compute changes in G for a system not undergoing a discontinuous phase transition:

$$\Delta G = \int_{P_1}^{P_2} V dP \tag{3.1}$$

$$\Delta(G/T) = -\int_{T_1}^{T_2} \frac{H}{T^2} dT. \tag{3.2}$$

If the Gibb's free energy at any pressure and temperature is known, we can use equations 3.1 and 3.2 to find it at any other temperature and pressure.

Thus one needs a reference state where the free energy is known for each phase. For fluid phases, the G of the ideal gas is a suitable reference state:

$$G^{ig} = kT \ln \frac{P\lambda}{kT} \tag{3.3}$$

where λ is the de Broglie wavelength. The value of λ does affect phase behavior because it is equal for all phases.

For solid phases we can use the Frenkel-Ladd method[70] to compute free energies. With Frenkel-Ladd, we compute the difference in free energies between an Einstein crystal, whose free energy is analytically calculable, and a real solid. Here we use a variant

called the Einstein molecule method[71], where the position of a single particle is fixed instead of the solid's center of mass like in the original formulation. More details can be found in other references[67, 71].

The free energy of each phase can be used to construct phase diagrams. Doing so in single-component systems is straightforward because the equilibrium phase at any given P and T is simply the one with the lowest G. Phase coexistence occurs at the T and P where the G of different phases are equal. Once the phase diagram is known for constant temperature and pressure, it can be mapped to other representations (*e.g.*, T and V) by computing values of the new coordinates at the coexistence lines. We note that, due to Gibb's phase rule[57], coexistence lines map to coexistence regions when going from constant P to constant V.

Phase diagrams in binary systems are complicated by stoichiometry, which is typically given as x_s, the fraction of small particles. Crystalline phases typically have a particular stoichiometry (*e.g*, the x_s of NaCl is 1/2), and G may be minimized by the coexistence of two phases. If both phases are solids, we can determine the stable combination of phases by looking for the pair that minimizes G, but the situation is more complicated for fluid-solid coexistence. In this case we can compute the chemical potential of individual species a and b in the fluid:

$$\mu_F^a = \mu_F - x_b \frac{\partial G}{\partial x_b} \tag{3.4}$$

$$\mu_F^b = \mu_F + (1 - x_b) \frac{\partial G}{\partial x_b}. \tag{3.5}$$

where μ_F is the chemical potential of a fluid with b particle fraction x_b.

A fluid is in equilibrium with a solid if

$$\mu_C = (1 - x_c)\mu_F^a + x_c \mu_F^b \tag{3.6}$$

where μ_C is the chemical potential of the solid and x_c is the fraction of b particles in the solid structure.

In addition to allowing us to compute phase diagrams, our free energy calculations provide us with $\Delta\mu$, a measure of the degree of supercooling. In later chapters of this thesis we use $\Delta\mu$ to explain why varying system parameters can make self-assembly more or less difficult.

Throughout this thesis we used Ovito[72] to visualize our systems and *signac*[73] for data and workflow management.

CHAPTER IV

The Influence of Softness on the Stability of Binary Colloidal Crystals

The contents of this chapter were adapted from "Influence of softness on the stability of binary colloidal crystals.", R. A. LaCour, C. S. Adorf, J. Dshemuchadse, S. C. Glotzer. *ACS nano* (2019)[59].

4.1 Introduction

Binary systems of spheroidal colloids self-assemble into many more colloidal crystal phases than do unary systems of the same particles. [16, 18, 22, 74, 75, 56] These phases, which typically have structures analogous to intermetallic or ionic crystals, are interesting for their structural diversity and promising functionalities. [13, 32, 31, 33, 35] The particles may differ in composition, charge, size and shape, each of which influences their self-assembly behavior and potential applications. Models based on hard particle packings are often invoked to explain experimentally observed phases, with varying degrees of success[76, 77, 78, 79, 56, 80]. Failure of packing models to explain observed phases – in particular for particles with screened electrostatics[81, 17] and/or ligand shells,[82, 56] could be due to entropic forces [83], or because the interparticle interaction in those systems is considerably softer than the excluded volume (hard particle) interaction considered by packing models[84, 85, 86, 26]. While the role of entropy has been widely considered[87, 88, 89, 90, 74, 47, 83] the effect of interaction softness on self-assembled colloidal crystal phases has received less attention[91, 92, 90, 86, 93], especially for binary

systems.

Here we examine the enthalpic influence of softness on the colloidal crystal phase behavior of binary mixtures of spherical particles of two different sizes interacting *via* an additive inverse power law (IPL) potential. We investigate a much wider range of softness than has been reported to date by tuning the exponent of the IPL to vary the distance over which the repulsive interaction falls off from the surface of a particle. Large exponents describe a very rapid decay (and thus "harder" interparticle interaction) while small exponents describe a slow decay (becoming a $1/r$ decay with an exponent of one). To isolate the role of softness from other effects, we perform zero-temperature enthalpy calculations (which disregard entropy) to determine the ground state stability of different phases. We find several experimentally observed phases that fail to be described by packing models; instead, we show that these phases – which have a small number of interparticle contacts and a tendency for icosahedral local order – are stabilized by particle softness. We also use finite temperature free energy calculations to probe the influence of temperature for a few phases, generally finding agreement with our ground state calculations with the exception of a recently reported dense packing phase.[94] We further find that a small amount of softness (described by a remarkably large IPL exponent) can influence phase behavior away from that describable by packing models. These deviations from hard sphere packing behavior partially explain why the packing fractions of different phases do not solely determine their self-assembly behavior, as is commonly invoked. We characterize the degree of softness necessary to destabilize any binary phases relative to phase-separated unary phases for the additive IPL potential, which has relevance for the modeling of binary systems and our understanding of the interaction between different species of particles. Finally, we relate our results to recent experimental reports, elucidating how repulsive forces contribute to the formation of particular structures observed in experiments.

4.2 Model

The use of packing models to understand the behavior of condensed phases stems in part from the ground state of the hard sphere model, in which particles are prohibited from overlapping; the ground state is the phase with the highest packing fraction at infinite pressure. Throughout this work we use the term ϕ_m to describe the maximum packing fraction obtainable by hard spheres in a particular structure. The binary hard sphere model, in which the particles can be one of two different sizes, describes the phase behavior of many binary colloidal systems, as shown by free energy calculations.[87, 95, 15, 90] However, no real particle is perfectly hard,[84, 85] and in many cases—particularly the self-assembly of metal and semiconductor nanoparticles—experimental results differ from binary hard sphere predictions.[17, 75, 74, 96, 22]

In contrast to hard particle models, softly repulsive pair potentials in binary systems have received much less consideration. In 2009, Hynninen *et al.* found the CsCl and Laves phases to be stable for a particular binary Yukawa potential.[90] In 2015 and 2016, Travesset and Horst found several more binary phases to be stable for a binary IPL model. [86, 93] However, the Laves phases were the only binary structures found to be stable when the potential was additive (where unlike particles interact as though their size is the average of the two particles); observing other phases required reducing the repulsion between unlike particles. Here we ascertain how softness affects crystal stability by considering a much wider range of softness.

We studied the IPL potential in Equation 4.1; its parameterization for binary systems is shown in Figure 4.1.

$$U_{ij} = \epsilon \cdot \left(\frac{\sigma_{ij}}{r_{ij}}\right)^n \tag{4.1}$$

The quantity n is related to the hardness of the particles, σ_{ij} governs their size, and ϵ determines the units of energy. The quantity γ in Figure 4.1 gives the size ratio between large and small particles. The potential is specified to be additive as is physically accurate

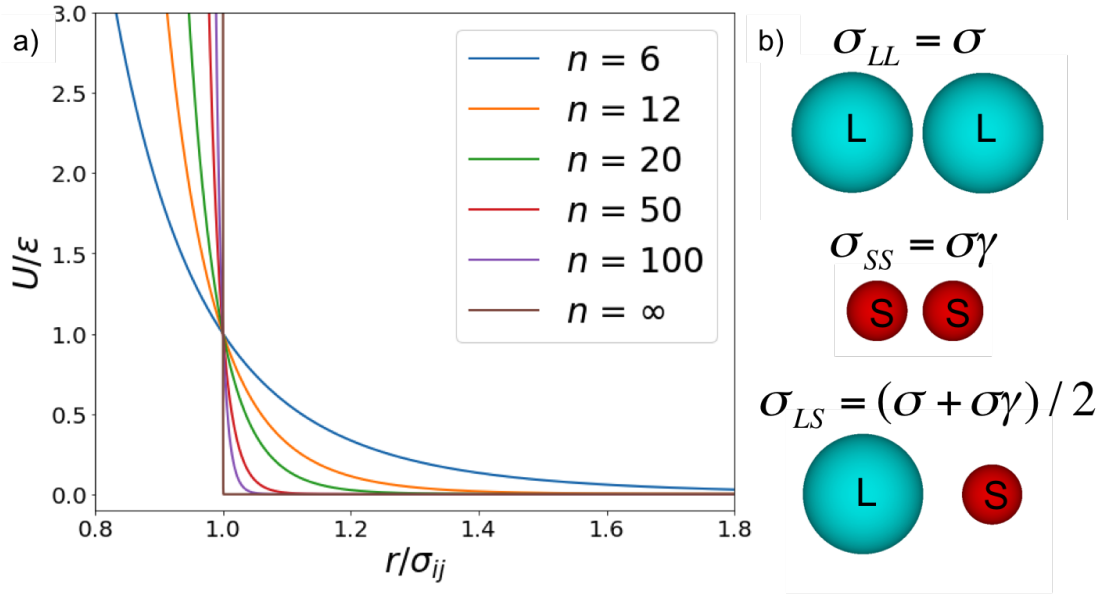

Figure 4.1: a) Plots of the IPL model for different values of n and b) the effective size of different types of particles. The pair potential is given by Equation 4.1 and is plotted over r/σ_{ij}—the distance between two particles i and j divided by the average size of the particles. The large and small particles are represented by "L" and "S", respectively. The quantity σ is the size of the large particles, and γ is the size ratio between the small and large particles. Unlike particles interact as though they are the average size of the two particles.

in the limit of n approaching ∞. For $n = \infty$, we obtain the binary hard sphere model; for $n = 1$, we obtain the potential describing Coulombic repulsion.

The phase behavior of our model depends upon n, γ, the stoichiometry, and a variable incorporating both the pressure and temperature. Note that, for the IPL model, giving ϵ as ϵ_{ij} to depend on the types of particles interacting does not increase the generality of the potential as any variation in ϵ_{ij} can also be accounted for through variation in σ_{ij}. The ability to write the temperature and pressure of the IPL model as one variable results from the its unique thermodynamic scaling properties and is not possible for most pair potentials.[91] We review these scaling properties in section 4.6.2. By constraining $T = 0$, we are then left with the aforementioned three parameters: n, γ, and the stoichiometry of the system. We will present two slices of the model's phase diagram at constant stoichiometry and four slices at constant n.

We analyze the phase behavior of our potential at constant pressure because the stability of densely packed phases for hard spheres at higher pressures can be justified on

the basis of enthalpy alone. The stability of these phases is often understood in terms of free volume theory, according to which particles in the densest packing phases will have more volume available to them than in other arrangements, and thus be entropically favored. However, at constant pressure, the Gibbs free energy in the limit of either zero temperature or infinite pressure can be written as:

$$\lim_{P\to\infty} G = \lim_{T\to 0} G = PV \tag{4.2}$$

Note that the equivalence of these two limits follows directly from the well-known thermodynamic scaling ($P\sigma^3/kT$) between pressure and temperature in hard particle systems (see section 4.6.2). Densely packed phases will minimize V, motivating the idea that they are the ground states of the system. For completeness, we give two more rigorous proofs that the densest packing phase has minimal free energy in the limit of zero temperature at finite pressure: in section 4.6.1 we take the limit of infinite n in our equation for the enthalpy of soft spheres, and in Section section 4.6.2 we take the zero temperature limit of our NPT partition function. Thus, we should expect (and do observe) that densely packed phases will arise in constant pressure ground state calculations of the enthalpy for our potential as n approaches ∞.

The IPL model exhibits thermodynamic scaling of the form $\frac{P\sigma^3}{\epsilon}/(\frac{kT}{\epsilon})^{(3/n+1)}$.[97] Note that as n approaches ∞, the scaling reduces to that of hard spheres, and that the $P \to \infty$ behavior is equivalent to that of $T \to 0$. Likewise, one would expect the specific value of the pressure to not affect phase behavior at $T \to 0$ because the scaling term diverges in that limit regardless of P. Indeed, we find this in our derivation of an equation for $H(T = 0, P)$ in section 4.6.1.

Although the IPL model does not perfectly describe colloidal interactions, we believe it is sufficiently general to account for the behavior of many colloids. In fact, the effective n for several colloidal polymer particles have been previously estimated[84, 85, 98] and are often similar to the values of n we investigate. In other binary self-assembly experiments, the nature of the interparticle forces during self-assembly is less clear,[99] but similari-

ties between the self-assembled structures formed from many metal and semiconductor nanoparticles and those formed with other softly repulsive particles suggest that repulsive forces play a key role in their assembly as well. Likely the most notable way in which our model deviates from other notions of softness is our neglect of 3-body interactions, such as the deformation of two particles in contact influencing the way they act with a third particle (which has been implicated as important for understanding the self-assembly of certain ligand-functionalized nanoparticles[56]). Many colloidal particles, such as those in charge-stabilized or hard sphere-like colloids, will be less deformable and thus more likely to correspond to our model.

Travesset and Horst previously investigated the binary IPL potential at $n = 12$ and $n = 6$, while varying the additivity of the potential.[86, 93] Here we investigate n at values from 6 to 100, a range inclusive of many experimental particles, as shown in a recent analysis by Royall *et al.*[85] We keep our potential additive to maintain correspondence with the hard sphere limit.

4.3 Results/Discussion

In Figure 4.2 we present phase diagrams calculated at stoichiometries of $x_S = 1/2$ and $x_S = 6/7$ in terms of γ and n. Due to the thermodynamic scaling properties of the IPL model, its ground state phase diagram also corresponds to its infinite pressure phase diagram and exhibits no pressure dependence (see section 4.6.1). We did not evaluate the enthalpy of any dense unary sphere packings other than the face-centered cubic (FCC) crystal due to their great structural similarities (*i.e.*, consisting of hexagonal layers stacked upon each other); we expect them all to have practically identical enthalpies at most n examined. Visualizations of several stable structures without equivalents in the Inorganic Crystal Structure Database[100] (ICSD) are included in section 4.6.3.

Regions of phase stability were calculated by finding the combination of phases that minimizes the enthalpy for a given stoichiometry. Unless the stoichiometry of a phase

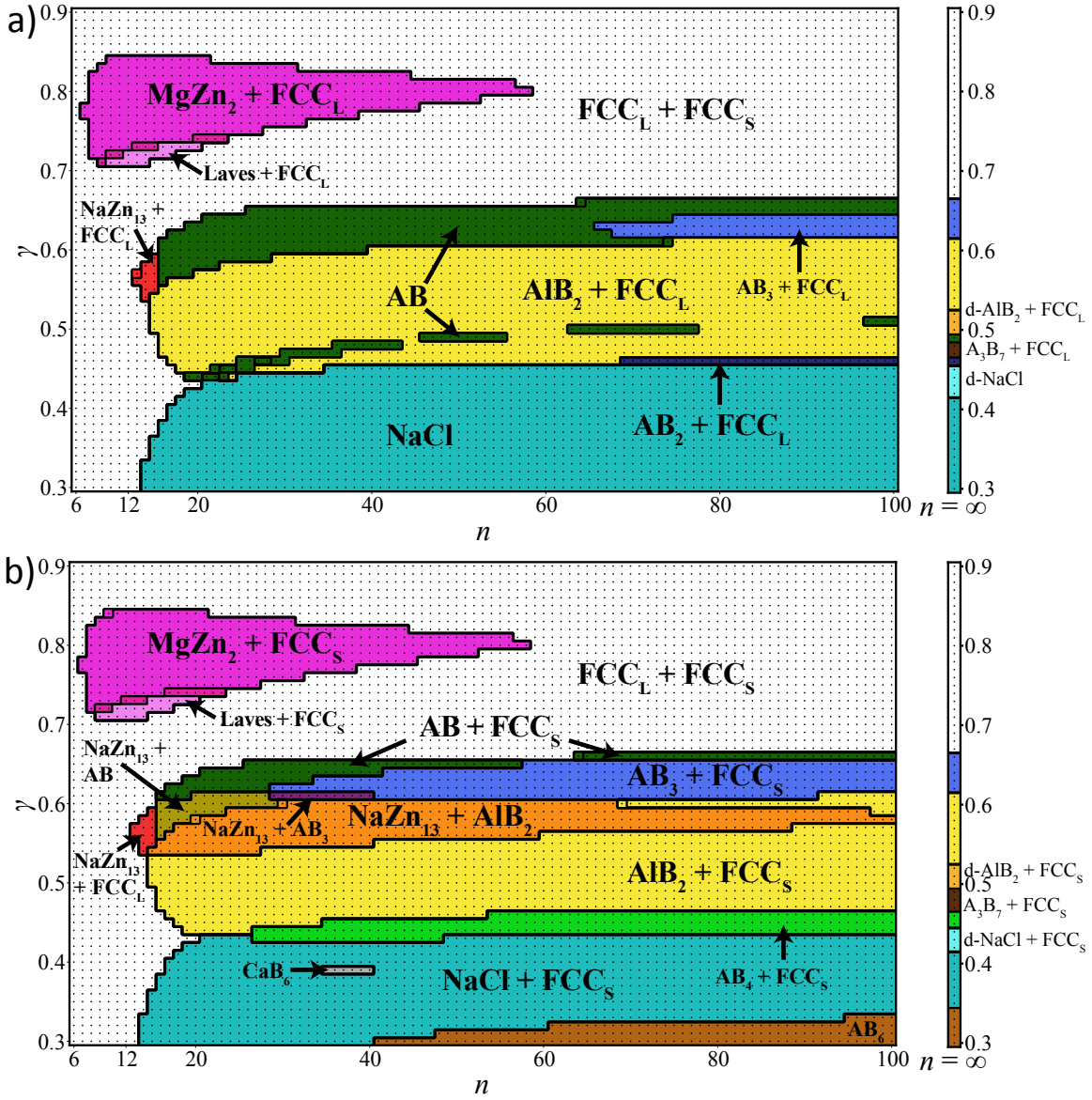

Figure 4.2: Phase diagrams calculated at stoichiometries of a) $x_s = 1/2$ and b) $x_s = 6/7$ for the binary IPL model. The diagrams are given in terms of particle size ratio γ and hardness n. We show 95 values of n spanning from 6 to 100, and 61 values of γ spanning from 0.3 to 0.9. The $n = \infty$ slice to the right of each plot was calculated from the densest packings. The equilibrium state consists of two phases unless the stoichiometry of a phase is identical to that of the system (*e.g.*, CaB_6 for $x_S = 6/7$); the colors indicate a region corresponding to a specific set of equilibrium phases. In regions denoted "Laves + FCC_S", the differences in enthalpy between the different Laves phases were very small. If the difference in enthalpy between two phases was $< 0.001\%$, the point was colored to indicate the presence of the phase nearest in stoichiometry to that of the entire phase diagram. In every region containing "NaCl", the difference in enthalpies between NaCl and NiAs was also $< 0.001\%$. The black dots indicate points at which basin hopping runs were performed.

matches the system's stoichiometry (*e.g.*, NaCl for $x_S = 1/2$), the enthalpy at each point in the phase diagram is minimized by two phases: one with a stoichiometry greater than that of the system, and one with a stoichiometry less than that of the system. Phases are taken to be in the thermodynamic limit and thus no attempt was made to account for interfaces between coexisting phases. The specific enthalpy for coexisting phases a and b was calculated from the standard thermodynamic formula as $x_a H_a + x_b H_b$, where x_a and x_b are determined through application of the lever rule to the natural stoichiometry of each phase a and b and the global stoichiometry of the system. We examined every possible combination of our candidate phases to determine the pair with the lowest enthalpy.

The phases present at $n = \infty$ correspond to the most densely packed combination of phases at the particular γ and stoichiometry obtainable with our set of candidate structures. With the exception of a densely packed phase we discovered, we generated the $n = \infty$ regions from the work of Hopkins *et al.*[101, 102] and Filion *et al.*[103], who both analyzed the densest packings of binary sphere systems. We denote structures with no clear atomic counterpart by A_xB_y, with x and y giving the stoichiometry. Certain structures that appear on Hopkins *et al.*'s phase diagram fail to appear on ours because the region of size ratios over which they are the densest packing is smaller than the resolution of our phase diagram (0.01), but we still examined the stability of these phases for finite n at the size ratios we did investigate. AB_4 is the aforementioned phase discovered to be a densely packed phase over the course of this work. The regions denoted d-NaCl and d-AlB_2 contain versions of NaCl or AlB_2 slightly distorted from their cubic or hexagonal symmetry into orthorhombic or monoclinic crystals, respectively, to have larger ϕ_m. Densest packing structures are also common at $n = 100$. A notable exception is A_3B_7 (a slightly symmetrized version of a structure reported by Hopkins *et al.*[102]), which is not present for $n \leq 100$, despite being the densest packing for $\gamma = 0.47$.

For $n \leq 100$, we found 11 equilibrium phases. Seven of these correspond to experimentally observed phases[16, 18, 22, 104, 74, 75, 56]: FCC, NaCl, AlB_2, $MgZn_2$, AB_4, CaB_6,

and $NaZn_{13}$. The four remaining phases are known to pack very densely.[105, 101, 102] AB_6 is a distorted version (from cubic to orthorhombic) of the bcc-AB_6 phase observed experimentally.[106] AB_2 is an orthorhombic phase with space group symmetry $Cmc2_1$ (no. 36). AB is an orthorhombic phase with space group symmetry $Pmnc$ (no. 62) and is particularly interesting for the high γ at which it appears. AB_3 is an orthorhombic phase with space group symmetry $Pmmn$ (no. 59).

In general, lower symmetry sets of space groups and Wyckoff sites are capable of producing multiple distinct structures through variation of their degrees of freedom. For example, a structure in space group $Pmnc$ (no. 62) with both the large and small particles in Wyckoff sites $4c$ will become the much higher symmetry structure NaCl for particular values of the free parameters and can be converted into several other densely packed structures for other values;[105] slight variations in the values will produce slightly distorted structures. In this manner our basin hopping procedure enabled us to search thousands of structures, including slightly distorted versions of common structures like NaCl. Thus, while it is likely that we missed some structures, we think enlarging our search space will not significantly alter the conclusions drawn in this paper.

4.3.1 Variable Stoichiometry Phase Diagrams

In Figures 4.3 and 4.4, we plot phase diagrams at constant n but variable stoichiometry and particle size ratio. The values of n considered are 20, 40, 60, and 80. These phase diagrams were generated in a manner similar to those in Figure 2: discrete values of the parameters were selected and the combination of phases resulting in the minimum enthalpy for those values were determined by comparing all possible combinations. Because we only consider the possibility of crystals of constant stoichiometry (as opposed to liquids and solid solutions), every region will contain two phases bounded by the x_s of the phases present within the region. However, we observe deviations from this for the AB + FCC_L region of our phase diagrams in Figure 3, whose enthalpy is extremely similiar to the AlB_2 + FCC_L region.

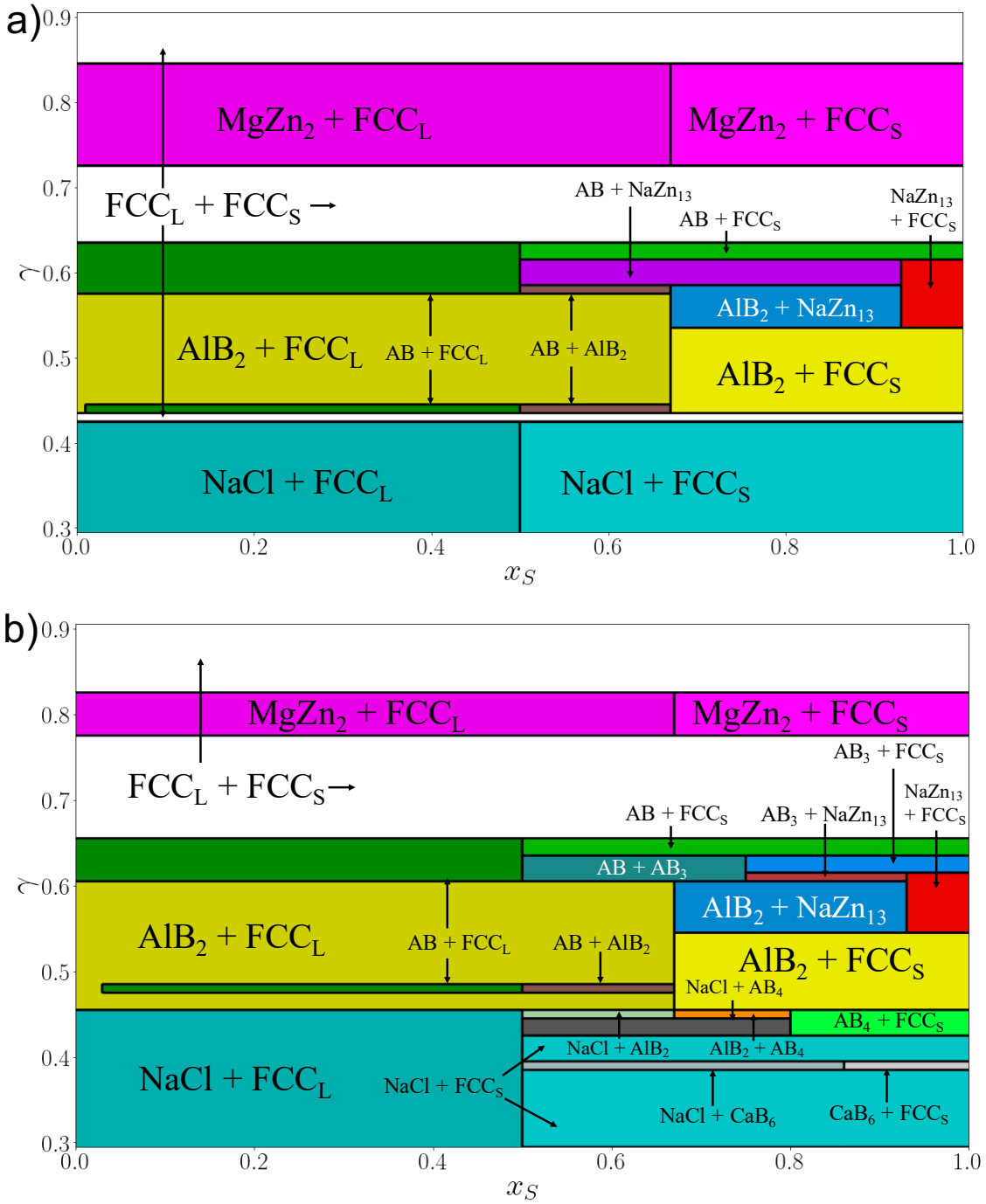

Figure 4.3: Phase diagrams calculated at n of a) 20 and b) 40 for the binary IPL model. The diagrams are given in terms of particle size ratio γ and concentration of small particles, x_s. We use a resolution of 0.01 in determining the phase boundaries with respect to both γ and x_s. The difference in enthalpy between the equilibrium phases and competing combinations of phases is generally $> 0.001\%$, with the only exceptions being the differences between $MgZn_2$ and the other Laves phases, the difference between AB + FCC_L and AlB_2 + FCC_L at $\gamma = 0.48$, and the difference between any region containing NaCl and an equivalent region containing NiAs instead.

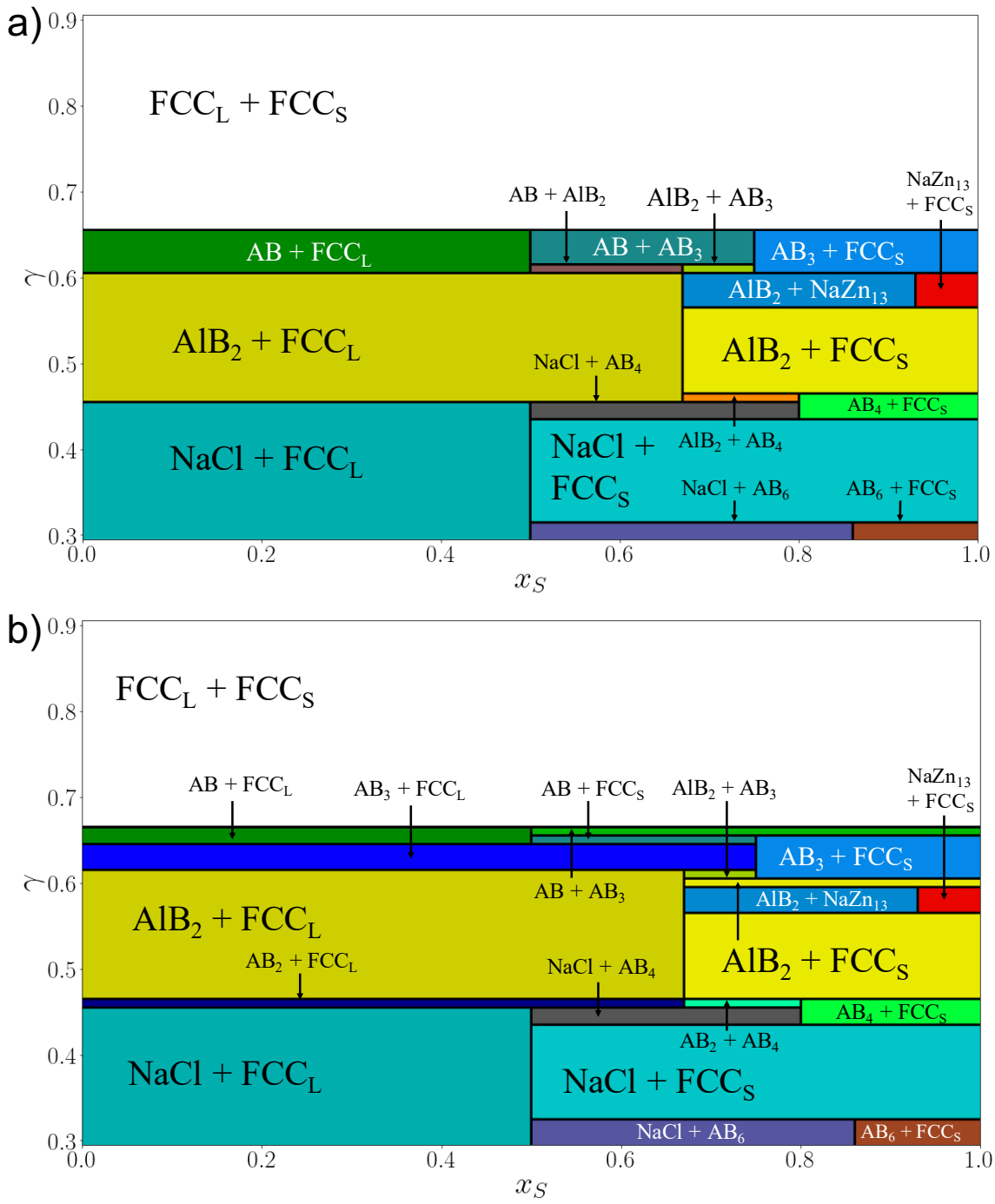

Figure 4.4: Phase diagrams calculated at n of a) 60 and b) 80 for the binary IPL model. The diagrams are given in terms of particle size ratio γ and concentration of small particles, x_s. The difference in enthalpy between the equilibrium phases and competing combinations of phases is generally $> 0.001\%$, with the only exception being the difference between any region containing NaCl and an equivalent region containing NiAs instead.

Although Figures 4.3 and 4.4 contain only phases present in Figure 2 (we chose the slices in Figure 2 such that they would contain at least a small region of every phase we found to be stable), we plot them to more clearly illustrate the influence of stoichiometry and to inspire experimentalists to test our predictions. Of course, these thermodynamic calculations will not account for experiments involving non-equilibrium phenomena or polydispersity, such as the assembly of more than 3 different superlattices from a single batch of nanoparticles[75] or heterogeneous effects, like the formation of wetting layers between different superlattices,[104] but should be a guide for the behavior of such particles under certain ideal conditions.

4.3.2 Influence of Temperature

An immediate concern for our phase diagram is how well our our ground state calculations reproduce actual assembly behavior at finite temperatures. Ideally, we could use direct self-assembly simulations to determine the phase behavior of our systems, in which we cool down a simulation of the fluid until we observe nucleation of the solids. Such methods provide relatively unambiguous determination of the preferred solid configuration of a particular set of particles, eliminating the need to examine the stability of other solids. However, in binary systems of mutually repulsive particles, the slow assembly kinetics often render such simulations computationally infeasible. [107, 108, 109] This is less of an issue for experiment, in which the timescales and number of particles are typically orders of magnitude larger than currently possible with computation. This difficulty has resulted in equilibrium calculations[87, 95, 15, 90] providing much of our basic understanding of self assembly in such systems. We do note two recent papers where binary assembly was observed for mutually repulsive particles by using specialized Monte Carlo techniques with particle swaps[109] or, intriguingly, tuning the softness of the particles.[110] We discuss possible influences of kinetics on self-assembly structure in the Experimental Relevance section.

More tractable is the issue of how increasing the temperature changes the relative free

energies of different structures. While the ground state phase is often predictive of finite temperature behavior, several cases exist in the literature in which raising temperature changes the preferred solid structure.[111, 38] As self-assembly generally occurs at higher temperatures, and large energy barriers may prevent solid-solid phase transitions at low temperature, finite temperature free energies should be more predictive of actual behavior.

In Table 4.1 we present the absolute Gibbs free energies of several structures for five points in our phase diagram, computed from a variant of the Frenkel-Ladd method.[70, 71] We focus on less hard n between 12 and 40, where we see several experimental structures on our phase diagram. We examined G at a range of pressures using thermodynamic integration of pressure-volume data, but present it only for the lowest pressure (least supercooled) in Table 4.1. We note that our calculations are unable to account for phase behaviour all the way to the fluid-solid coexistence due to the lack of a comprehensive equation of state for the binary IPL fluid; instead we were limited by the melting point of an FCC crystal of the small particles.[112] These points were chosen to test the stability of more unusual structures at finite temperatures. $CaCu_5$ and bcc-AB_6 are the only two structures not mentioned previously; their symmetry and Wyckoff sites are given in Table 2. The values in parentheses correspond to the standard deviation$\cdot 10^3$ across three independent sets of simulations.

The most stable structures are generally in line with those for the ground states, with a deviation only being observed in once case. For $n = 40$ and $\gamma = 0.6$, AB_3 changes from being the ground state to being less favorable than multiple other structures at finite temperatures, which we discuss in our Experimental Relevance subsection. Our free energy calculations also provide evidence that temperature will not destabilize the AB, AB_4, and CaB_6 phases.

Naturally, we expect our phase diagram to be most relevant for systems under high pressure and low temperature. From literature results on the free energies of binary hard sphere systems, we can anticipate other changes to our phase diagram at high tempera-

Table 4.1: Free Energies of Different Structures at $kT/\epsilon = 1$, $x_s = 6/7$

γ	n	$P\sigma^3/kT$	Structures	G/kT	Ground State?
0.39	35	203	CaB_6	38.729(15)	Yes
0.39	35	203	NaCl + FCC_S	38.806(2)	No
0.39	35	203	FCC_L + FCC_S	39.601(1)	No
0.39	35	203	bcc-AB_6	39.924(4)	No
0.43	40	151	AB_4 + FCC_S	33.673(3)	Yes
0.43	40	151	AlB_2 + FCC_S	33.878(3)	No
0.43	40	151	NaCl + FCC_S	33.906(3)	No
0.43	40	151	FCC_L + FCC_S	34.264(4)	No
0.6	20	56	AB + $NaZn_{13}$	23.828(2)	Yes
0.6	20	56	FCC_L + $NaZn_{13}$	23.850(1)	No
0.6	20	56	$CaCu_5$ + $NaZn_{13}$	23.893(3)	No
0.6	20	56	AB_3 + $NaZn_{13}$	24.084(2)	No
0.63	40	48	AB + FCC_S	22.445(3)	No
0.63	40	48	FCC_L + FCC_S	22.489(4)	No
0.63	40	48	$CaCu_5$ + FCC_S	22.491(3)	No
0.63	40	48	AB_3 + FCC_S	22.527(4)	Yes
0.63	40	48	FCC_L + $NaZn_{13}$	22.5363(1)	No
0.81	12	31	$MgZn_2$ + FCC_S	24.108(5)	Yes
0.81	12	31	FCC_L + FCC_S	24.159(3)	No

tures. In particular, we would expect the region over which the Laves phases are stable to extend all the way to $n = \infty$, but over less size ratios at higher n.[90] We also expect that $NaZn_{13}$ would be present all the way to $n = \infty$.[87] Systematically mapping out their (and the other phases') region of stability would require a comprehensive equation of state for the binary IPL fluid.

4.3.3 Minimization of Contacts

The variation in phase stability with n and γ shown in Figure 4.2 necessarily results from the local environments of each type of particle in the structure. Considering that our pair potential is purely repulsive, low energy (ground state) structures would seem to be those that minimize the number of contacts between particles. However, at $n = \infty$, the densest packing structure becomes favored regardless of the number of interparticle contacts, so ϕ_m obviously plays a role as well (despite not being directly involved in our calculations), and we find the structures stabilized by softness to have both high ϕ_m and a low number of contacts. The importance of having a high ϕ_m for soft particles comes from its correspondence with the nearest interparticle distance. When comparing two structures at constant number density, the nearest contact distance (defined here as

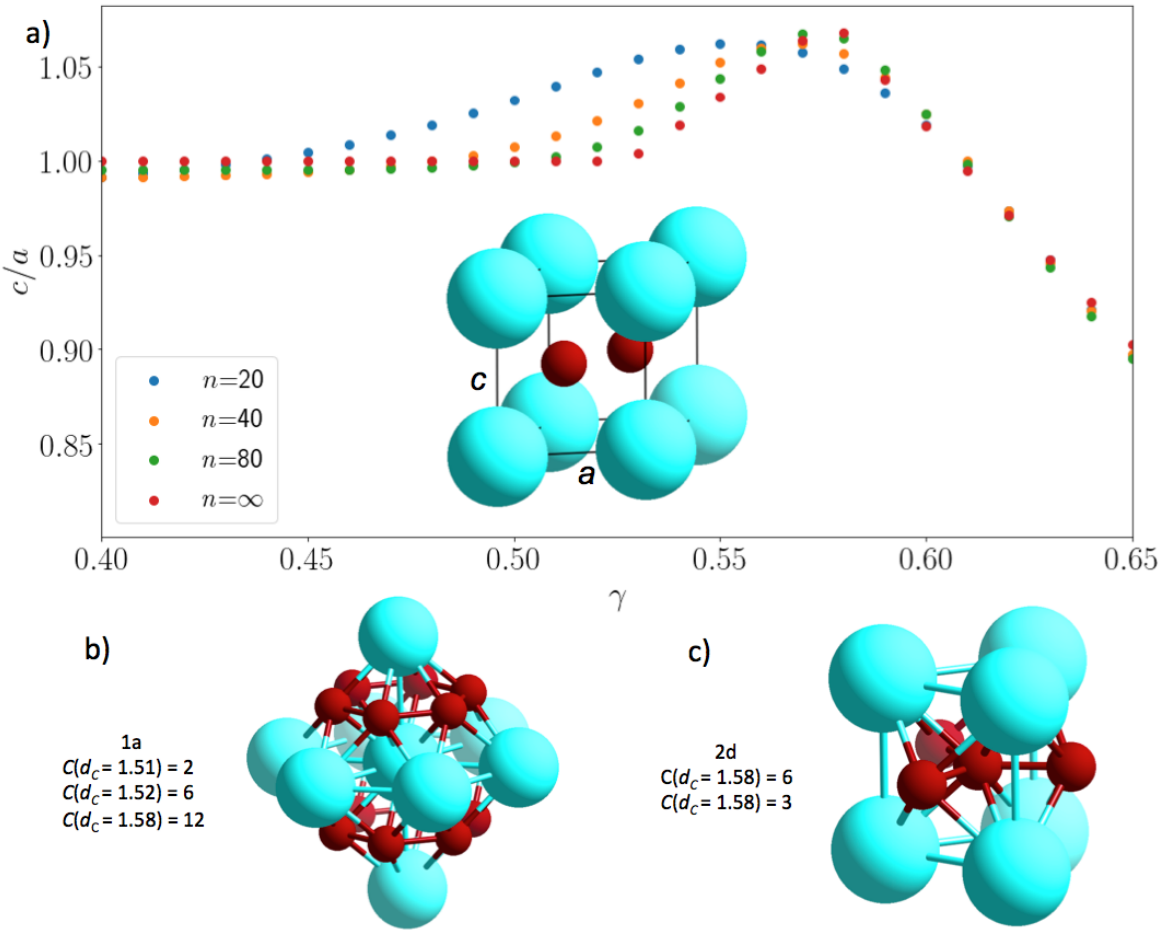

Figure 4.5: The a) optimal unit cell parameters (c and a) and local arrangements at the b) $1a$ (blue) and c) $2d$ Wyckoff sites (red) of the AlB_2 structure. The inset in a) shows the unit cell of AlB_2 for a $c/a = 1$. This particular AlB_2 structure was optimized for minimal enthalpy at $n = 45$ and $\gamma = 0.46$. C gives the number of particles at a particular contact distance, while d_c gives the distance to that particular set of neighbors divided by the average diameter of the particles, *i.e.*, the distance used in the IPL potential. Distances are all calculated with a number density of $1/\sigma^3$.

the distance between two particles divided by the average diameter of the particles, σ_{ij}) of the densest packing structure will be largest for the structure with the greater ϕ_m. The nearest contact will be the largest contribution to the energy of the structure; thus higher ϕ_m structures tend to have lower energy than competing phases. This leads to FCC being the stable unary phase for all n examined. The binary phase diagram is more diverse because there are many structures with both high ϕ_m and few contacts. Here we analyze how having a small number of contacts stabilizes two phases commonly observed in experiment[16, 18, 22, 56]: AlB_2 and $NaZn_{13}$. In Figure 4.5, we highlight the structure of AlB_2 optimized for $n = 45$ and $\gamma = 0.46$.

AlB_2 is the densest known packing for $0.53 < \gamma < 0.62$.[102] Its large particles are arranged in simple hexagonal layers whose interstitial voids are occupied by the small particles. The c/a ratio is the only degree of freedom of its unit cell; optimal c/a ratios for particular n and γ and interparticle distances are shown in Figure 4.5. These distances are scaled by σ_{ij}, the quantity relevant for the IPL potential and for ϕ_m calculations.

Lowering n from ∞ can expand the region of stability for AlB_2 down to $\gamma = 0.43$ despite it packing significantly less effectively than competing phases. For example, the AlB_2 structure reported in Figure 5 is more stable than AB_4 despite AB_4 having a higher ϕ_m (0.759 vs. 0.722). We can use their ϕ_m values to estimate energy differences, as the cube of the ratio of two structures' nearest contact distances is proportional to the ratio of their ϕ_m values if they have the same stoichiometry (see section 4.6.1). Therefore, this difference in ϕ_m indicates that the nearest contact of AB_4 (scaled to account for the stoichiometry difference) is $(0.759/0.722)^{1/3} = 1.018$ times farther away than in AlB_2, which, at $n = 45$, corresponds to AlB_2 having $1.018^{45} = 2.12$ times more energy per nearest contact. To define an "average" number of nearest neighbors, we note from Figure 4.5 that the nearest contact is at a scaled distance of ~ 1.51. The large particle has 8 such contacts while the tow small particles have none; thus we can define the average number of nearest contacts as $8/3 \sim 2.67$. The definition is reasonable as contacts from both large and small particles contribute equally to the total energy. The competing AB_4 structure has ~ 9.4 nearest contacts (data not shown); this difference enables the less densely packed AlB_2 structure to have a lower energy than AB_4 at $n = 45$. Non-nearest neighbors will also contribute to the total energy of both crystals, but have a substantially lesser influence than the nearest neighbor.

In $NaZn_{13}$ and several other structures, particles in a few Wyckoff sites have many nearest neighbors, but the average number per particle is low. The local environments of each Wyckoff site in $NaZn_{13}$ are shown in Figure 4.6. The standard unit cell of $NaZn_{13}$ contains 8 large particles and 104 small particles. Each large particle is surrounded by 24

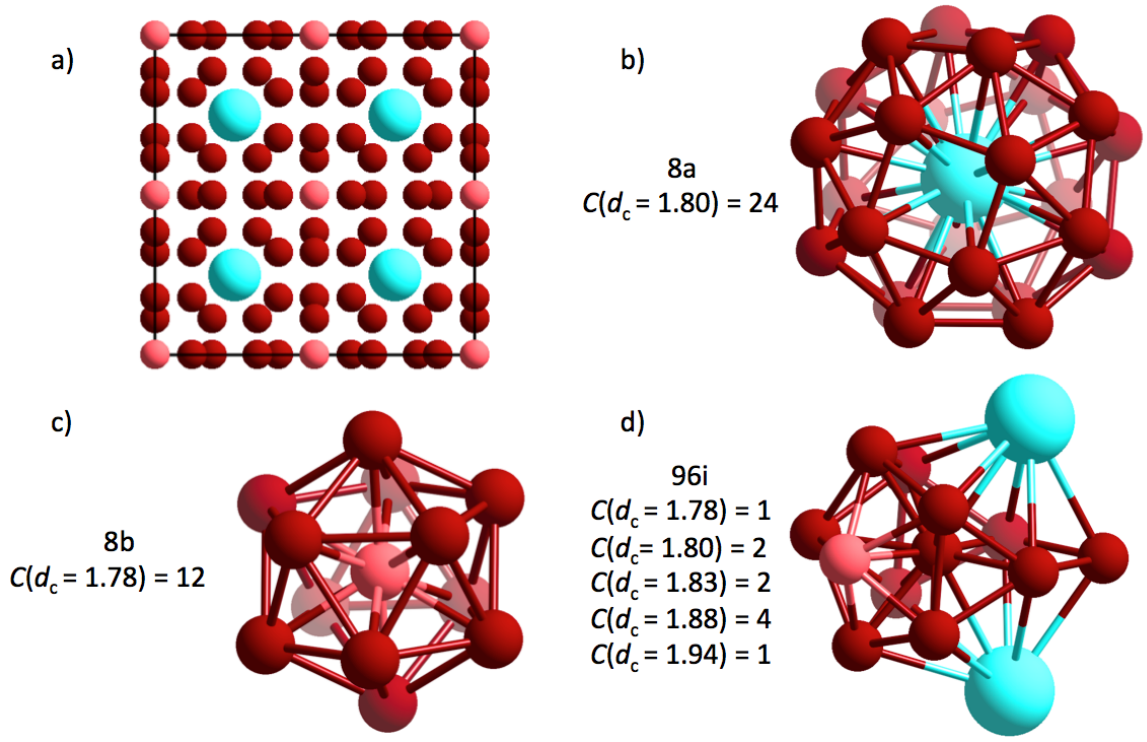

Figure 4.6: The a) $NaZn_{13}$ unit cell and the environments of its b) 8*a* (blue), c) 8*b* (light red), and d) 96*i* Wyckoff sites (dark red). This particular $NaZn_{13}$ structure was optimized for low enthalpy at $n = 60$ and $\gamma = 0.57$. C gives the number of particles at a particular contact distance, while d_c gives the distance to that particular set of neighbors divided by the average diameter of the particles (the distance used in the IPL potential). The distances are all calculated with a number density of $1/\sigma^3$.

small particles arranged at the vertices of a snub cube. Small particles in the 8*b* Wyckoff site occupy the center of an icosahedron of small particles, while those in the 96*i* position occupy the icosahedron's vertices. In general the snub cube and icosahedron are slightly distorted from the perfect shapes. Despite $NaZn_{13}$'s structural complexity, it is the most commonly observed binary structure in many colloidal self-assembly experiments, occurring across a wide range of particle compositions.[18, 56, 17]

Particles in the 8*a* (snub cube-coordinated) and 8*b* (icosahedrally coordinated) Wyckoff sites in $NaZn_{13}$ both have nearest neighbors slightly closer than competing structures (*e.g.*, AlB_2); furthermore, they both have a significant number of neighbors at the nearest contact distance. On the other hand, the 96*i* Wyckoff site, which accounts for 6/7 of the total number of particles, has relatively few nearest neighbors, so the average number of nearest neighbors per particle is low. Thus, if the particles are softer, diminishing slightly

the relevance of the first contact relative to further neighbors, $NaZn_{13}$ is stable for several values of γ.

It is interesting to consider $NaZn_{13}$'s stability in light of its coordination polyhedron. Both the icosahedron and snub cube are solutions to the Tammes problem, *i.e*, maximizing the smallest interparticle distance constrained on the surface of a sphere.[113, 114] While these distances do not correspond to the nearest contacts in $NaZn_{13}$, they influence the energy for finite n. Due to their distance-maximizing nature, the occurrence of these coordination polyhedra in structures in our phase diagram seems natural.

We suspect that this partially accounts for the icosahedral order observed in many binary nanoparticles superlattices,[115] several of which[35] adopt the structures in our phase diagram. Particularly notable is $MgZn_2$, which, being a Frank-Kasper phase, exhibits a significant amount of icosahedral local arrangements; we also find it to be stable over a substantial region of our phase diagram.

4.3.4 High n Limit

In Figure 4.2 we see that the hard sphere limit is not yet reached for $n = 100$, although the γ values where particular phases are stable do appear to be converging to the hard sphere case. This result is surprising to us, as other studies indicate that, for certain system properties (*e.g.*, melting points, transport coefficients) in unary systems, the hard sphere limit may be effectively reached for $n = 72$ or even $n = 18$.[116, 117] To better understand the hard sphere limit, we analyzed the degree to which having few nearest neighbors enhances the stability of a structure.

If n is sufficiently large, the energy of a structure can be approximated as

$$E/N = C\epsilon\left(\frac{\sigma_1}{r_1}\right)^n, \tag{4.3}$$

where C equals the average number of nearest contacts per particle and r_1/σ_1 is the nearest contact distance in the structure. Thus, as mentioned earlier, a structure with

low C may be stabilized over other structures with larger nearest contact distances (or, equivalently, larger ϕ_m). By equating the energy of two structures with different C, we can calculate the differences in nearest contact distance necessary for two structures with different C values to have the same energy:

$$\left(\frac{(r_1/\sigma_1)_b}{(r_1/\sigma_1)_a}\right)_{E_b=E_a} = \left(\frac{C_b}{C_a}\right)^{(1/n)}, \tag{4.4}$$

in which b and a are two different structures and the subscript $E_b = E_a$ indicates that the energy of the two structures are equal. We can also rewrite Equation 4.4 in terms of ϕ_m:

$$\left(\frac{\phi_{m,b}}{\phi_{m,a}}\right)_{E_b=E_a} = \left(\frac{C_b}{C_a}\right)^{(3/n)}. \tag{4.5}$$

From this we calculate the minimum ϕ_m that a low C structure can have and still be stable relative to a structure with high C and ϕ_m values. We show this in Figure 4.7 by comparing the energy for different C and n values to a structure with $C = 12$. The y-axis represents the smallest ϕ_m that a structure with a given C value can have relative to another structure with $C = 12$ and still be stable. In this calculation we are neglecting any neighbor shells beyond the first one and assuming structures of equal stoichiometry.

We see in Figure 4.7 that a low C value can stabilize many low ϕ_m structures, even when $n > 100$. This is essentially why, in Figure 4.2, differences exist between $n = 100$ and $n = \infty$. As established earlier, AlB_2 has 8/3 nearest contacts per particle for $\gamma \approx 0.46$; we indicate this point in Figure 4.7 for $n = 100$. We note that for many structures, including the AlB_2 and $NaZn_{13}$ structures shown, the second shell of neighboring particles is only slightly beyond the first, and thus the approximation in Equation 4.3 is large for smaller n, and the curves shown in Figure 4.7 should be interpreted qualitatively for real structures.

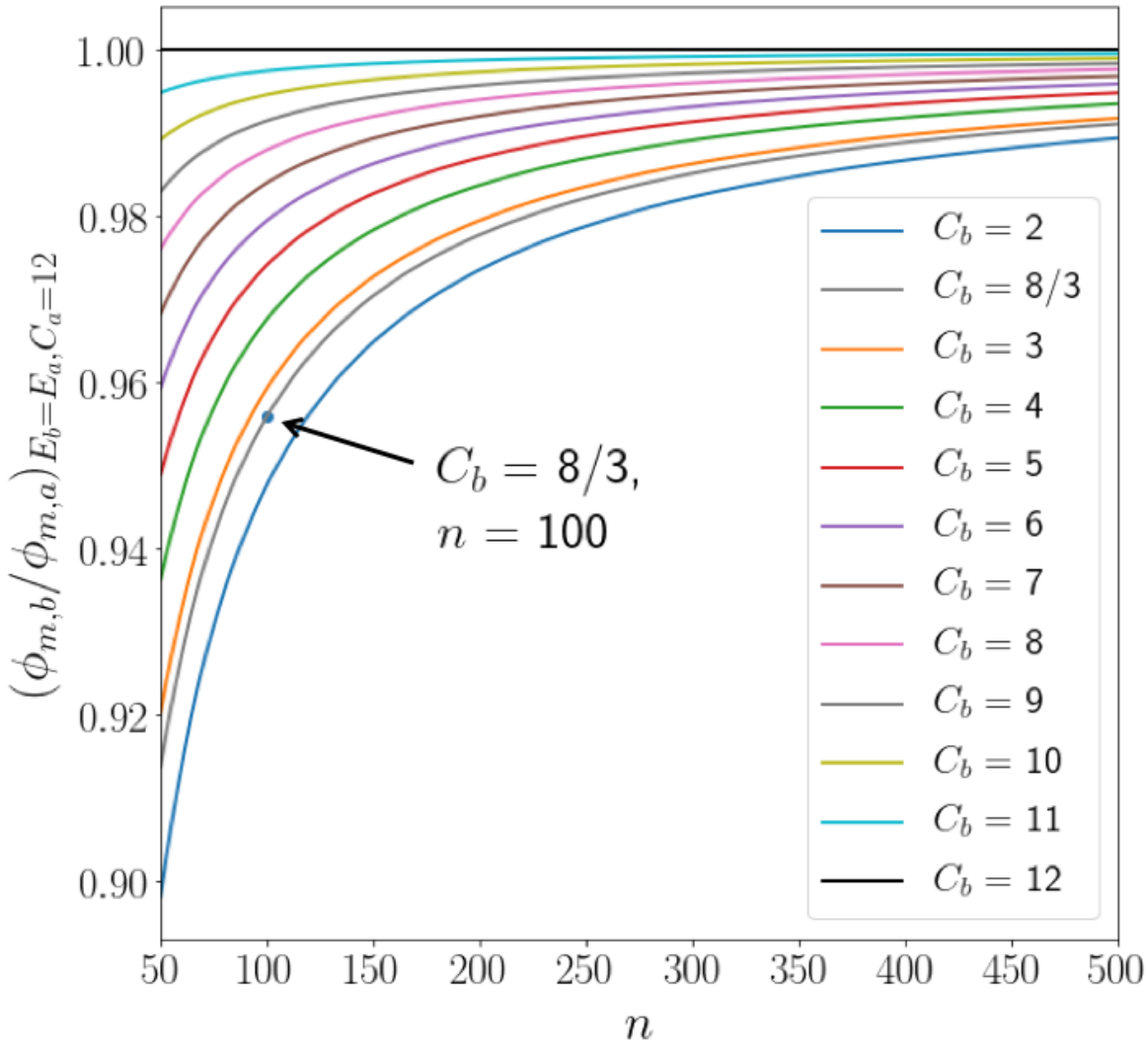

Figure 4.7: Plots of the lowest packing fraction ϕ_m that a structure b with a given number of nearest contacts C can have and still be stable relative to another structure a with higher C and ϕ_m values. In this plot we define structure a as having $C = 12$ in analogy with FCC. The subscript $E_b = E_a$ indicates that the energies of the two structures are equal, so the curves represent lower bounds on what $\phi_{m,b}$ can be for a stable structure. These curves were computed with Equation 4.5. In all cases we assume that any non-nearest neighbors contribute negligibly to the energy, which is a more accurate approximation at higher n.

4.3.5 Low n Limit

For $n = 6$, every binary phase becomes unstable with respect to two phase-separated FCC structures containing only large and only small particles, respectively. While the same observation has been made previously for a smaller group of candidate structures,[86, 118] we were surprised to see this occur for our much larger group of candidate structures. Excluding the Laves phases, which are destabilized for all γ only below $n = 7$, every binary structure is destabilized for $n \leq 13$. This destabilization necessarily results from the energetic cost of neighbor shells beyond the first. Thus, it seems as though FCC has a particularly favorable set of neighbor shells for very soft particles.

As mentioned previously, other work has shown that reducing the additivity between unlike particles results in the observation of more binary phases.[86] We keep our potential additive for consistency with our results at higher n, but, as others have noted,[118, 119] it is likely that the assumption of additivity for very soft, repulsive particles is not applicable to many binary self-assembly experiments. For our final optimization run at $n = 6$, we truncate our potential at the fairly long distance of 12σ, which makes it very unlikely that the truncation significantly influenced our results. We also note the previous reports of fluid-fluid phase separation for the IPL model at $\gamma = 1/3$ and $n = 6$.[120]. In this paper, our primary focus is on higher values of n.

4.3.6 Experimental Relevance

Here we discuss a few experimental systems where we believe softly repulsive forces likely play a role in self-assembly: colloids thought to behave like hard spheres ("nearly-hard spheres"), certain metal and semiconductor nanoparticles, and like-charged colloids. We explicitly neglect discussing certain cases where we expect our model to fail, such as colloids functionalized with complementary DNA or oppositely charged colloids, who probably have a significantly different driving force for assembly.[121, 122] We also discuss why certain phases we predict to be stable have not been observed experimentally, and

possible implications for the behavior of atomic systems at high pressure.

Our results indicate that softness plays a role in binary colloidal crystals with "nearly-hard" colloidal spheres, as their effective n is often less than or around 100.[85] The phases observed thus far in experiment are NaCl, AlB_2, $NaZn_{13}$, and the Laves phases (with various degrees of stacking disorder).[18, 123, 26] We find that intermediate hardness ($\sim 20 < n < 100$) increases the range of γ over which each of these structures is stable relative to $n = \infty$. Furthermore, we find that some densely packed phases that have not been reported in experiment are destabilized by softness, including d-NaCl, AB_3, and d-AlB_2. We suspect that particle softness may be partially responsible for their failure to assemble in experiment.

Interestingly, all of the experimentally observed phases reported in the literature are also known to be stabilized by entropy in binary hard sphere systems; thus entropy and softness likely both play a role in their formation. While we do not quantify their relative contributions in this study, we can say that increasing the softness of the particles (at least to $n \sim 30$) should increase their likelihood to self-assemble. In fact, a recent report found that repulsive softness did promote the self-assembly of Laves phases, in direct agreement with our predictions[110]. Decreasing the role of entropy in such systems by reducing the temperature or increasing the density should further increase their correspondence with our phase diagram; it would be interesting to see then if the stable phases we find that have not been observed in experiment (*e.g.*, AB, AB_3) could be experimentally realized.

Our results are particularly interesting with regards to the self-assembly of the Laves phases with polymer microgels reported by Schaertal *et al.*[26] The Laves phases are known to be stabilized by entropy at finite temperatures in hard sphere systems—a fact that was used to justify their appearance in these systems. However, Schaertal *et al.*, estimated the n and γ values of their particles to be ~ 45 and ~ 0.77, respectively—only slightly outside of the region in which we predict the Laves phases to be stable due solely to the softness of the interparticle interactions. Thus, we strongly suspect that enthalpic

effects played a role in the observation of the Laves phases in that study.[26]

Experiments with metal and semiconductor nanoparticles have yielded several new phases in addition to those observed for nearly-hard spheres.[22, 56, 75] We also see two of these additional phases in our phase diagram: AB_4[104] and CaB_6.[106] The appearance of these phases in addition to those observed for nearly-hard spheres implies that repulsive forces also play a key role in their assembly. Nonetheless, our results will not account for several of the binary colloidal crystals observed in experiment. These include structures with lower ϕ_m (*e.g.*, AuCu, Li_3Bi, Fe_4C; with our model, structures generally must have a fairly high ϕ_m value to be stable). For many of these nanoparticles, the size of the ligand corona is comparable to that of the nanoparticle core, and accounting for the stability of these structures has thus far only been accomplished by the orbifold topological model for ligand behavior.[124, 125] In predicting some experimentally observed phases but not others, our model may be useful in determining when interactions more complicated than pairwise repulsion are influencing phase behavior.

Fewer reports of the self-assembly of binary structures with like-charged particles exist, but most of the reported structures are similar to those reported for other repulsive particles. The most notable results are those of Hachisu *et al.*,[16, 17] who investigated binary suspensions of charged latex particles over 30 years ago. They found every structure observed for nearly-hard spheres, as well as two additional ones: $CaCu_5$, which is commonly observed in nanoparticle assembly, and a structure with stoichiometry L_1S_4. Further reports of the structures observed in nearly-hard sphere systems have appeared since then[81, 126]; our finding that these phases are also stabilized by interaction softness explains their occurrence. Below we discuss the possible reasons why $CaCu_5$ does not appear in our phase diagram, but the few reports of the L_1S_4 structure make its experimental observation harder to understand. Recently, more self-assembly experiments with polydisperse charged particles have been reported,[126] so hopefully future results will clarify certain discrepancies between experiment and our phase diagram.

We also find a few phases to be enthalpically stable for soft particles that have not been reported in experiment. Most notable are AB and AB_3; we find them to be stable for γ values commonly examined in experiment. Our finite temperature results clearly explain the instability of AB_3. We could not rule out the stability of the AB phase on the entropy, but instead suspect its nonappearance is due to kinetic effects. $CaCu_5$ and $NaZn_{13}$ commonly self-assemble in experiment for similar γ values, and prior research has indicated that both of these phases may have particularly low nucleation barriers, which could cause them to form instead of the equilibrium phases.[17, 96]

Finally, we note that softness may be an important factor in preventing certain densely packed phases from being observed in atomic systems. Many recently discovered densely packed phases[103, 102] appear to not correspond to any known atomic structure. They include phases represented in our phase diagram as d-AlB_2, d-NaCl, AB_3 and a few others produced by the candidate structures listed in Table 4.2. Our results indicate that a very small amount of interaction softness suffices to destabilize many of these new densely packed structures in favor of more commonly observed structures (*e.g.,* the Laves phases, AlB_2), even at the high pressures where densely packed phases are more likely to appear.

4.4 Conclusions

We investigated the influence of interparticle interaction softness on the solid phase behavior of binary sphere systems by determining the ground state enthalpies of a wide variety of structures modeled by an additive inverse power law potential. We found that a surprisingly small amount of softness can influence the phase diagram, and that considerable softness will destabilize every examined binary phase relative to coexisting single-component FCC phases at zero temperature. We compared our results to a long list of experimental findings. We suspect that the softness of colloidal particles is responsible for the lack of observation of certain densest packings in experiment, and posit that particle softness likely influences the frequent observation of structures with icosahedral

local order.

In this study we neglected all kinetic influences on the phase behavior, and only investigated entropic effects for a few cases. In doing so, we vastly enlarged the space of structures we were able to examine, as both free energy calculations and crystallization simulations from disordered initial conditions can be computationally expensive. Despite this focus on ground state crystal phases, our work helps explain why certain structures not described by dense packings are observed in experiments on binary colloidal crystals. We expect our findings to be particularly useful for those working with particles of variable softness, such as charged particles, polymer beads, or small nanoparticles functionalized with sterically interacting ligands, and to guide the design of particle interactions to self-assemble target structures, particularly in low temperature or high pressure systems where entropy does not play a significant role.

4.5 Methods

We calculated the ground state phase diagram by computing the enthalpy H of different structures at temperature $T = 0$ and reduced pressure $P\sigma^3/\epsilon = 1$. The well-known scaling properties of the IPL potential model[91, 97] allow the calculation of H at any P for a configuration of N particles through a calculation of potential energy E at the corresponding density $\phi = N/V$, where V is the volume of the simulation box (see section 4.6.1).

We found low enthalpy structures using a basin hopping global minimization technique on the free parameters of the Wyckoff sites of particular space groups. For example, we optimized over structures with space group symmetry $C2/m$ (no. 12) with the large particles in Wyckoff site $2a$ and the small particles in Wyckoff site $4i$. Wyckoff site $4i$ has two free parameters and the monoclinic unit cell of space group $C2/m$ has an additional 3 parameters that can be optimized (β, where a, b, and c correspond to the lattice vectors of the unit cell and β is the angle between a and c), for a total of 5 degrees

of freedom. In structures where we optimized the lattice vectors, we limited b/a and c/a to between 0.25 and 4 if no dense known packings exist outside those bounds. In certain cases where we know dense packings exist outside those bounds, we expanded the upper bound from 4 to 6. For monoclinic structures we kept θ between 60° and 120°, as every known dense packing is within those bounds. Limiting these parameters reduced errors resulting from finite size effects. Candidate space groups and Wyckoff sites (see Table 4.2) were selected from those thought to produce structures with high ϕ_m[103, 127] or experimentally observed structures. Structures are labeled by their atomic equivalent if known; other structures we found to be stable are labeled by their stoichiometry. In general the stoichiometry of a phase is determined from the number of particles in large (L) or small (S) Wyckoff sites. We did not include some known dense packing phases because they have exceedingly low symmetry[101, 102] and thus would require extensive time to optimize; however in such cases we included slightly symmetrized versions of the structures with only marginally reduced ϕ_m (typically $\sim$ 0.2% less). Our overall approach in optimizing the degrees of freedom of Wyckoff sites is similar to approaches in the literature.[105, 103, 127]

Optimizing over particular space groups and Wyckoff sites enabled us to search a wide array of possible structures while allowing for simple identification of the resulting low energy structure. First, several of the higher symmetry structures had no free parameters (*e.g.,* NaCl) or had well-known free parameters (AlB_2, CaB_6, $MgZn_2$, $NaZn_{13}$), which made their identification trivial. The values of the free parameters would typically vary slightly for different n and γ, similarly to how they vary for atomic crystals. Second, if the lower symmetry space groups produced structures with the same energy as those of known identity that we also examined, we would conclude, after visual inspection, that they were identical. This situation was extremely common, as several low symmetry space groups reduced to NaCl or AlB_2. Third, if the structure did not correspond to a known higher symmetry structure, we compared their packing fractions and appearance

Table 4.2: Candidate Structure Types

Structure type	Space group		Wyckoff sites	
			L	S
$cF8$–NaCl	$Fm\bar{3}m$	225	$4a$	$4b$
$hP4$–NiAs	$P6_3/mmc$	194	$2a$	$2c$
$cP2$–CsCl	$Pm\bar{3}m$	221	$1a$	$1b$
$tP2$–CuAu	$P4/mmm$	123	$1a$	$1d$
$oP8$–AB	$Pnma$	62	$4c$	$4c$
$oC8$	$Cmmm$	65	$4g$	$4j$
$hP3$–AlB_2	$P6/mmm$	191	$1a$	$2d$
$hP12$–$MgZn_2$	$P6_3/mmc$	194	$4f$	$2a$, $6h$
$hP24$–$MgNi_2$	$P6_3/mmc$	194	$4e$, $4f$	$4f$, $6g$, $6h$
$cF24$–$MgCu_2$	$Fd\bar{3}m$	227	$8b$	$16c$
$oP12$	$P2_12_12_1$	19	$4a$	$4a$, $4a$
$mC6$	$C2/m$	12	$2a$	$4i$
$oC12$–AB_2	$Cmc2_1$	36	$4a$	$4a$, $4a$
$hP6$	$P6_3/mmc$	194	$2b$	$4f$
$oP12$	$Pnma$	62	$4c$	$4c$, $4c$
$mC12$	Cm	8	$2a$, $2a$	$2a$, $2a$, $2a$, $2a$
$oC20$–A_3B_7	$I222$	23	$2a$, $4j$	$2c$, $4j$, $8k$
$mC14$	Cm	8	$2a$, $2a$	$2a$, $2a$, $2a$, $4b$
$cP4$–Cu_3Au	$Pm\bar{3}m$	221	$1a$	$3c$
$cF16$–Li_3Bi	$Fm\bar{3}m$	225	$4a$	$4b$, $8c$
$cP8$–Cr_3Si	$Pm\bar{3}n$	223	$2a$	$6c$
$oC16$	$Cmcm$	63	$4c$	$4c$, $8g$
$oP8$–AB_3	$Pmmn$	59	$2a$	$2b$, $4f$
$oF20$	$F222$	22	$4a$	$16k$
$cP5$–Fe_4C	$P\bar{4}3m$	215	$1a$	$4e$
$tP20$–AB_4	$P4bm$	100	$4c$	$4c$, $2a$, $2a$, $8d$
$hP30$	$P6_3mc$	186	$6c$	$6c$, $6c$, $6c$, $2a$, $2b$, $2b$
$hP6$–$CaCu_5$	$P6/mmm$	191	$1a$	$2c$, $3g$
$cP7$–CaB_6	$Pm\bar{3}m$	221	$1a$	$6f$
$cI14$–bcc-AB_6	$Im\bar{3}m$	229	$2a$	$12d$
$oI14$–AB_6	$Immm$	71	$2a$	$4f$, $4h$, $4j$
$cF112$–$NaZn_{13}$	$Fm\bar{3}c$	226	$8a$	$8b$, $96i$
$cP14$	$Pm\bar{3}m$	221	$1a$	$1b$, $12i$

to structures reported to be dense packings in other papers, allowing us to identify AB, AB_2, AB_3, and AB_6. As with the more well-known structures the free parameters of these structures would typically vary slightly with different γ and n. Finally, AB_4 was identified by comparison with a well-described experimental structure[104]. Note that the last two tasks greatly simplified by the fact that most of our candidate space groups were motivated by reports of dense packings and experimental structures.

Using the Python library Scipy's[128] functions for basin hopping[129] and sequential least squares programming minimization, we conducted global minimization on almost every structure for IPL exponent n between 6 and 100 and γ between 0.3 and 0.9. The

exceptions are two structures with a large number of degrees of freedom (specifically the two with space group symmetry Cm (no. 8)); they were only optimized for γ in the vicinity of where they are known to produce dense packings ($0.43 \leq \gamma \leq 0.52$).[102] We performed at least two unbiased runs of 200 basin hopping steps for each structure with more than two degrees of freedom. After conducting the unbiased global optimization runs, we determined which structures are most stable for particular values of n and γ, and for those structures we conducted another nine local minimization runs for each n and γ, starting from the values of the free parameters found previously for the state point, as well as those for the eight immediately neighboring n and γ values. The second run had a lower tolerance for convergence and served to refine the boundaries of phase stability. The presence of distinct regions of structural stability in our phase diagram gives us confidence that we accurately detected each enthalpy minimum.

The lowest enthalpy phases in the $n = \infty$ limit correspond to the densest packing phases at a given γ and stoichiometry. With the exception of AB_4 (a dense packing discovered in this project), the putative densest packing phases were taken from the literature. For AB_4 and the approximations of the densely packed phases, we conducted short basin hopping runs to optimize their ϕ_m for particular γ values.

The enthalpy of the candidate structures during optimization was evaluated by constructing a perfect crystal containing many unit cells and evaluating the enthalpy of a single, central unit cell. These perfect structures were all constructed at a number density of $1/\sigma^3$. The number of particles was varied from ~ 500 to $\sim 100,000$, depending on the n used. For the unbiased basin hopping runs, we truncated our potential at distances varying from 4σ to 10σ; for the final nine local optimization runs we truncated it at distances varying from 6σ to 12σ. Long-range corrections were applied to account for the finite cutoffs of the potential. The signac data management framework supported our computational workflow and data management.[73]

The free energies of particular phases at finite temperature were calculated using the

Einstein molecule method with the HOOMD-blue simulation toolkit. [65, 66] The Einstein molecule method is a variant of the Frenkel-Ladd method in which the position of a single particle within the simulation box is constrained instead of the center of mass.[71] The methods involve using thermodynamic integration to compute the free energy differences between a crystal of harmonic oscillators to the real crystal under scrutiny; the accuracy of the method is limited only by numerical precision. Further details of the method have been reported in several places.[70, 71, 130] We set the de Broglie wavelength of each particle equal to unity; doing so does not affect phase equilibrium. The integration was performed in 20 steps using an Einstein molecule with a harmonic constant of $2 \cdot 10^5$. To reduce the errors from using a large harmonic constant, we used a time step of $10^{-4}\ \sigma(m/kT)^{1/2}$.

Einstein molecule calculations were performed at constant density and $kT/\epsilon = 1$ on crystals of at least 1000 particles. The density was chosen to be close to the melting point, and the temperature was maintained with the Langevin thermostat. Pressure-volume data was obtained from conducting NPT simulations with the Nosé-Hoover thermostat and barostat; this data was thermodynamically integrated to find G at a particular pressure. The pressure presented in Table 4.1 was chosen to be slightly lower than the melting point of FCC_S (as determined by interpolating the data of Agrawal *et al.*[112]) but high enough for the crystal to be metastable. Standard deviations were computed by running 3 independent replicas of every simulation.

4.6 Supplement

4.6.1 Ground State Enthalpy

Here we derive the equation used to calculate the enthalpy of our structures at constant pressure. For completeness we begin our derivation from basic thermodynamic principles and the inverse power law (IPL) model. Some of what we present is already known or easily extendable from the literature.[97]

Definitions

E = Total Energy

H = Enthalpy

A = Helmholtz Free Energy

G = Gibbs Free Energy

K = Kinetic Energy

U = Potential Energy

T = Temperature

S = Entropy

P = Pressure

V = Volume

N = Number of Particles

ρ = Number Density (N / V)

Thermodynamic Potentials

At constant P and T, the expected macrostate of a system is the one with minimal G:

$$G = E - TS + PV. \tag{4.6}$$

At T = 0, G is given by:

$$G(T = 0) = E + PV, \tag{4.7}$$

or, alternatively,

$$G(T = 0) = H. \tag{4.8}$$

Therefore, we can say that at zero temperature and constant pressure that the enthalpy must be minimized in equilibrium.

For $T = 0$, the system has no kinetic energy, and thus

$$E(T = 0) = U, \tag{4.9}$$

and

$$P(T = 0) = -\left(\frac{\partial U}{\partial V}\right)_{N,V,T}. \tag{4.10}$$

Pressure of Inverse Power Law Potential

With the IPL potential, the energy of interaction between two particles i and j is given by

$$U_{ij} = \epsilon\Big(\frac{\sigma_{ij}}{r_{ij}}\Big)^n. \tag{4.11}$$

The value of σ_{ij} is σ, $(\sigma + \sigma\gamma)/2$, or $\sigma\gamma$ depending on whether the interacting pair consists of two large particles, a large and a small particle, or two small particles, respectively. The total potential energy of the system is then

$$U = \sum_i \sum_j \frac{\epsilon}{2}\Big(\frac{\sigma_{ij}}{r_{ij}}\Big)^n. \tag{4.12}$$

We can write the density of the system in reduced units $\rho\sigma^3$. For $T = 0$ all interparticle distances r_{ij} in the system scale with the density or volume:

$$\frac{r_{ij}(\rho\sigma^3 = \rho_2\sigma_2^3)}{r_{ij}(\rho\sigma^3 = \rho_1\sigma_1^3)} = \Big(\frac{\rho_1\sigma_1^3}{\rho_2\sigma_2^3}\Big)^{1/3}. \tag{4.13}$$

Thus we can write:

$$r_{ij}(\rho\sigma^3) = \frac{r_{ij}(\rho\sigma^3 = 1)}{\rho^{1/3}\sigma}. \tag{4.14}$$

Substituting this into Equation 4.12:

$$U = \sum_i \sum_j \frac{\epsilon}{2}\Big(\frac{\sigma_{ij} \cdot \rho^{1/3}\sigma}{r_{ij}(\rho\sigma^3 = 1)}\Big)^n \tag{4.15}$$

$$= U(\rho\sigma^3 = 1) \cdot (\rho\sigma^3)^{n/3}. \tag{4.16}$$

Thus, if we calculate U at one density we can easily compute it at any other density. In addition, we can compute P from Equation 4.10:

$$-\left(\frac{\partial U}{\partial V}\right)_{N,V,T} = -\frac{\partial\big(U(\rho\sigma^3 = 1) \cdot (\rho\sigma^3)^{n/3}\big)}{\partial V}. \tag{4.17}$$

The internal energy at a density of $1/\sigma^3$ is a constant. The density term can be rewritten in terms of the volume:

$$P = U(\rho\sigma^3 = 1)\frac{-\partial\big((N\sigma^3/V)^{n/3}\big)}{\partial V} \tag{4.18}$$

$$= U(\rho\sigma^3 = 1)\frac{n(N\sigma^3)^{n/3}}{3V^{n/3+1}} \tag{4.19}$$

$$= U(\rho\sigma^3 = 1)\frac{n(\rho\sigma^3)^{n/3}}{3V} \tag{4.20}$$

$$= \frac{nU}{3V}. \tag{4.21}$$

The finite temperature version of this result was given by Hoover et al. in 1970.[91]

Enthalpy at Zero Temperature

Our goal is to calculate H at constant P. With our results from Section S1.3, we can find an exact result for H at $T = 0$:

$$H = E + PV \tag{4.22}$$

$$= \frac{3PV}{n} + PV \tag{4.23}$$

$$= PV\left(\frac{3}{n} + 1\right). \tag{4.24}$$

We can find $V(P)$ by rearranging Equation 4.19:

$$V = \left(\frac{n(N\sigma^3)^{n/3}U(\rho\sigma^3 = 1)}{3P}\right)^{\frac{1}{n/3+1}} \tag{4.25}$$

$$= N\sigma^3\left(\frac{nU(\rho\sigma^3 = 1)}{3PN\sigma^3}\right)^{\frac{1}{n/3+1}}. \tag{4.26}$$

Substituting this into Equation 4.24 we obtain:

$$\frac{H}{N} = P\sigma^3\left(\frac{3}{n} + 1\right)\left(\frac{n(U(\rho\sigma^3 = 1)/N)}{3P\sigma^3}\right)^{\frac{1}{n/3+1}}. \tag{4.27}$$

Varying P in Equation 4.27 will not affect the relative stability of different phases; only varying $U(\rho\sigma^3 = 1)$ or n will.

Enthalpy at Zero Temperature and Infinite n

As n approaches ∞, Equation 4.12 becomes

$$\frac{U}{N} = \epsilon\left(\frac{\sigma_1}{r_1}\right)^n, \tag{4.28}$$

where σ_1/r_1 is the largest value in Equation 4.12. Its inverse r_1/σ_1 is the nearest contact distance in a structure. Substituting this equation into Equation 4.27 and taking the limit as n approaches ∞:

$$\frac{H}{N} = P\sigma^3\left(\frac{\sigma_1}{r_1}\right)^3_{\rho\sigma^3=1}. \tag{4.29}$$

We know that at any density ρ in which the particles do not overlap, ϕ_m will be the volume occupied by spheres multiplied by ρ:

$$\phi_m = \rho(x_L + x_S\gamma^3)\frac{4\pi(\sigma/2)^3}{3}. \tag{4.30}$$

To calculate a structure's maximum packing fraction we need to determine how much the structure can be compressed without the particles overlapping. We can compute this from the nearest contact distance and the scaling relation between interparticle distances and the density (Equation 4.14):

$$\rho_{max} = \rho_{ref}\left(\frac{r_1}{\sigma_1}\right)^3_{ref}. \tag{4.31}$$

Thus if we know the nearest contact distance at any given reference density we can calculate the maximum density and, through Equation 4.30, its maximum ϕ_m. We prepared structures at a density of $1/\sigma^3$ and calculated their packing fraction with

$$\phi_m = \frac{4\pi(x_L + x_S\gamma^3)(\sigma/2)^3}{3\sigma^3} \cdot \left(\frac{r_1}{\sigma_1}\right)^3_{\rho\sigma^3=1}. \tag{4.32}$$

We can now compute H of hard spheres directly from ϕ_m. Through combining Equations 4.29 and 4.32:

$$\frac{H}{N} = \frac{4\pi P(x_L + x_S\gamma^3)(\sigma/2)^3}{3\phi_m}. \tag{4.33}$$

Equation 4.33 shows that the enthalpy of a structure is inversely proportional to its packing fraction, and thus, for a system of particular x_L and x_s (which, of course, depend on each other) and σ and γ, the phase with the highest packing fraction will minimize the enthalpy.

4.6.2 Scaling Properties and Behavior in Different Limits of the IPL Model

Here we discuss certain aspects of the IPL model that we make use of in the main text. Much of the discussion focuses on the $n \to \infty$ limit (i.e. the hard sphere model). We also verify our theoretical expression for the $T = 0$ enthalpy of IPL systems (Equation 4.27) by comparison with simulation.

Thermodynamic Scaling of Inverse Power law and Hard Sphere Models

We review the previously known[91] scaling properties of the inverse power law (IPL) and hard sphere model for completeness. At constant volume, these scalings follow from the classical configuration integral:

$$Z(NVT) = \int \exp\left[-\frac{U(\mathbf{x})}{kT}\right] d\mathbf{x}, \tag{4.34}$$

in which $\mathbf{x}$ is a vector containing the coordinates of all N particles.

For hard spheres at finite temperature, for which U/kT can be 0 or ∞, the configuration integral reduces to:

$$Z(NVT) = \Omega(NV), \tag{4.35}$$

in which Ω is the volume of configuration space in which the particles do not overlap. This quantity does not depend on the temperature, and thus neither does the thermodynamic behavior of hard spheres in the NVT ensemble.

For soft spheres, whose potential energy can be written in the form of Equation 4.16, the configuration integral instead becomes:

$$Z(NVT) = \int \exp\left[- \frac{(\rho\sigma^3)^{n/3}}{kT} U(\rho\sigma^3 = 1, \mathbf{x}) \right] d\mathbf{x}, \tag{4.36}$$

in which $U(\rho\sigma^3 = 1, \mathbf{x})$ is the potential energy of a particular configuration ($\mathbf{x}$) of particles scaled to a density of $1/\sigma^3$.

Changing the density or temperature will not change the value of $U(\rho\sigma^3 = 1, \mathbf{x})$, so the configuration integral will only change with quantity $\frac{(\rho\sigma^3)^{n/3}}{kT}$, a thermodynamic scaling parameter incorporating both temperature and density. Note that the parameter can be made unitless by extracting ϵ from $U(\rho\sigma^3 = 1, \mathbf{x})$.

One expression for the classical partition function of the NPT ensemble is::

$$\Delta(NPT) = \frac{1}{\Lambda^{3N} N!} \int \exp\left[- \frac{U(\mathbf{x}) + PV(\mathbf{x})}{kT} \right] d\mathbf{x}. \tag{4.37}$$

Denoting an indicator function for all nonoverlapping configurations as $\mathbf{1}_{U=0}(\mathbf{x})$, which is unity if the particles do not overlap but zero otherwise, we can rewrite the partition function as:

$$\Delta(NPT) = \frac{1}{\Lambda^{3N} N!} \int \mathbf{1}_{U=0}(\mathbf{x}) \exp\left[- \frac{PV(\mathbf{x})}{kT} \right] d\mathbf{x}, \tag{4.38}$$

which reveals the scaling parameter of hard sphere systems at constant pressure to be P/kT, and that approaching the high P limit is equivalent to approaching the low T limit. Note that the expression can become unitless by extracting σ^3 from $V(\mathbf{x})$.

For soft spheres, we will not derive the scaling parameter, but instead present the one used recently by Travesset[97] : $\left(\frac{P\sigma^3}{\epsilon}\right)\left(\frac{\epsilon}{kT}\right)^{(3/n+1)}$. One can clearly see that as n proceeds to ∞, the expression reduces to the hard sphere case.

As evidence for the expression's accuracy, we present some NPT data in Table 4.3 which we generated using the HOOMD-blue simulation toolkit[65, 66]. We computed the density from NPT simulations to show that, at different values of $\frac{P\sigma^3}{\epsilon}$ and $\frac{kT}{\epsilon}$ which

Table 4.3: Thermodynamic Scaling Examples

n	$\left(\frac{P\sigma^3}{\epsilon}\right)\left(\frac{\epsilon}{kT}\right)^{(3/n+1)}$	$\frac{P\sigma^3}{\epsilon}$	$\frac{kT}{\epsilon}$	$\rho\sigma^3$	$\frac{(\rho\sigma^3)^{n/3}}{kT}$
25	13.84	13.84	1.0	1.033(1)	1.310(12)
25	13.84	1.0	0.09556	0.779(2)	1.309(22)
10	30.64	30.44	1.0	1.338(1)	2.640(6)
10	30.64	1.0	0.07190	0.607(1)	2.640(9)

produce the same value of the PT scaling variable, we obtain the same values of the VT scaling parameter, indicating thermodynamic equivalence. Properties were computed for systems of 2048 particles in the FCC lattice. The specific state points were chose to match some of those from Agrawal et al., [112] and we confirmed that our computed densities agree with their results.

Dense Packings as the Ground States of Hard Particle Systems

In section 4.6.1 we show that dense packings are the ground states of hard sphere systems at constant pressure by taking the $n \to \infty$ limit of the equation for the enthalpy of the IPL model at $T = 0$. Here we present an alternative derivation by taking the $T \to 0$ limit of the Gibbs free energy in terms of the NPT partition function:

$$\lim_{kT\to 0} G = \lim_{kT\to 0} -kT \ln\left(\frac{1}{\Lambda^{3N} N!}\int \exp\left[-\frac{U(\mathbf{x}) + PV(\mathbf{x})}{kT}\right] d\mathbf{x}\right). \tag{4.39}$$

For $kT \to 0$, the term $kT \ln\left(\frac{1}{\Lambda^{3N} N!}\right) \to 0$, and for any hard shape at finite temperature U/kT can only be 0 or ∞. Denoting an indicator function for all nonoverlapping configurations as $\mathbf{1}_{U=0}(\mathbf{x})$, we can rewrite the partition function as:

$$\lim_{kT\to 0} G = \lim_{kT\to 0} \frac{-1}{1/kT} \ln \int \mathbf{1}_{U=0}(\mathbf{x}) \exp\left[-\frac{PV(\mathbf{x})}{kT}\right] d\mathbf{x}, \tag{4.40}$$

which is an indeterminate form. For finite P we can apply L'Hopital's rule to obtain

$$\lim_{kT\to 0} G = \lim_{kT\to 0} (kT)^2 \frac{\int \mathbf{1}_{U=0}(\mathbf{x}) \frac{PV(\mathbf{x})}{(kT)^2} \exp\left[-\frac{PV(\mathbf{x})}{kT} \right] d\mathbf{x}}{\int \mathbf{1}_{U=0}(\mathbf{x}) \exp\left[-\frac{PV(\mathbf{x})}{kT} \right] d\mathbf{x}}, \tag{4.41}$$

$$= \lim_{kT\to 0} \frac{\int \mathbf{1}_{U=0}(\mathbf{x}) PV(\mathbf{x}) \exp\left[-\frac{PV(\mathbf{x})}{kT} \right] d\mathbf{x}}{\int \mathbf{1}_{U=0}(\mathbf{x}) \exp\left[-\frac{PV(\mathbf{x})}{kT} \right] d\mathbf{x}}. \tag{4.42}$$

We can rewrite this integral in terms of V, writing the degeneracy of each V as $\Omega(V)$. Furthermore we can multiply both the numerator and denominator by $\exp[PV_{min}/kT]$, where V_{min} is the smallest possible volume the system can take in which the spheres do not overlap:

$$\lim_{kT\to 0} G = \lim_{kT\to 0} \frac{\int \Omega(V) PV \exp\left[-\frac{P(V-Vmin)}{kT} \right] dV}{\int \Omega(V) \exp\left[-\frac{P(V-V_{min})}{kT} \right] dV}, \tag{4.43}$$

We are also free to multiply both the numerator and denominator by P/kT. As $kT \to 0$, the exponential function multiplied by this term proceeds to a delta distribution centered at V_{min}. After integration we arrive at:

$$\lim_{kT\to 0} G = \frac{\Omega(V_{min}) PV_{min}}{\Omega(V_{min})}, \tag{4.44}$$

$$= PV_{min}. \tag{4.45}$$

As the phase with V_{min} is also the densest packing, we find that the densest packing phase represents the ground state of hard sphere systems at constant pressure.

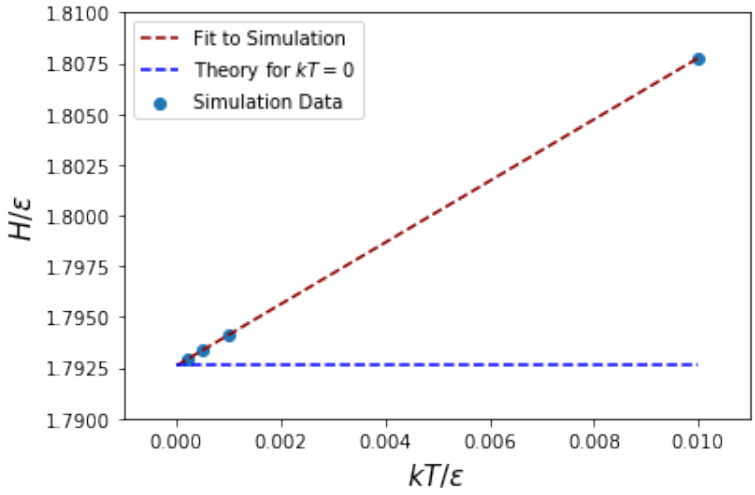

Figure 4.8: The enthalpy of a system of IPL spheres with $n = 12$ in an FCC crystal at low temperatures and a pressure of $1\epsilon/\sigma^3$. The light blue points indicate enthalpies computed for the system from simulations at different temperatures. The red dotted line is a fit to the simulation data, and is extrapolated to 0. The blue dotted line indicates a theoretical calculation of the enthalpy from Equation 4.27 using prior knowledge of the first 6 coordination shells of FCC. Simulation results were obtained for an FCC crystal of 2048 particles. Error bars for the 4 simulation measurements are smaller than the data points.

Low Temperature Behavior of Inverse Power Law Model

While we derived Equation 4.27 analytically, here we present some small simulation results showing that the enthalpy of our systems actually proceeds towards the predicted value for low temperature. We again use NPT simulations executed with the HOOMD-blue simulation toolkit, computing the enthalpy of an FCC crystal composed of IPL spheres with $n = 12$ at $P\sigma^3/\epsilon = 1$ and temperatures approaching 0. In Figure 4.8, we compare our simulation results with those from our theoretical expression, finding strong agreement. This is to be expected, as Equation 4.27 should be exact.

4.6.3 Visualizations of Unusual Structures

Here we present visualizations of structures not found in the ICSD.

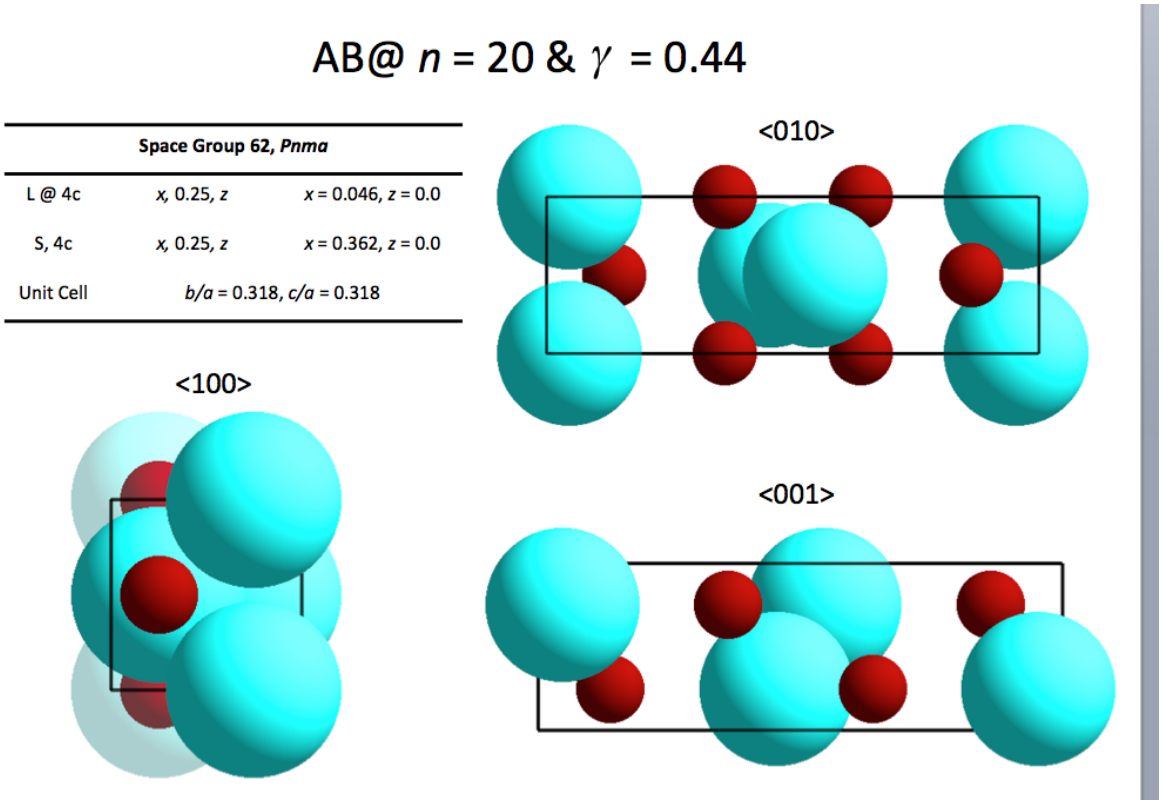

Figure 4.9: The unit cell of the AB structure from the main text. The parameters will change slightly at different n and γ.

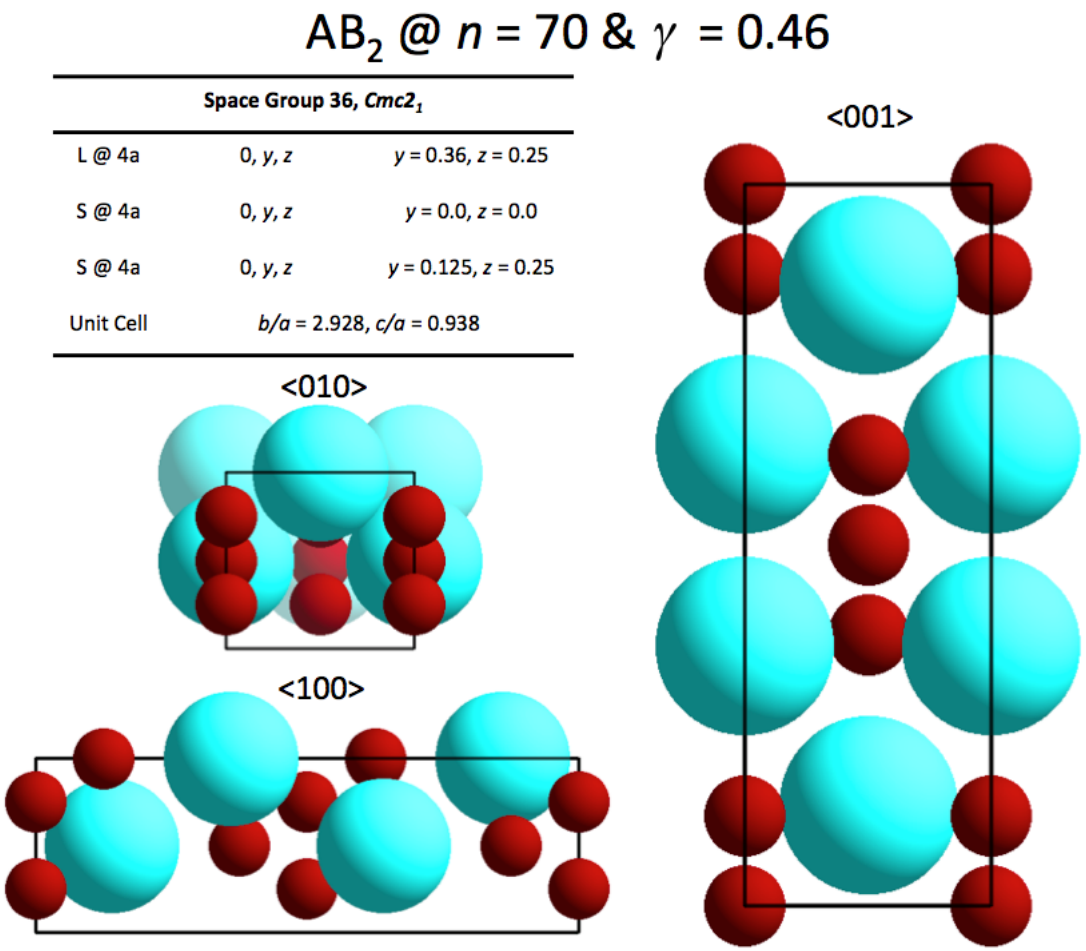

Figure 4.10: The unit cell of the AB_2 structure from the main text. The parameters will change slightly at different n and γ.

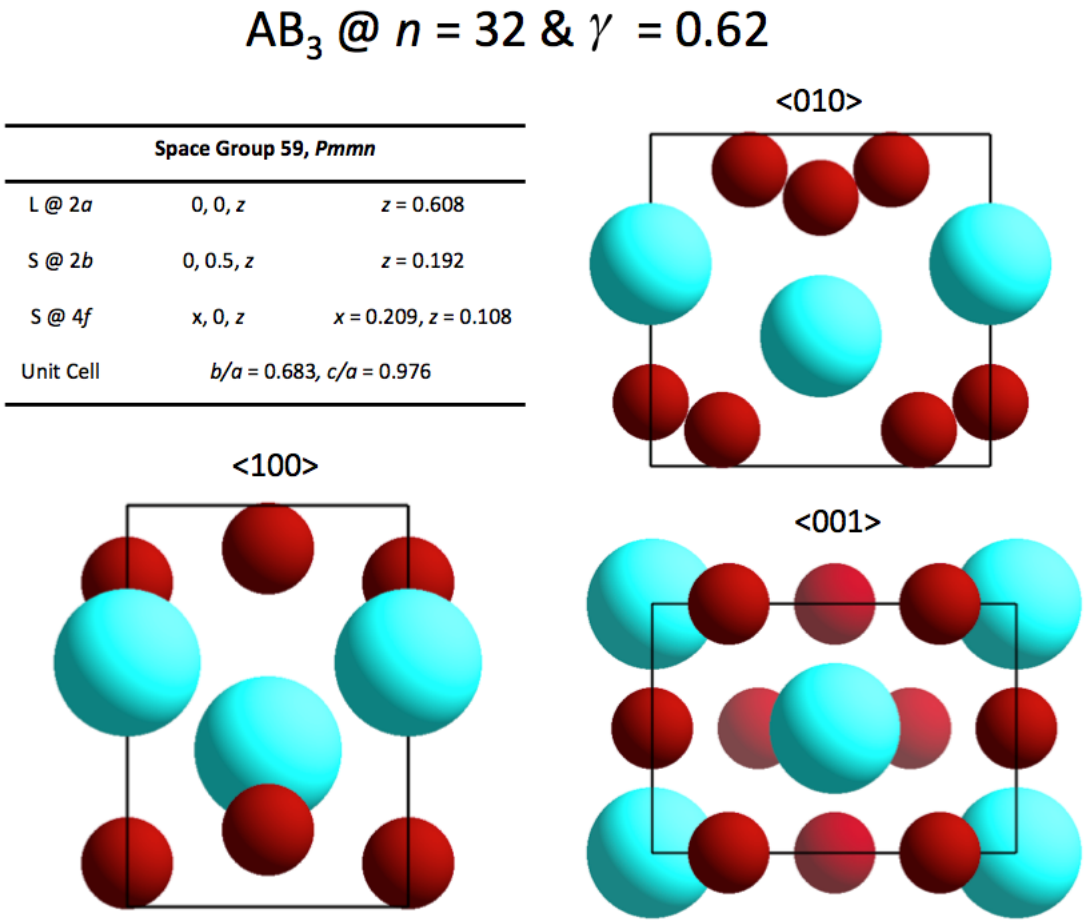

Figure 4.11: The unit cell of the AB_3 structure from the main text. The parameters will change slightly at different n and γ.

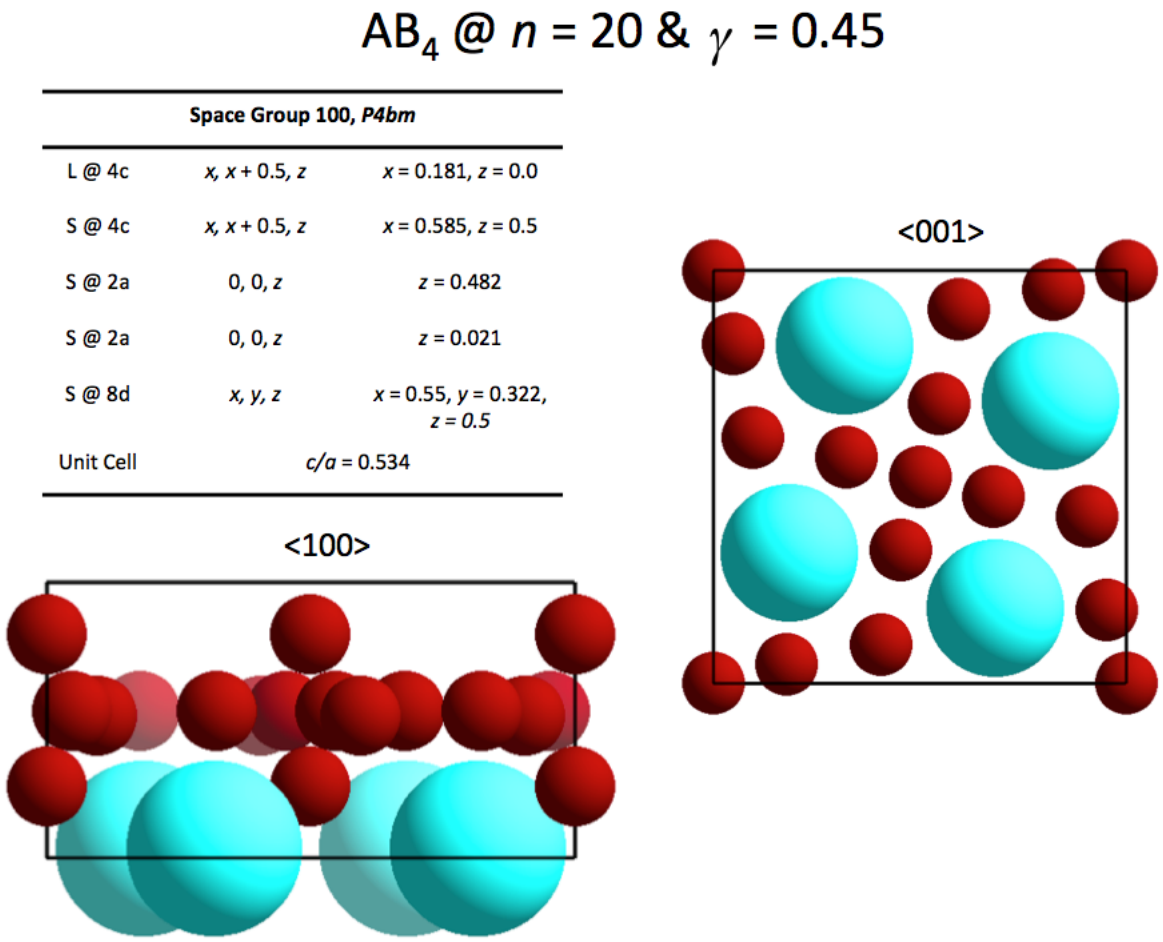

Figure 4.12: The unit cell of the AB_4 structure from the main text. The parameters will change slightly at different n and γ.

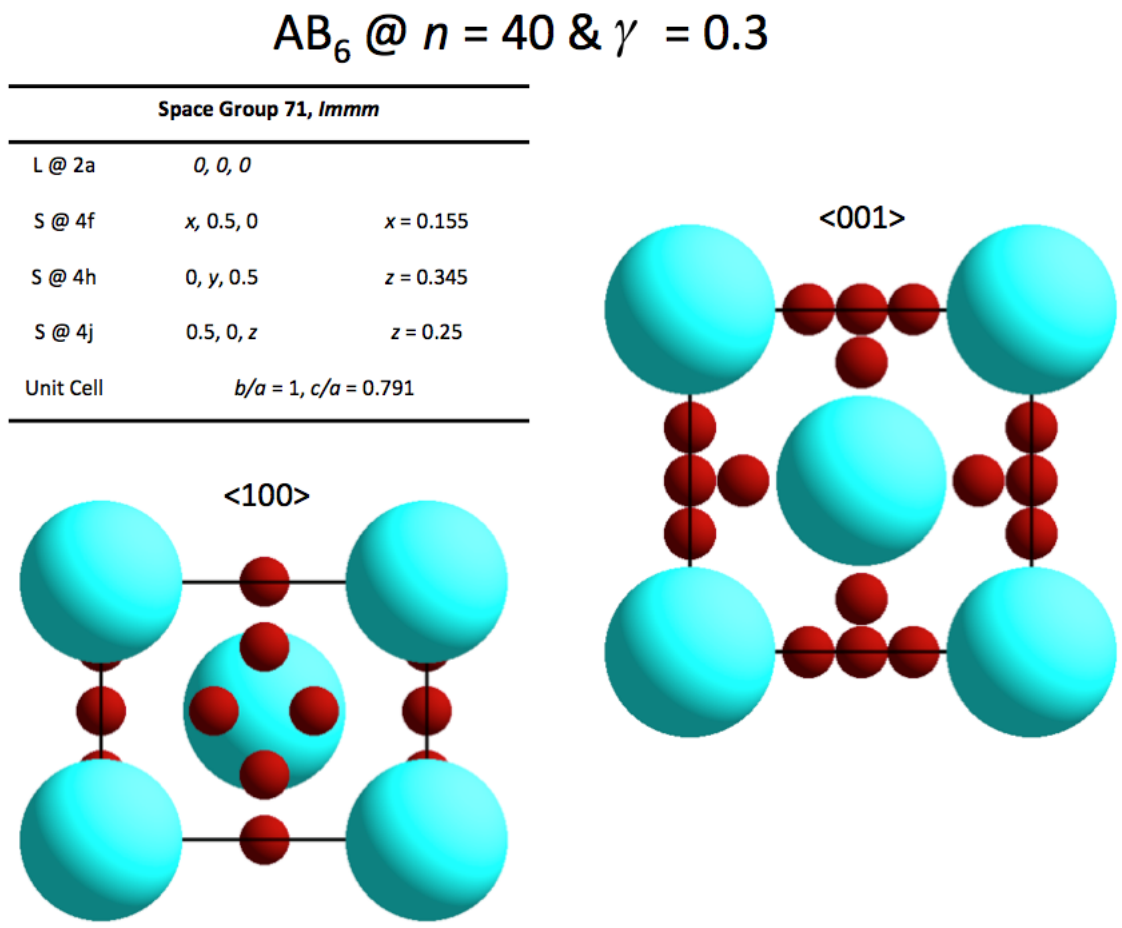

Figure 4.13: The unit cell of the AB_6 structure from the main text. The parameters will change slightly at different n and γ.

CHAPTER V

Tuning Stoichiometry to Promote Formation of Binary Colloidal Superlattices

The contents of this chapter were adapted from "Tuning Stoichiometry to Promote Formation of Binary Colloidal Superlattices." R. A. LaCour, T. C. Moore, S. C. Glotzer, *Submitted*.

5.1 Introduction

Binary colloidal mixtures are known to self-assemble into a diverse array of binary superlattices, providing a simple way to prepare colloidal co-crystals with novel combinations of properties. In many cases, including with polymer beads[18], microgel particles[26], metal nanoparticles[22, 35], and quantum dots[77], mixtures of particles differing only in their sizes can produce a compositionally ordered superlattice[76, 16, 18, 87, 95].

The structure of the superlattice dictates important material properties, *e.g.* photonic response [15] and catalytic activity[31]; thus much effort has focused on designing particles that self-assemble particular colloidal crystal structures [49, 131, 132, 133, 47, 134, 135, 49, 131, 136]. However, less well understood is how to ensure that the equilibrium structure is kinetically accessible *via* self-assembly. The self-assembly of co-crystal phases appears particularly susceptible to kinetic limitations, as these phases frequently fail to assemble, instead forming glasses[137, 138, 139], or assemble into metastable phases[140, 141]. Glass formation is expected when assembly kinetics are slow relative to particle mobility;

metastable phases are expected when the equilibrium phase has slower assembly kinetics than thermodynamically competing phases.

Many colloidal systems are characterized by purely repulsive or hard (excluded volume) interparticle interactions, including some micron-sized colloidal spheres, polymer microgels, and nanoparticles. Because their interactions are well characterized[142, 84, 143], they are especially useful for comparing experiment with theory[95]. Binary mixtures of purely repulsive (hard) particles are known to resist self-assembly in many instances[144, 139, 145], but their self-assembly has been observed in experiments under certain conditions[18, 123, 81, 26]. Understanding why self-assembly occurs in some situations but not others is necessary for further advances.

In this Letter, we demonstrate using computer simulation that variation of the stoichiometry can enhance the kinetics of co-crystal self-assembly in binary mixtures whose components differ in size. Self-assembly of binary crystals is usually attempted "on-stoichiometry," in which the initial fluid phase has the same stoichiometry as the target crystal[146, 108, 145, 139, 147]. We show that going "off-stoichiometry" by adding an excess of the smaller component can dramatically improve self-assembly. We demonstrate that this enhancement can be attributed to two mechanisms, both of which we observe in our simulations. Specifically, we show that the excess of small particles (i) enables the large component to remain mobile at higher supersaturation, facilitating self-assembly of the equilibrium structure and avoiding kinetic arrest; and (ii) can disfavor competing structures that may interfere with the growth of the equilibrium structure.

5.2 AlB_2 Self-Assembly

We first investigate a binary inverse power law (IPL) system at a size ratio (γ) of 0.55, similar to many experiments[16, 18, 123, 22]. Setting the power n to 50 makes the particles similar in softness (steepness of repulsion with interparticle distance – less steep is softer) to some experimental microgels[26] but slightly softer than most PMMA

beads[85]. We make them slightly soft so as to be able to use standard molecular dynamics (MD) algorithms; from our previous work[59] and the phase diagram computed here, we do not expect their phase behavior to deviate significantly from hard spheres. We used HOOMD-Blue[148, 66] to conduct, freud[149] to analyze, and signac[73] to organize the MD simulations. We describe stoichiometry throughout this work in two ways: using the ratio N_L:N_S, where N_L and N_S are the number of large and small particles respectively, or using the fraction of small particles $x_S = N_S/(N_L + N_S)$.

Via free energy calculations[70, 71], we computed the thermodynamic phase diagram of the binary IPL model at $kT/\epsilon = 1$, as shown in Figure 5.1, plotted in terms of reduced pressure $P^* = P\sigma^3/\epsilon$ and x_S, where ϵ and σ are the energy and length scales of the IPL. Because of comparable experimental[18] and simulation[87] studies, we considered the following candidate phases: a face-centered cubic crystal of the large particles (FCC_L), a face-centered cubic crystal of the small particles (FCC_S), an AlB_2 co-crystal, and a $NaZn_{13}$ co-crystal. Their stoichiometries N_L:N_S are 1:0, 0:1, 1:2, and 1:13, respectively.

The phase diagram tells us the equilibrium phase(s) for a given set of conditions, but does not tell us whether the phases are kinetically accessible. For self-assembly to occur, the average time for another phase to nucleate and grow must be shorter than the time accessible in experiment (or simulation). Both nucleation and growth rates are strongly influenced by the degree of supersaturation. For a fluid-to-solid transition, increasing the degree of supersaturation has contrasting effects: the free energy barrier for nucleation decreases, favoring assembly, but the particle mobility decreases, disfavoring assembly[150]. If the mobility decreases too much before the free energy barrier becomes surmountable, the particles become kinetically arrested, inhibiting the formation of the equilibrium solid phase.

We first investigate whether AlB_2 will homogeneously nucleate from a fluid for a variety of pressures and stoichiometries. The simulations were initialized in a fluid-like state with 27,000 particles at constant temperature T and pressure P (i.e., an NPT ensemble), and

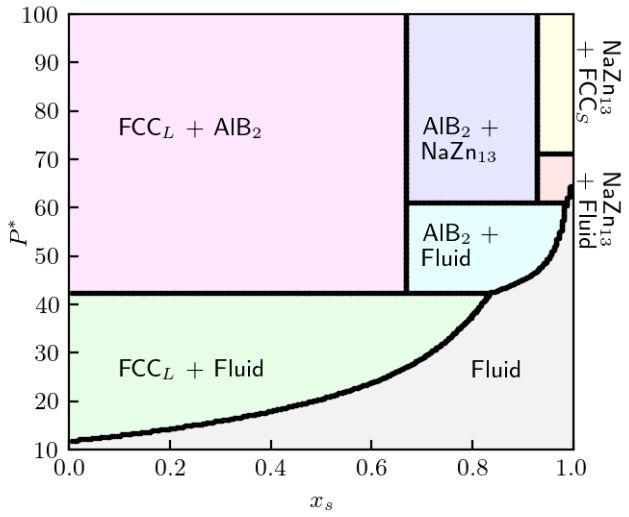

Figure 5.1: Thermodynamic phase diagram for the binary inverse power law model (IPL) at $\gamma = 0.55$, $n = 50$, and $kT/\epsilon = 1$. Five phases are present: fluid, FCC_L, FCC_S, AlB_2, and $NaZn_{13}$. Together they form 7 distinct regions.

run for $4{\cdot}10^5\tau$ timesteps, where $\tau = \sigma(m/\epsilon)^{1/2}$ and m is particle mass. Because we observed some crystal growth at N_L:N_S = 1:3 and $P^* = 70$ and wanted to verify that the crystal continued to grow, we continued that simulation for an additional $4{\cdot}10^5\tau$ timesteps. In Figure 5.2a we show the evolution in the number of AlB_2-like particles up to 200 particles to observe the initial growth of the co-crystal nuclei.

Figure 5.2a shows that N_{AlB_2} never exceeds 16 for the on-stoichiometry systems at the chosen pressures, indicating that self-assembly never occurs. In contrast, we find that N_{AlB_2} increases to 200 and beyond for systems with an excess of small particles. The results are consistent with the system snapshots shown in Figures 5.2c-e, where crystals grains are only apparent at 1:3 and 1:5. We note the presence of small grain sizes, which mirrors the results obtained by Bommineni et al. with particle swap moves[151] in binary mixtures of hard spheres. At the highest pressure we simulated for N_L:N_S = 1:2 ($P^* = 74$), particle mobility is extremely limited, as shown in Figure 5.2b where we plot the temporal decay of the first peak ($q*$) in the intermediate scattering function calculated for the large particles ($F_{LL}(t)$). We thus conclude that self-assembly is only possible with an excess of small particles on the time scale of our simulations. We attribute this result in part to particles being more mobile at higher x_s. For example, by fitting the decay of

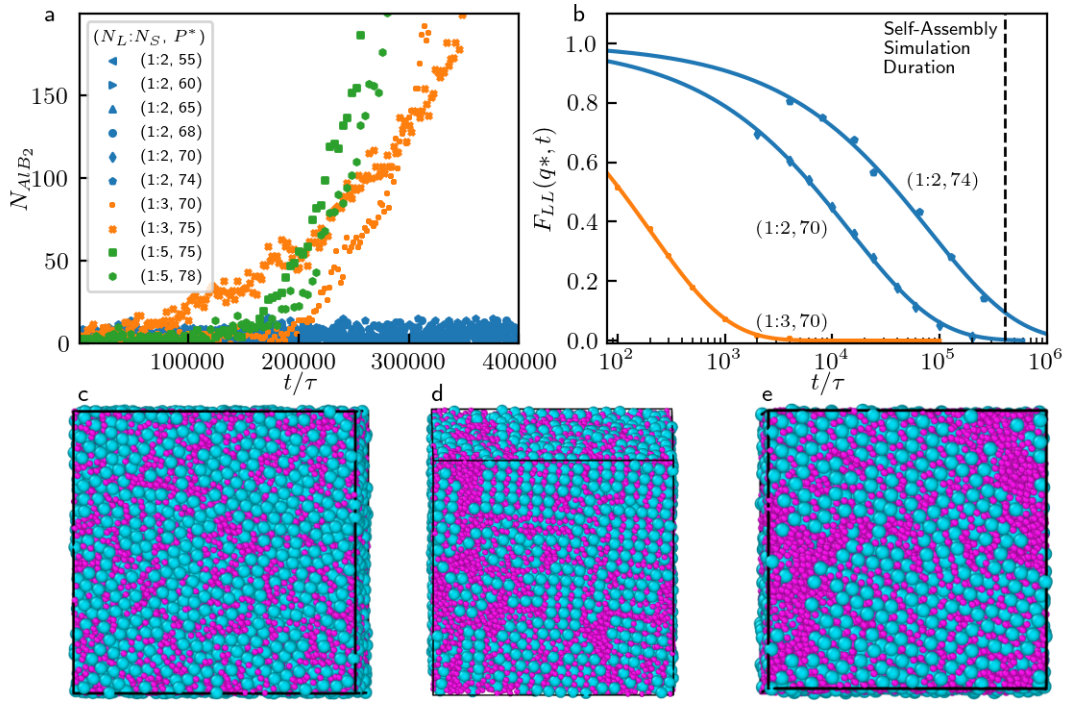

Figure 5.2: Self-assembly of AlB_2. The plot in a) shows the evolution of the number of large particles identified as AlB_2 for NPT simulations at the given pressure and stoichiometry. All simulations at $N_L{:}N_S$ = 1:2 (colored blue on the plot) overlap substantially because they never exceed $N_{AlB_2} = 16$. The plot in b) shows the decay of the intermediate scattering function for certain combinations of stoichiometry and pressure. The lines are fits to the data. The dotted black line indicates the duration of simulations in a). Snapshots of the results are shown for stoichiometries and pressures of c) $N_L{:}N_S$ = 1:2, $P^* = 70$, d) $N_L{:}N_S$ = 1:3, $P^* = 70$, and e) $N_L{:}N_S$ = 1:5, $P^* = 75$. The simulations all began in a fluid state.

$F_{LL}(t)$ to a stretched exponential (indicated by the lines in Figure 5.2b), we computed that the structural relaxation time is around 76 times longer at a stoichiometry of 1:2 than at 1:3 (14,700τ versus 202τ) at $P^* = 70$, which indicates much slower equilibration at 1:2.

We next analyze the growth of AlB_2 in the presence of crystalline seeds. By construction, these simulations bypass the need to form a critical nucleus and thus may allow self-assembly on shorter time scales than required for homogeneous nucleation. Each simulation was prepared by compressing a fluid around a perfect (constructed) seed of AlB_2 and then allowing the fluid and seed to evolve in an NPT simulation. The seed crystals were chosen to be small but post-critical, as evidenced by their persistence in the simulations.

igure 5.3a shows the evolution of the fraction of large particles classified as AlB_2-like (N_{AlB_2}/N_{Total}). We consistently find more crystal growth off-stoichiometry at N_L:N_S = 1:3, with final values of N_{AlB_2}/N_{Total} ranging from 0.25 to 0.48, than on-stoichiometry, for which N_{AlB_2}/N_{Total} never rises above 0.035.

Inspection of the growing seeds at N_L:N_S = 1:2 revealed the accumulation of non-AlB_2 layers of particles on the seed (an example at $P^* = 55$ is shown in Figure 5.3b). We identified many of these layers to be two (or more) subsequent close-packed planes of large particles. This possibility seemed likely because FCC_L, which consists of close-packed planes, is metastable under the conditions we investigate, and AlB_2 has a close-packed layer of large particles in its structure onto which additional close-packed layers could grow. We call a layer of these particles a "mixed layer" and the associated coordination environment "mixed FCC-AlB_2;" we denote the number of these particles N_{mix}. In Figure 5.3b we illustrate their presence in dark green for a seed grown at $P^* = 55$ and N_L:N_S = 1:2.

We quantify the formation of the mixed layer during the seeded simulations in Figure 5.3c, plotting N_{mix}/N_{AlB_2} versus N_{AlB_2}. For N_L:N_S = 1:2 we plot only the results for

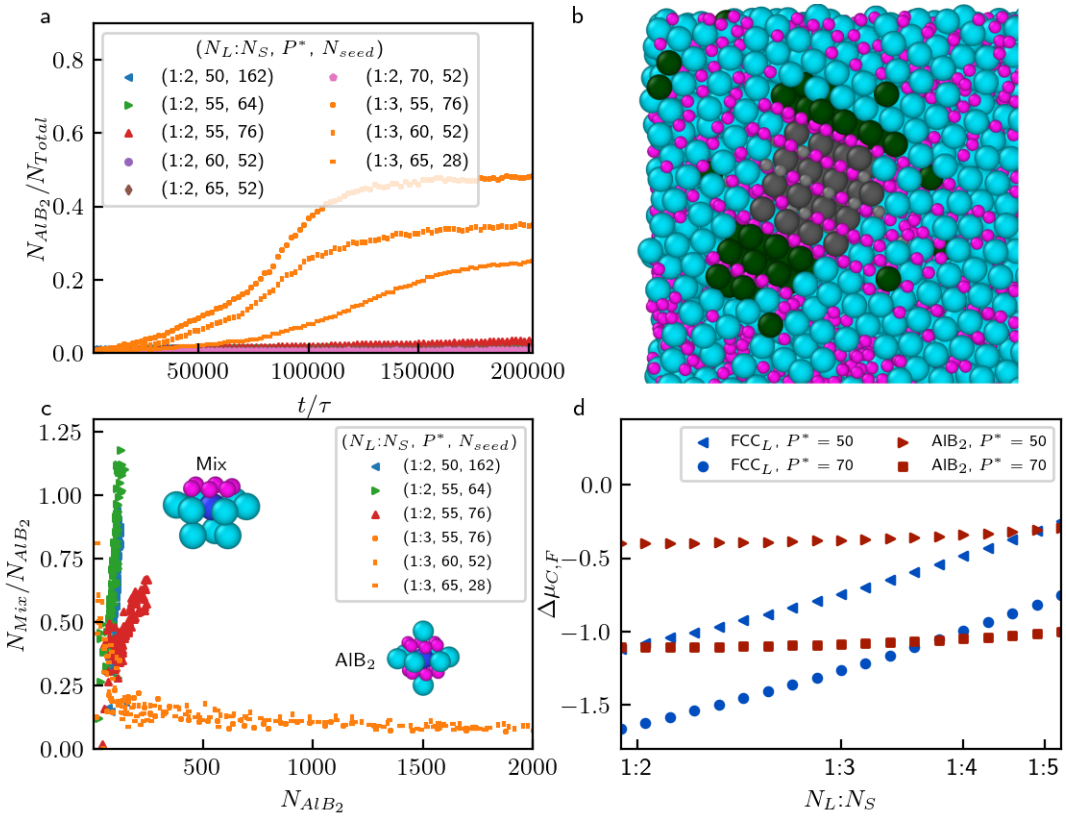

Figure 5.3: Crystal growth in seeded simulations. The plot in a) shows the evolution of the number of large particles identified as AlB_2 from seeded simulations for different x_s, $P\sigma^3/\epsilon$, and initial seed size (N_{seed}). The image in b) is a snapshot of the end of the seeded simulation at $N_L{:}N_S$ = 1:2 and $P\sigma^3/\epsilon = 55$. Large and small particles belonging to the initial seed are colored dark grey and light grey, respectively, respectively; large particles classified as mixed FCC-AlB_2 are colored dark green. The plot in c) shows the number of particles classified as AlB_2 (N_{AlB_2}) versus the ratio of the number classified as mixed FCC-AlB_2 to N_{AlB_2} (N_{Mix}/N_{AlB_2}). The two inset figures illustrate the mixed FCC-AlB_2 and AlB_2 environments. The plot in d) shows the chemical potential driving force $\Delta\mu_{C,F}$ for the FCC_L and AlB_2 as a function of pressure and stoichiometry, where $\Delta\mu_{C,F}$ is defined by Equation 5.1. Errors are smaller than the size of the points.

$P\sigma^3/\epsilon \leq 55$ because at higher pressures N_{AlB_2} never exceeds 100 (*i.e.*, those seeds grow negligibly over the simulation). Off-stoichiometry at N_L:N_S = 1:3, the proportion of mixed layers decreases with crystal growth in all cases. In contrast, on-stoichiometry at 1:2 the proportion always increases, indicating that mixed layers form more frequently than AlB_2 layers.

We identify a thermodynamic reason as to why the mixed layers are more prevalent at N_L:N_S = 1:2. Because the mixed layer is essentially the formation of an FCC layer where an AlB_2 layer should have formed, its appearance likely correlates with the thermodynamic stability of the competing FCC_L phase. In Figure 5.3d we examine the chemical potential difference between the particles in the fluid and the solid:

$$\Delta\mu_{C,F} = \mu_C - (1 - x_C)\mu_F^L - x_C \cdot \mu_F^S \tag{5.1}$$

The quantity μ_C is the chemical potential of the crystal; x_C is the fraction of small particles in the crystal; and μ_F^L and μ_F^S are the chemical potentials of the large and small species in the fluid, respectively. More negative $\Delta\mu_{C,F}$ values indicate stronger thermodynamic driving forces for nucleus formation.

Figure 5.3d shows that the $\Delta\mu_{C,F}$ of both crystals decreases with pressure but increases with a greater proportion of small particles. However, we find that $\Delta\mu_{FCC_L,F}$ is more sensitive to stoichiometry than $\Delta\mu_{AlB_2,F}$. For example, at $P^* = 70$, changing the stoichiometry from 1:2 to 1:3 increases the $\Delta\mu_{C,F}$ of FCC_L by 0.37 kT while only increasing the $\Delta\mu_{C,F}$ of AlB_2 by 0.02 kT, resulting in a greater preference of the fluid to form AlB_2 relative to FCC_L.

To summarize these results, we find that AlB_2 does not self-assemble or even grow from a seed crystal in on-stoichiometry fluid. We identified two reasons its formation is inhibited: slow dynamics and interference from a competing phase. Both issues are alleviated by adding excess small particles.

Table 5.1: Crystals Observed in Simulation and Experiment

N_L:N_S	Sim. Structures	Exp. Structures*
1:2	Amorphous	Amorphous
1:3	AlB_2	-
1:4	AlB_2	AlB_2
1:5	AlB_2	-
1:6	AlB_2	AlB_2
1:9	AlB_2/$NaZn_{13}$	$NaZn_{13}$
1:13	$NaZn_{13}$	-
1:14	$NaZn_{13}$	$NaZn_{13}$
1:20	$NaZn_{13}$	$NaZn_{13}$
1:30	$NaZn_{13}$	$NaZn_{13}$

*Bartlett et al.[18]

5.3 Experimental Comparison

Our simulations should be most comparable with the experiments of Bartlett et al.[142, 18] using PMMA particles because our results are for a similar size ratio (0.55 vs. 0.58) and they explore how stoichiometry affects assembly. In Table 5.1, we compare the binary crystals we obtain with theirs. Our results at N_L:N_S of 1:2, 1:3, 1:5, are shown in Figure 5.2; results for the other stoichiometries are shown in the section 5.7. We denote any experiment not reported with "-".

Overall, we see strong agreement between simulation and the published experimental results. We both obtain an amorphous structure at 1:2, but see AlB_2 with a slight excess of small particles. Around a stoichiometry of 1:9, we both begin to see $NaZn_{13}$ self-assemble, and continue to see it self-assemble at stoichiometries up to 1:30.

5.4 Binary Shapes

To establish whether the self-assembly of other binary crystals may be assisted by an excess of small particles, we also simulated a binary mixture of hard cuboctahedra and octahedra at a volume ratio of 5:1, which has proven difficult to crystallize despite being capable of comprising a space-filling CsCl-type structure.[146] Like the IPL spheres, the particles in this system are purely repulsive (hard). To our knowledge, the CsCl structure has never been self-assembled from these hard shapes; in previous work, attractive patches on the particles' surface were required for self-assembly[152]. In Figure 5.4, we present

our results for self-assembly conducted at stoichiometries of 1:1 and 1:2. Due to the higher computational cost of simulating anisotropic particles[153, 154], we used a slow compression scheme with 4096 particles.

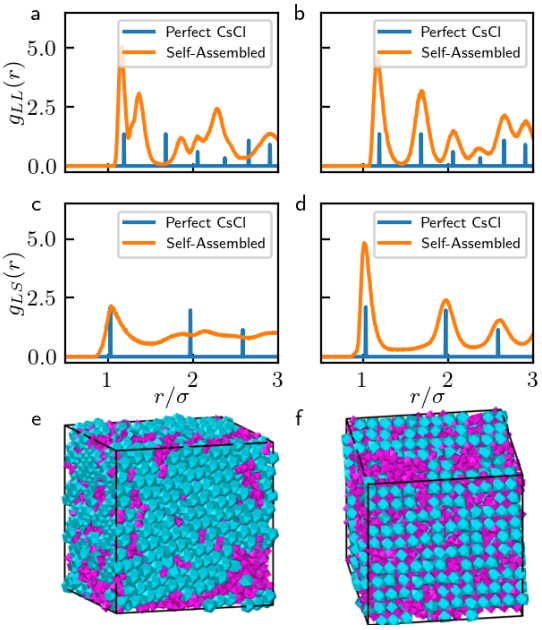

Figure 5.4: The self-assembly of hard cuboctahedra and octahedra. The plots show the radial distribution functions (RDFs) averaged over the final few frames of self-assembly at stoichiometries of a,c) 1:1 and b,d) 1:2. Also shown are the RDFs for a perfect CsCl structure. We show the RDF for large particles (g_{LL}) and for large and small particles (g_{LS}); the RDF for small particles is dominated by fluid-like small particles. Snapshots of the results are shown for e) 1:1 and f) 1:2. Simulations were run in an NPT ensemble with 4096 particles under a slow compression starting at a volume fraction of 0.565.

By comparison with the radial distribution functions of perfect CsCl, we identified the result at 1:2 to be CsCl. At 1:1, a single-component structure composed of the large particles self-assembles, while the small particles remain fluid-like. It is thus apparent that, although particle mobility is not limited, the single-component structure (successfully) competes with CsCl when the fluid is on-stoichiometry, and an excess of small particles is necessary to observe the thermodynamically preferred binary structure.

5.5 Conclusions

In summary, we demonstrated that the self-assembly of binary nanoparticle superlattices can be promoted by adding an excess of the smaller component to the colloidal fluid mixture. While some crystals, like $NaZn_{13}$, do not require an excess of small parti-

cles, the surprisingly dramatic influence of excess small particles on the assembly of AlB_2 and CsCl suggests many other binary systems may best – or only – self-assemble off-stoichiometry. Our results likely apply best to purely repulsive systems; we will examine attractive systems in future work.

5.6 Methods

5.6.1 Simulation Details

We used molecular dynamics (MD) with the HOOMD-Blue simulation toolkit[65, 66] to study the binary inverse power law (IPL) potential with power $n = 50$:

$$U(r_{ij}) = \epsilon\left(\frac{\sigma_{ij}}{r_{ij}}\right)^{50}. \tag{5.2}$$

The quantity U is the potential energy of interaction between two particles i and j at a distance of r_{ij}. The quantity σ_{ij} represents the diameter of the particles; for interactions between unlike particles, we set it to their average diameter. We denote the diameter of the large particles as σ and diameter ratio between small and large particles as γ. The unit of energy is ϵ, which is set to 1 temperature unit (kT) throughout this work. The IPL exhibits thermodynamic scaling between temperature and pressure such that a change in temperature can be mapped to an equivalent change in pressure[91]; thus we only need to investigate its behavior at a single temperature. We truncated the potential at a cutoff of $1.3\sigma_{ij}$ and shifted it from an energy of $2.0{\cdot}10^{-6}\epsilon$ at the cutoff to zero.

We used NPT simulations based on the MTK equations[155] to collect data on nucleation from a fluid and growth from a seed and when computing the intermediate scattering function between large particles ($F_{LL}(q,t)$).

We used HOOMD-Blue's Hard Particle Monte Carlo module to simulate the mixtures of cuboctahedra and octahedra. On-stoichiometry simulations at N_L:N_S = 1:1 consisted of a slow compression from a packing fraction of 0.565 to 0.635 in increments of 0.001. Off-stoichiometry simulations at N_L:N_S = 1:2 consisted of a slow compression from a packing fraction of 0.565 to 0.615 in increments of 0.001. We compressed to a higher

packing fraction at N_L:N_S = 1:1 because the system had not finished crystallizing at 0.615, while the system at N_L:N_S = 1:2 was crystalline by that packing fraction.

Free energy calculations were performed with HOOMD-blue to obtain the phase diagram shown in Figure 2. Pressure-Volume (PV) data were gathered for the fluid and solid phase from NVT and NPT simulations respectively. Free energies at different $P\sigma^3/\epsilon$ were computed by integrating curves fit to the PV data. The reference free energy for the fluid was taken to be that of a dilute gas; the reference free energy for the solid was computed from the Einstein molecule method[71], a variant of the Frenkel-Ladd method[70] in which a single particle is fixed instead of the center of mass. By comparing free energies differences computed by PV integration to those from two Einstein molecule method calculations, we estimated our errors to be below 0.05 kT. The Langevin integrator[156] within HOOMD-Blue was used when performing the Einstein molecule method.

We used Steinhardt order parameters[157] to classify particles as having AlB_2, mixed FCC-AlB_2, or fluid environments. The freud software library[149] was used to calculate radial distribution functions and Steinhardt order parameters. We used Ovito[72] to visualize particles throughout the work.

The computational workflow was supported by the signac data management framework [73].

5.6.2 Order parameter

We use Steinhardt order parameters to classify particles according to their coordination environment. We show in Figure 5.5 that a combination of two order parameters can distinguish whether large particles are in fluid, AlB_2 (Figure 5.5a), or "mixed FCC-AlB_2" (Figure 5.5b) environments, which we show to be a common defect during AlB_2 self-assembly. The black lines in Figure 5.5c show how we classify particles with specific q_6^{LL} and $q_8^{LL,LS}$ into the three environments. For the mixed FCC-AlB_2 environments, we simulated a structure involving alternating layers of a hexagonally close packed crystal and AlB_2 crystals and computed the order of the particles at the interface; a visualization

of the structure is shown in Figure 5.6. We note that our order parameter will somewhat underestimate the number of crystalline particles because it does not detect particles at the edges of crystal grains. We computed that our order parameter misclassified particles in the fluid with a rate under 0.25%.

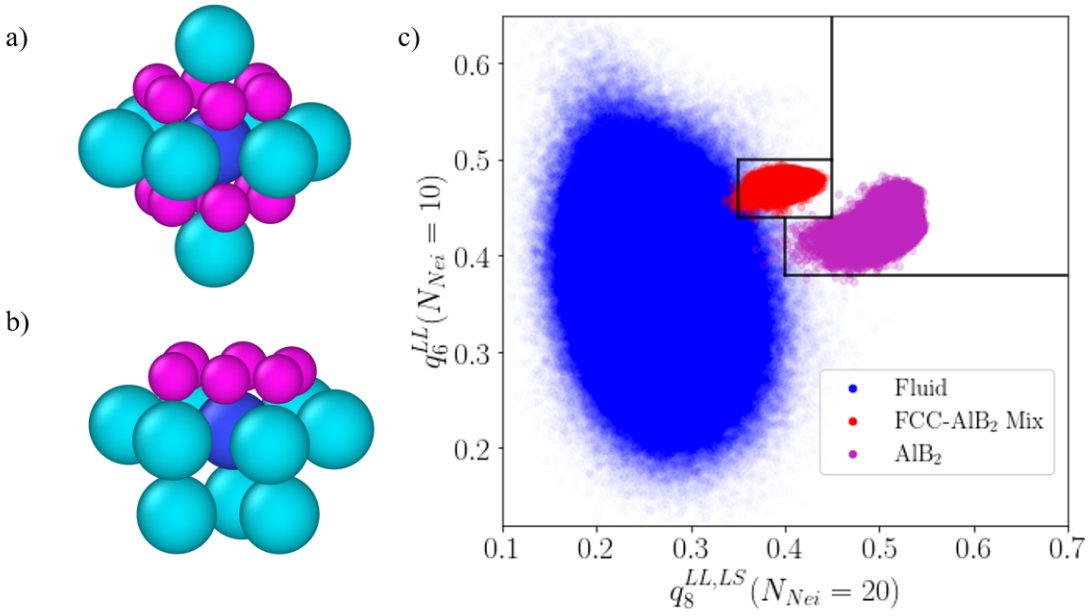

Figure 5.5: The coordination of large particles in a) AlB_2 and b) mixed FCC-AlB_2 environments; c) the Steinhardt order parameters of large particles in those environments and a fluid environment at N_L:N_S = 1:2. In a) and b) the reference particle is colored dark blue We use the Steinhardt order parameter q_8 for the first 20 neighbors (the number of neighbors of each large particle in the perfect AlB_2 crystal) of either type, and the q_6 for the first 10 *large* neighbors. The data for AlB_2 and mixed FCC-AlB_2 were generated from simulations of pre-assembled versions of the structures. The structure used for mixed FCC-AlB_2 is shown in Figure S4. The black lines in c correspond to how we classified particles. The distribution of order parameters shown in c) is computed at $P^* = 60$.

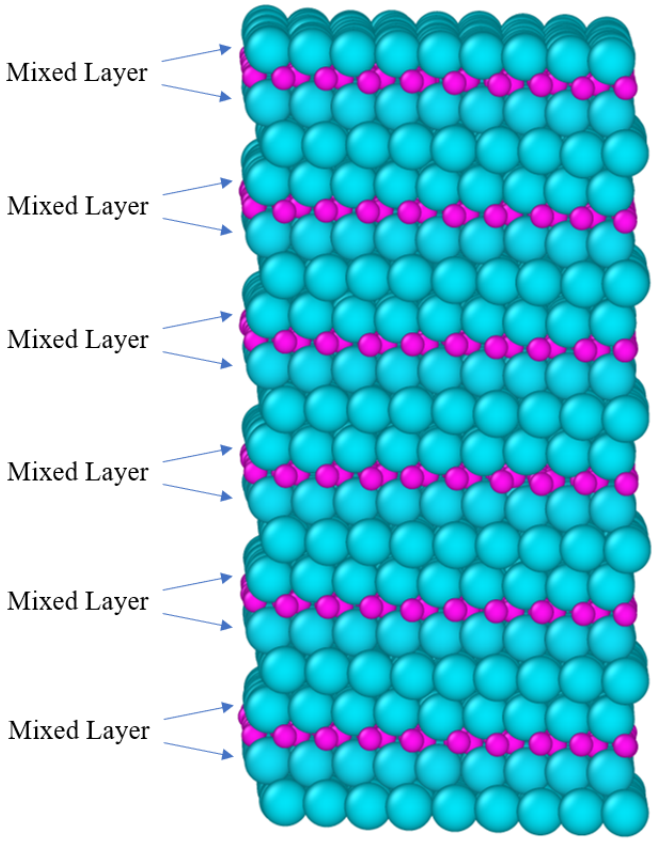

Figure 5.6: Snapshot of the structure we used to determine the order parameter for "mixed FCC-AlB_2" environments. We only computed the order parameter for layers denote "Mixed Layer".

5.7 Supplement

We present RDFs and snapshots for our results at each stoichiometry in Figures 5.7 to 5.9.

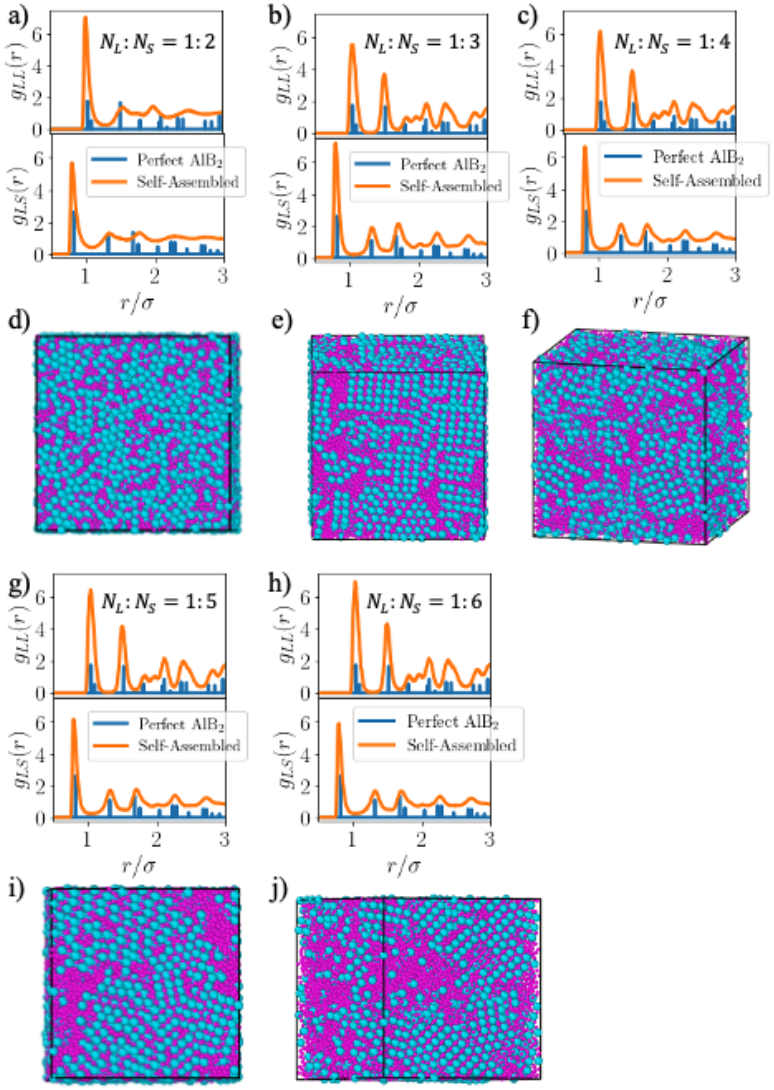

Figure 5.7: Radial distribution functions (RDFs) and and snapshots of NPT simulation results at (a,d) N_L:N_S = 1:2, P^* = 70, (b,e) N_L:N_S = 1:3, P^* = 70, (c,f) N_L:N_S = 1:4, P^* = 78, (g,i) N_L:N_S = 1:5, P^* = 75, and (h,j) N_L:N_S = 1:6, P^* = 80. These simulations all began in a fluid-state. The RDFs are averaged over the final 5 frames of the simulations; the snapshots are the last frames of the simulations. We only show the RDFs for large-large and large-small interactions because that of small-small interactions tends to be dominated by fluid-like small particles. At both stoichiometries, we see crystal grains in both the snapshots and the RDFs. Visual inspection and comparing the RDFs to the perfect ones for AlB_2 show the crystal structure to be that of AlB_2.

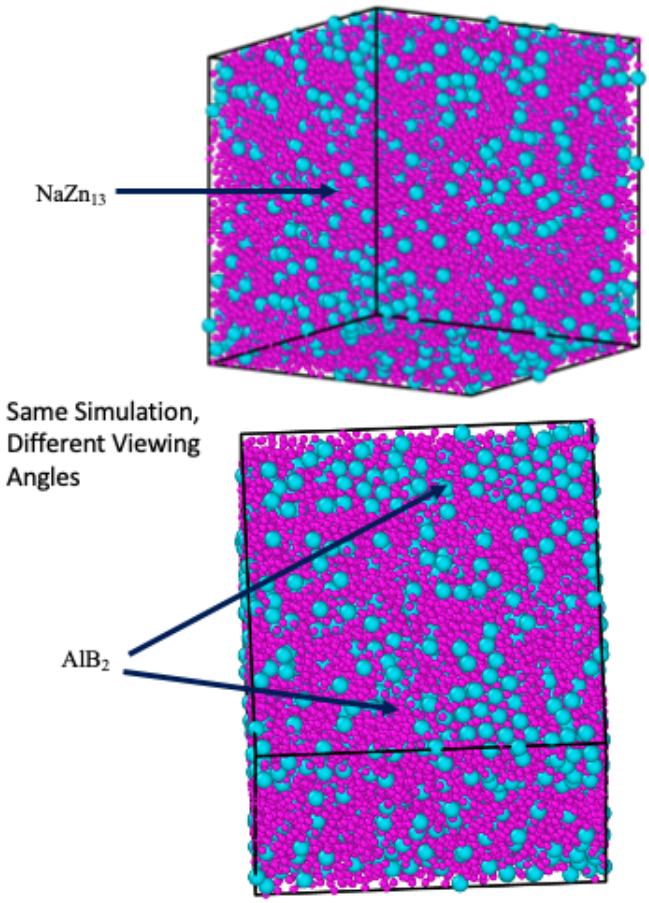

Figure 5.8: Snapshots showing different angles of an NPT simulation run at N_L:N_S = 1:9 and $P^* = 98$. The simulation began in a fluid-state. Both AlB_2 and $NaZn_{13}$ self-assemble in the simulation, as point out by the arrows. The crystal grains are small in both cases.

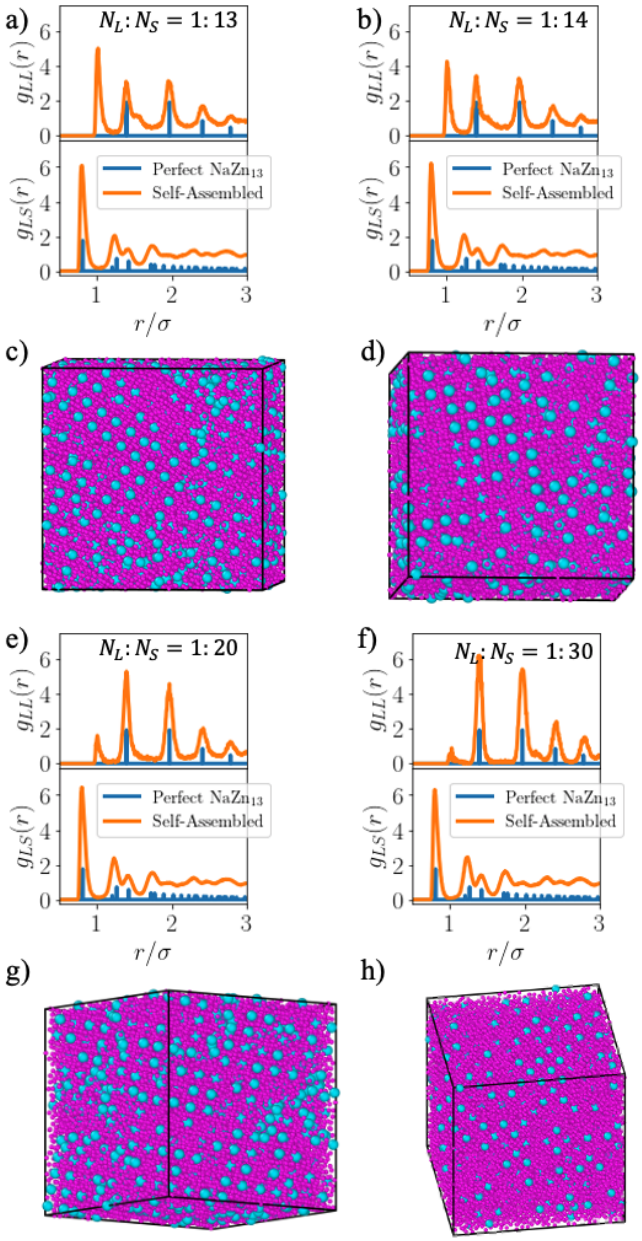

Figure 5.9: Radial distribution functions (RDFs) and and snapshots of NPT simulation results at (a,c) N_L:N_S = 1:13, P^* = 98, (b,d) N_L:N_S = 1:14, P^* = 98, (e,g) N_L:N_S = 1:20, P^* = 98, and (f,h) N_L:N_S = 1:30, P^* = 98. These simulations all began in a fluid-state. The RDFs are averaged over the final 5 frames of the simulations; the snapshots are the last frames of the simulations. We only show the RDFs for large-large and large-small interactions because that of small-small interactions tends to be dominated by fluid-like small particles. At both stoichiometries, we see crystal grains in both the snapshots and the RDFs. Visual inspection and comparing the RDFs to the perfect ones for $NaZn_13$ show the crystal structure to be that of $NaZn_13$. We note presence of an unexpected peak at $r/\sigma = 1$; this is due to large particles in contact with each. There are no such contacts in perfect $NaZn_13$, but they occur in our self-assembly due to some large particles not being incorporated into the crystal.

CHAPTER VI

Short-Range Attraction Enables the Self-Assembly of Binary Nanoparticle Superlattices

The contents of this chapter were adapted from "Short-Ranged Attractive Forces Enable the Self-Assembly of Binary Nanocrystal Superlattices.", E. Marino, R. A. LaCour, T. C. Moore, S. W. Dongen, A. W. Keller, D. An, S. Yang, D. J. Rosen, G. Gouget, E. H. R. Tsai, C. R. Kagan, T. E. Kodger, S. .C Glotzer, C. B. Murray, *Submitted*.

All experimental work (Figures 6.1 and 6.2) was performed by our collaborators in the Murray group.

6.1 Introduction

Recent advances in colloidal synthesis have enabled the fabrication of colloidal nanocrystals (NCs) with different sizes, shapes, and compositions, creating a library of nanoscale building blocks with well-defined optical, electronic, and magnetic properties. These properties have been exploited to develop optoelectronic devices like photodetectors[158, 159], light-emitting diodes[160, 161], field-effect transistors[162, 163], and solar cells[164, 165] by assembling NCs into ordered solids, or superlattices. While single-component NC superlattices have already revealed structure-property relationships[166, 167], multi-component NC superlattices are still in the early stages of investigation[168]. The hetero-integration of NCs with orthogonal functionalities is crucial in unlocking a vast design space for material properties resulting from the synergistic interaction of the individual components[29, 169, 33, 170, 31, 171, 172, 173]. So far, the exploration of this design space

has been restricted by our limited understanding of the formation of multi-component NC superlattices.

Binary nanocrystal superlattices (BNSLs) with diverse crystal structures have been reported, integrating combinations of semiconducting, magnetic, and metallic NCs.[19, 22] However, predicting which BNSL self-assembles from a given combination of NCs has proven extremely challenging[174]. With rare exceptions[145, 175, 147], simulation models of binary mixtures of NCs frequently fail to self-assemble, indicating that the current understanding of NC interactions, and their contribution to BNSL self-assembly, is incomplete. By contrast, experimental *in situ* studies have already revealed the self-assembly mechanism of single-component NC superlattices[176, 177, 178, 179, 180, 181, 182, 183, 184] enabling a priori structure prediction by capturing both kinetic and thermodynamic aspects of how different inter-NC interactions influence self-assembly[185, 41, 186, 121, 43, 20, 175, 187]. Yet, in almost two decades since the first observation of BNSLs[19], only one *in situ* study has been reported for BNSLs of iron oxide NCs[187], and no *in situ* studies have investigated the assembly of different materials into BNSLs.

Here we combine experiments and simulations to understand the formation of BNSLs. We use synchrotron-based *in situ* small-angle X-ray scattering (SAXS) to follow in real-time the self-assembly of two commonly observed BNSLs isostructural to AlB_2 and $NaZn_{13}$. The NCs were confined to emulsion droplets that were slowly dried to trigger crystallization, resolving with unprecedented detail the formation of high-quality BNSLs. This approach was combined with molecular dynamics (MD) simulations to determine the interparticle interactions allowing the formation of these BNSLs. We find that only the presence of a strong, short-ranged attraction between NCs results in a self-assembly behavior consistent with experiment. This short-ranged attraction dramatically accelerates the self-assembly kinetics by stabilizing the crystalline solid phase at low NC densities, resulting in higher crystallization driving forces than possible for the hard-sphere models commonly used in the literature[175, 188]. We next elucidate the early stages of

self-assembly; in contrast to single-component superlattices[176, 178, 179, 189], BNSLs undergo homogeneous nucleation into the final crystal structure without any intermediate phases. By establishing a direct link between experiments and simulations, our work provides crucial insights into the formation of BNSLs and represents a significant step towards a priori structure prediction of these complex, 3D artificial solids.

6.2 Results and Discussion

We conduct self-assembly of binary mixtures of NCs using emulsion-templating[190]. We prepare a surfactant-stabilized oil-in-water emulsion containing a dispersion of larger (L) super-paramagnetic Fe_3O_4 and smaller (S) PbS semiconductor NCs with an effective size ratio of 0.56, a number ratio of 1:2, and a total inorganic volume fraction of ≈ 0.001. To collect *in situ* scattering patterns, we flow the emulsion in a closed loop through a quartz capillary aligned with the X-ray beam. Figure 6.1a illustrates the continuous kinetic evolution of the structure factor, $S(q)$. Initially, the structure factor is featureless and centered around 1, as expected for a colloidal gas. During the first 3 hours drying the emulsion, broad features arise across the wave vector range, q. After 3.6 hours, a succession of sharp peaks suddenly emerges from the background, growing in intensity while shifting with time towards higher q. As highlighted in Figure 6.1b, the shape of the structure factor at 3.6 hours resembles that of a low-density colloidal fluid, but within 0.1 hours rapidly develops into a fully-formed diffraction pattern featuring at least 7 sharp peaks from growing crystallites. Immediately thereafter, all peaks shift synchronously toward higher q, indicating a contraction of the crystal lattice. We identified the crystal as isostructural to AlB_2 with parameters $a = b \approx c$; see Figure 6.1c. This structure is characterized by stacked hexagonal layers of the larger NCs intercalated by hexagonal layers of the smaller NCs that occupy the trigonal prismatic voids left by the larger NCs.

To understand the formation of these BNSLs, we extract the evolution of the structural parameters from the *in situ* measurements as shown in Figure 6.1d. After nucleation,

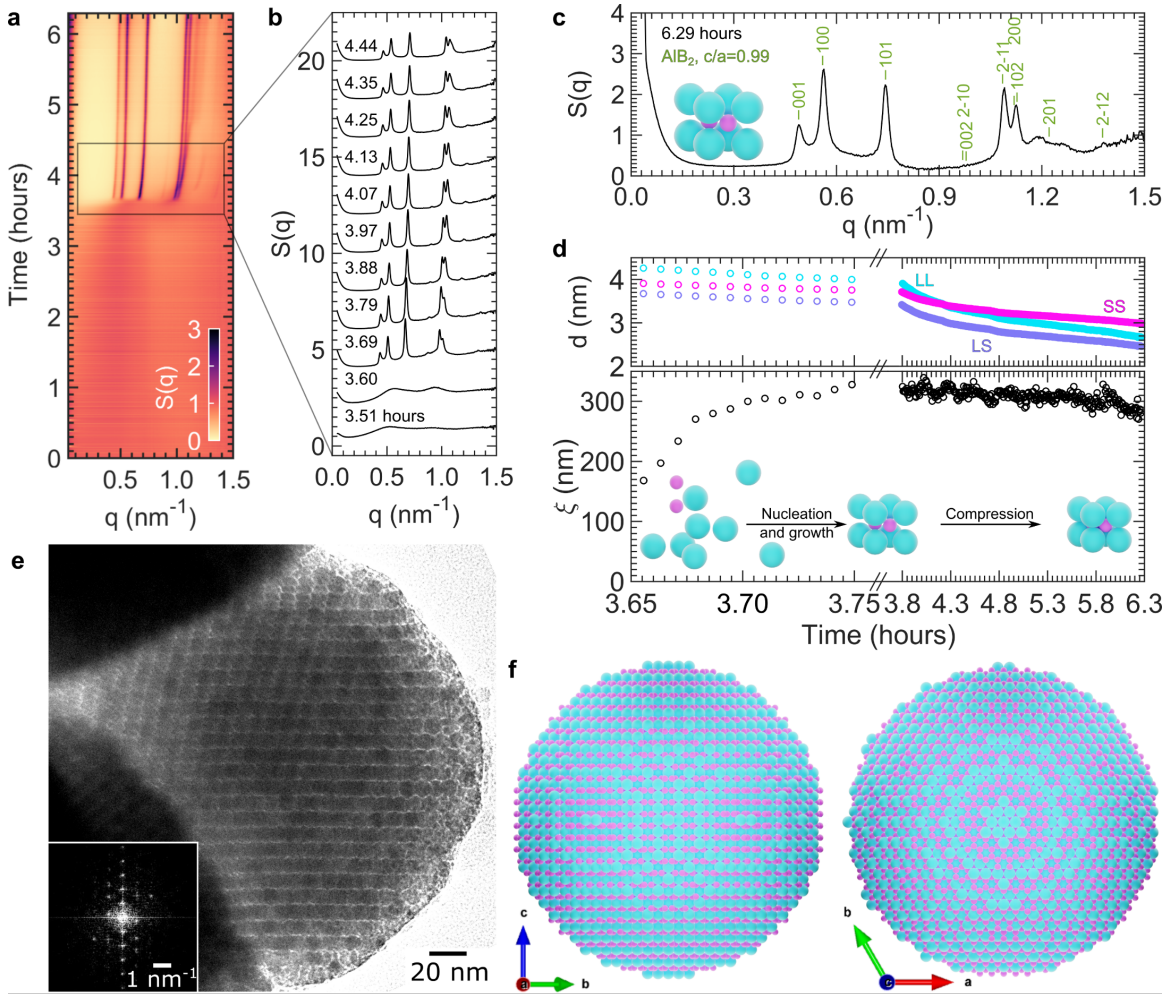

Figure 6.1: Formation of colloidal AlB_2 BNSLs. (a) Kinetic structure factor, S(q), of a binary dispersion of PbS and Fe_3O_4 NCs under spherical confinement of a drying emulsion. (b) $S(q)$ patterns showing the emergence and evolution of diffraction peaks around the time of BNSL nucleation. (c) Final $S(q)$ pattern identifying the BNSL structure as AlB_2. (d) Evolution of the crystalline lattice after nucleation, highlighting the kinetics of surface-to-surface distance between larger (L) and smaller (S) NCs, d (top), and average crystal size, ξ (bottom). The proposed assembly mechanism is shown as inset. (e) TEM micrograph of PbS and Fe_3O_4 NCs crystallized into a 3D AlB_2 BNSL. The fast-Fourier transform is shown as inset. (f) Model of the AlB_2 BNSL shown in (e).

lattice contraction induces a slow decrease in the surface-to-surface distance between NCs, d. This decrease takes place over several hours to reach an inorganic volume fraction of $\phi = 0.357$. In stark contrast to this steady compression of the lattice, the average crystal size extracted from the Scherrer equation[191], ξ, increases rapidly: Within 0.1 hours after nucleation, the crystal size increases to reach $\xi \approx 330$ nm, corresponding to $\xi/a \approx 23$ unit cells of the BNSL. Eventually, the crystal size slowly decreases to $\xi \approx 280$ nm as the result of lattice compression.

Based on these observations, we hypothesize the assembly mechanism shown in the inset of Figure 6.1d: crystallization occurs as a single-step transition from the fluid to the crystalline phase. The relative positions of the diffraction peaks do not change during assembly, implying the absence of intermediate phases between the fluid and the final crystal. This is a simpler process compared to previous reports for single-component NC superlattices reporting crystal-to-crystal transitions[178, 179, 189]. The continuous compression of the BNSL follows crystallization. We attribute this compression to the evaporation-driven desorption of solvent from the ligand shell of the NCs, consistently with reports on single-component systems[176, 178, 192]. The fast-Fourier transform of the BNSL shown in Figure 6.1e reveals a discrete set of spots, as expected for a crystalline structure. Combining *in situ* and *ex situ* experimental results leads to the model shown in Figure 6.1f.

We test the robustness of this approach by using a pair of larger plasmonic CdO NCs co-doped with fluorine and indium (FICO), and smaller semiconductor PbS NCs with comparable size ratio, number ratio, and initial volume fraction: their assembly in emulsion yields the same AlB_2 BNSL structure with similar kinetics. We next target a different BNSL, $NaZn_{13}$, by increasing the number ratio of these FICO and PbS NCs from 1:2 to 1:13. The experimental structure factor reveals the onset of diffraction peaks from the flat background shortly after 2.3 hours of drying. The diffraction pattern appears qualitatively different from Figure 6.1, with at least 10 discernible reflections. A more

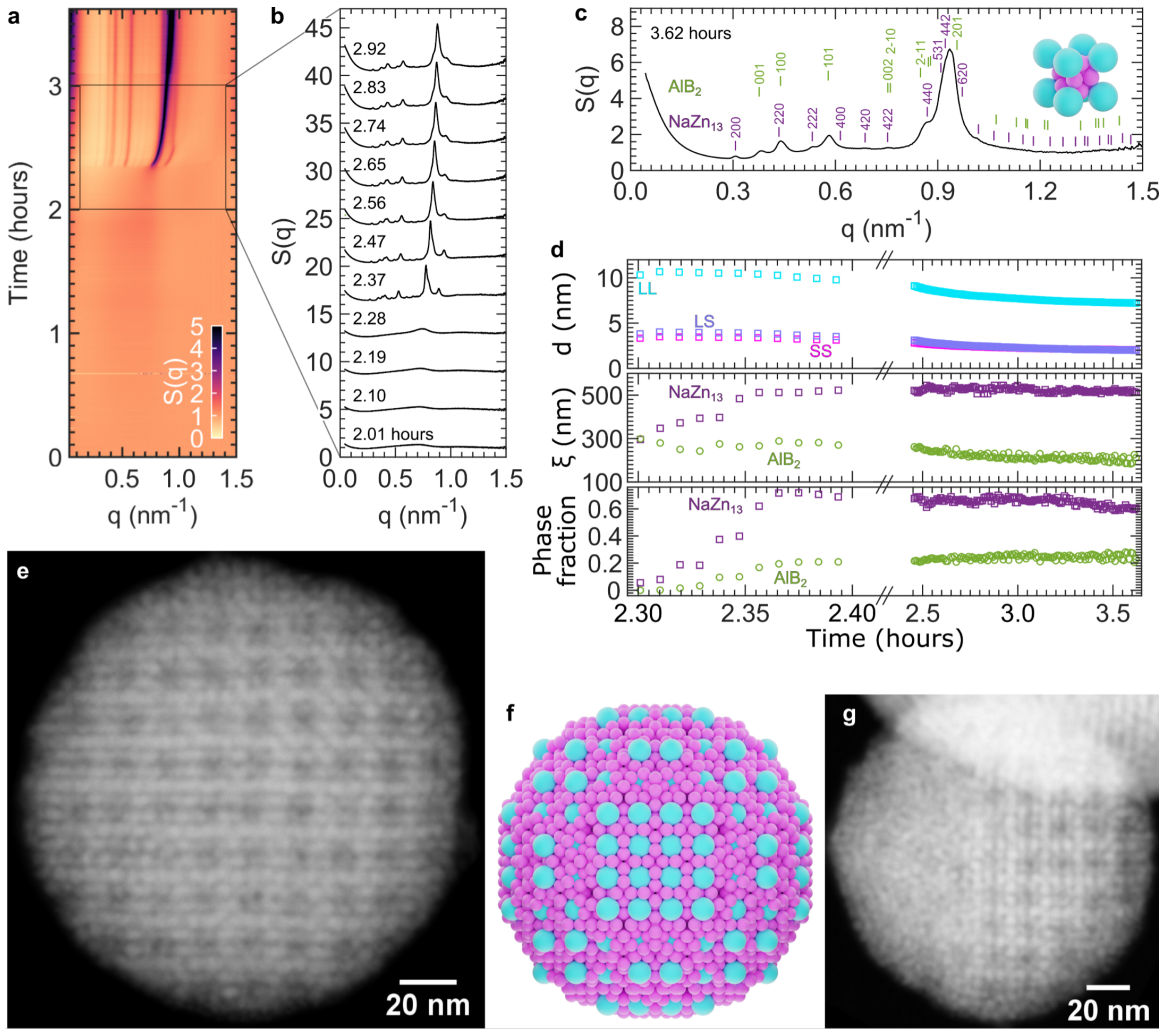

Figure 6.2: Formation of colloidal $NaZn_{13}$ BNSLs. (a) Kinetic structure factor, $S(q)$, of a binary dispersion of PbS and FICO NCs under spherical confinement of a drying emulsion. (b) $S(q)$ patterns showing the emergence and evolution of diffraction peaks around the time of BNSL nucleation. (c) Final $S(q)$ pattern identifying the BNSL structure as $NaZn_{13}$ with a minority AlB_2 phase. (d) Evolution of the surface-to-surface distance between larger (L) and smaller (S) NCs, d (top), average crystal size, ξ (middle), and phase fraction (bottom) of the two binary phases during lattice compression. (e) Dark-field STEM micrographs of a single-crystal $NaZn_{13}$ BNSL, and (f) its structural model. (g) Micrograph of a hetero-structure showing the coexistence of $NaZn_{13}$ with a secondary phase.

careful examination of the final diffraction pattern indicates the coexistence of a majority phase isostructural to $NaZn_{13}$ with a minority AlB_2 phase, as shown in Figure 6.2c. The $NaZn_{13}$ structure consists of a body-centered icosahedral cluster of 13 smaller particles contained within a simple cubic subcell of the larger particles, as illustrated in the inset in Figure 6.2c.

We study the synchronous evolution of the $NaZn_{13}$ and AlB_2 phases in Figure 6.2d. The lattice parameters of the two crystalline phases slowly decrease as a function of time, to reach maximum inorganic volume fractions of $\phi = 0.360$ and 0.384 for $NaZn_{13}$ and AlB_2 , respectively. Within 0.1 hours after nucleation, the average domain sizes of the $NaZn_{13}$ and AlB_2 phases rapidly increase and saturate at their final values of $\xi \approx$ 510 nm and 200 nm, respectively. We quantify the fraction of each crystalline phase by comparing with the assembly performed at a NC number ratio of 1:2. After nucleation, the fraction of both $NaZn_{13}$ and AlB_2 phases quickly increases to reach the values of 0.74 and 0.21, respectively, confirming $NaZn_{13}$ as the majority phase. Interestingly, while the fraction of the AlB_2 phase shows a slow increase in the late stages of the assembly, that of the $NaZn_{13}$ phase shows a comparable decrease. This suggests that even though the $NaZn_{13}$ phase readily nucleates to occupy most of the available volume, this structure might be thermodynamically less stable than AlB_2 . The relative strengths of inter-NC interactions may be responsible for shifting this equilibrium towards one specific phase.

Ex situ dark-field STEM confirms the formation of 3D colloidal $NaZn_{13}$ BNSLs; see Figure 6.2e. The [200] projection clearly illustrates the cubic symmetry of the $NaZn_{13}$ phase, as well as the four-fold symmetry of the smaller NCs surrounding each larger NC. In Figure 6.2f we illustrate a 3D model of this colloidal BNSL, obtained by carving a sphere out of a $NaZn_{13}$ lattice with experimentally determined structural parameters. We also observed superstructures characterized by a heterostructure of $NaZn_{13}$ with a second phase, shown in Figure 6.2g, confirming the presence of a minority phase as suggested by SAXS.

In situ measurements draw a detailed picture of the self-assembly process that we juxtapose with simulations to reveal the driving force behind the formation of BNSLs. The formation of AlB_2 and $NaZn_{13}$ BNSLs is frequently attributed to entropy[96, 193] because of their high packing fractions[76, 194] and because these are both equilibrium phases of the hard-sphere model[87], whose phase behavior is solely dictated by entropy. However, in Chapter V of this thesis we discovered that the self-assembly of the AlB_2 phase is kinetically prohibited in hard-sphere mixtures at a NC number ratio of 1:2, indicating that more complex interactions are necessary for its formation.

The NCs used in this work interact through van der Waals interactions between inorganic cores and between ligands, mediated by the choice of solvent, and superparamagnetic interactions in the case of Fe3O4 NCs[195]. Previous efforts have focused on computing the potential of mean force between two NCs, leading to results that are limited to specific compositions[196, 197, 198, 199, 82, 200]. Furthermore, many of these results pertain to NCs in vacuum, while the superlattice contraction observed in our experiments indicates that the ligand coronas are still swollen with solvent at the time of self-assembly. These considerations warrant the use of a more general approach. Here, we infer the overall interaction potential by directly comparing the experimentally determined self-assembly results with simulation. The inability of AlB_2 to form from purely-repulsive NCs at a number ratio of 1:2 implies the key role of attractive interactions. The introduction of an isotropic, attractive force is consistent with the expected van der Waals and superparamagnetic interactions and may promote self-assembly behavior consistent with experiments. Such interaction is well-described by a Mie potential[201],which is characterized by a repulsive core and an attractive well whose depth and width control the strength and range of attraction, respectively. Similar NC interaction potentials have been found in previous studies[196, 197, 198, 199, 82, 200]. Here, we pinpoint the specific shape of the potential driving the formation of BNSLs. We test two different well widths, described as "narrow well" and "wide well" and shown in Figure 6.3a-b, scaling

the range of the interaction between two NCs by the average of their effective sizes to account for the size difference. For simplicity, the well depth, ε, is kept constant for all interspecies interactions, *i.e.* $\varepsilon = \varepsilon_{LL} = \varepsilon_{LS} = \varepsilon_{SS}$. To reveal how the range and strength of interaction affect the phase behavior, we computed phase diagrams for a NC number ratio of 1:2, as shown in Figure 6.3c-d. In the presence of the narrow well, the gas and solid AlB_2 phases are both stable. In contrast, in the presence of the wide well a region of vapor-liquid coexistence is stable above a critical well-depth ε_c; see Figures 6.3d and 6.5. This is consistent with the Noro-Frenkel law of corresponding states[202], which predicts that wider potential wells exhibit a stable liquid–gas transition.

While these phase diagrams show the equilibrium predictions for a given set of parameters, they do not indicate whether a phase is kinetically accessible. To study whether the AlB_2 phase will form, we slowly compress an initially disordered fluid under periodic boundary conditions. A combination of Steinhardt order parameters[68] enables the quantification of the fraction of larger NCs that become crystalline as a function of time, N_{AlB_2}/N_{Total}; see Figure 6.6 for calculation details. When using a narrow well at least as deep as 1.0 kT, over 50% of larger NCs crystallize by the end of the simulations, as shown in Figure 6.3e. There is limited crystallization for a shallower well of 0.5 kT, and no crystallization when the NCs are purely repulsive. In contrast, only minimal crystallization occurs with the wide well, with at most 6% of larger NCs registering as crystalline even for the deepest well investigated, 2.5 kT, as shown in Figure 6.3f.

These results show that short-range attractive forces substantially improve the crystallization kinetics of NCs into AlB_2. The rate at which AlB_2 nucleates and grows is related to both the degree of supersaturation of NCs and their mobility. Since the NC mobility depends strongly on density, self-assembly occurs more readily when higher supersaturations are reached at lower densities, which is the case for the narrow, deep well. In contrast, the dense liquid phase found for the wide, deep well reduces the degree of supersaturation for AlB_2 and thus hinders self-assembly. We quantify these effects by

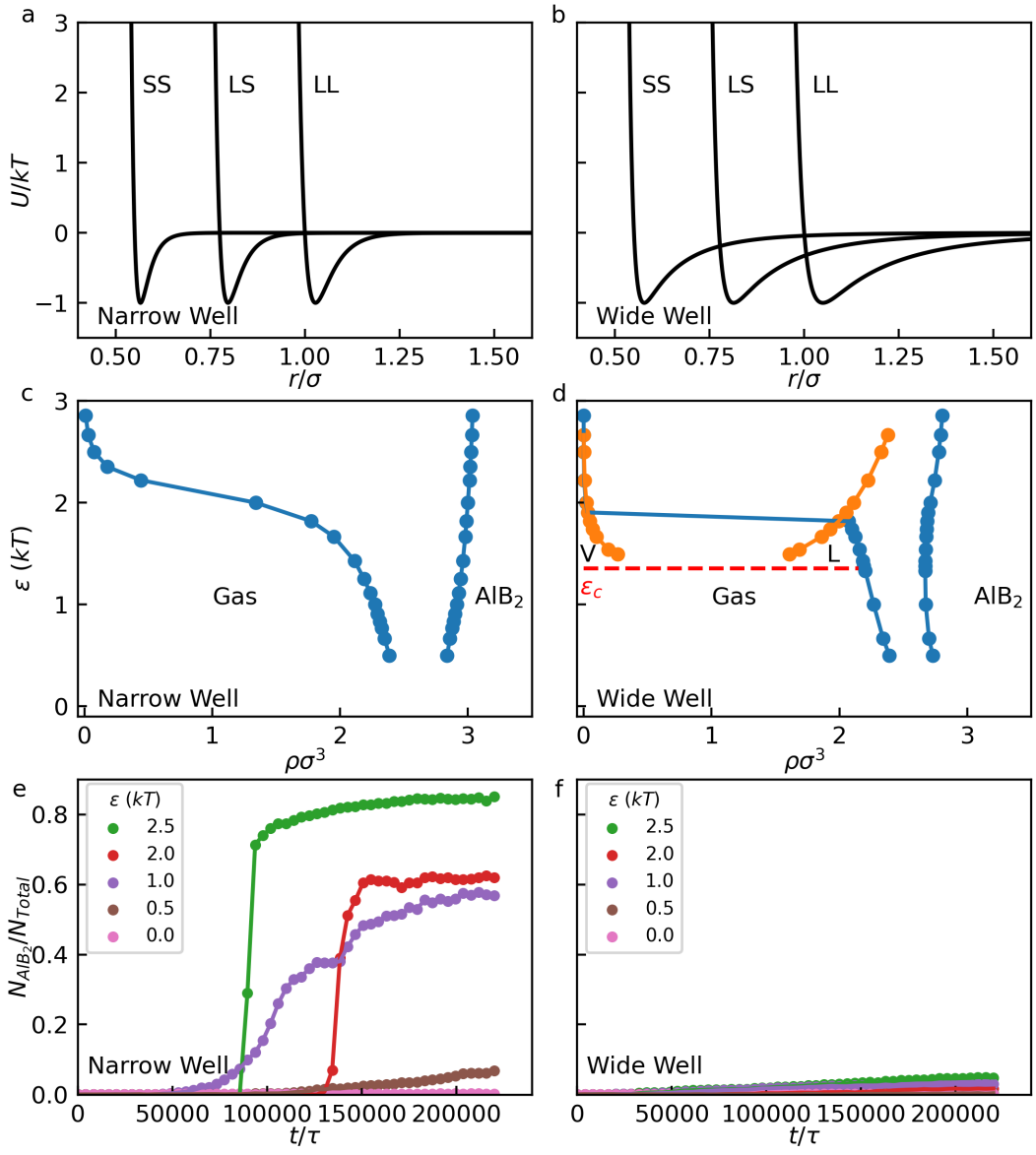

Figure 6.3: The influence of attractive forces in binary mixtures. (a-b) Mie pair potentials shown as a function of the normalized interparticle distance, $U(r/\sigma)$, calculated for a well depth of 1 kT and for length scale parameters $m = 25$ (a) and $m = 6$ (b). The potential in (a) is described as the "narrow well" and the one in (b) as the "wide well" in the main text. For each potential, three types of interactions are shown: between larger NCs (LL), between larger and smaller NC s (LS), and between two smaller NCs (SS). (c-d) Thermodynamic phase diagrams computed from free energy calculations for the narrow (c) and wide well (d) as a function of well depth, ε, and normalized particle density, $\rho\sigma^3$. The blue and orange lines demarcate the regions of gas-solid coexistence and vapor-liquid coexistence, respectively. Errors in the phase boundaries are smaller than the points. The dashed red line in (d) indicates the critical well depth ε_c above which vapor-liquid coexistence occurs. The phase diagrams are computed at a NC number ratio of 1:2. (e-f) The evolution of the number of AlB_2-like particles in self-assembly simulations through slow compression for the narrow (e) and wide well (f).

showing a measure of the degree of supersaturation, the difference in chemical potentials between the crystal and fluid phases, as a function of NC mobility in Figure 6.7. The acceleration of crystal nucleation with isotropic, short-ranged attractive forces was reported previously in single-component systems[203, 204, 205], and attributed to either critical fluctuations[203], or the presence of a metastable liquid phase[204, 205]. These factors are not relevant for our systems as the narrow well is simulated away from its metastable critical point, as shown in Figure 6.8. Instead, our results are reminiscent of the increased driving force for crystallization observed in colloids with small attractive patches[206].

These results indicate that the interaction between NCs during self-assembly is consistent with a pair potential characterized by a narrow, deep well. After settling on a specific potential shape, we check for further consistency with experiment by simulating conditions closer to experiment by adding NC polydispersity and spherical confinement to the simulations. We determine the polydispersity of each NC species by SAXS and simulate each NC's interaction with the confining boundary of the droplet using a Weeks-Chandler-Anderson potential[207]. Each simulation system is initialized as a colloidal fluid in a droplet, then slowly compressed to induce self-assembly. In close agreement with experiment, AlB_2 forms at a NC number ratio of 1:2, while $NaZn_{13}$ forms at 1:13. Interestingly, crystallization begins at a slightly lower volume fraction for $NaZn_{13}$ than AlB_2, 0.528 and 0.572 respectively, as shown in Figure 6.4a. Simulations performed at lower volume fractions did not result in self-assembly. As shown by the kinetic change in the fraction of crystalline particles, rapid crystal growth follows nucleation. Consistent with experiments, we find no intermediate crystal phases that precede the final phases[178, 179].

Simulations provide the unparalleled advantage of directly visualizing crystal nucleation, a process notoriously elusive to capture in experiments. The early stages of assembly for $NaZn_{13}$ and AlB_2 BNSLs are shown in Figures 6.4b-c, respectively. To highlight

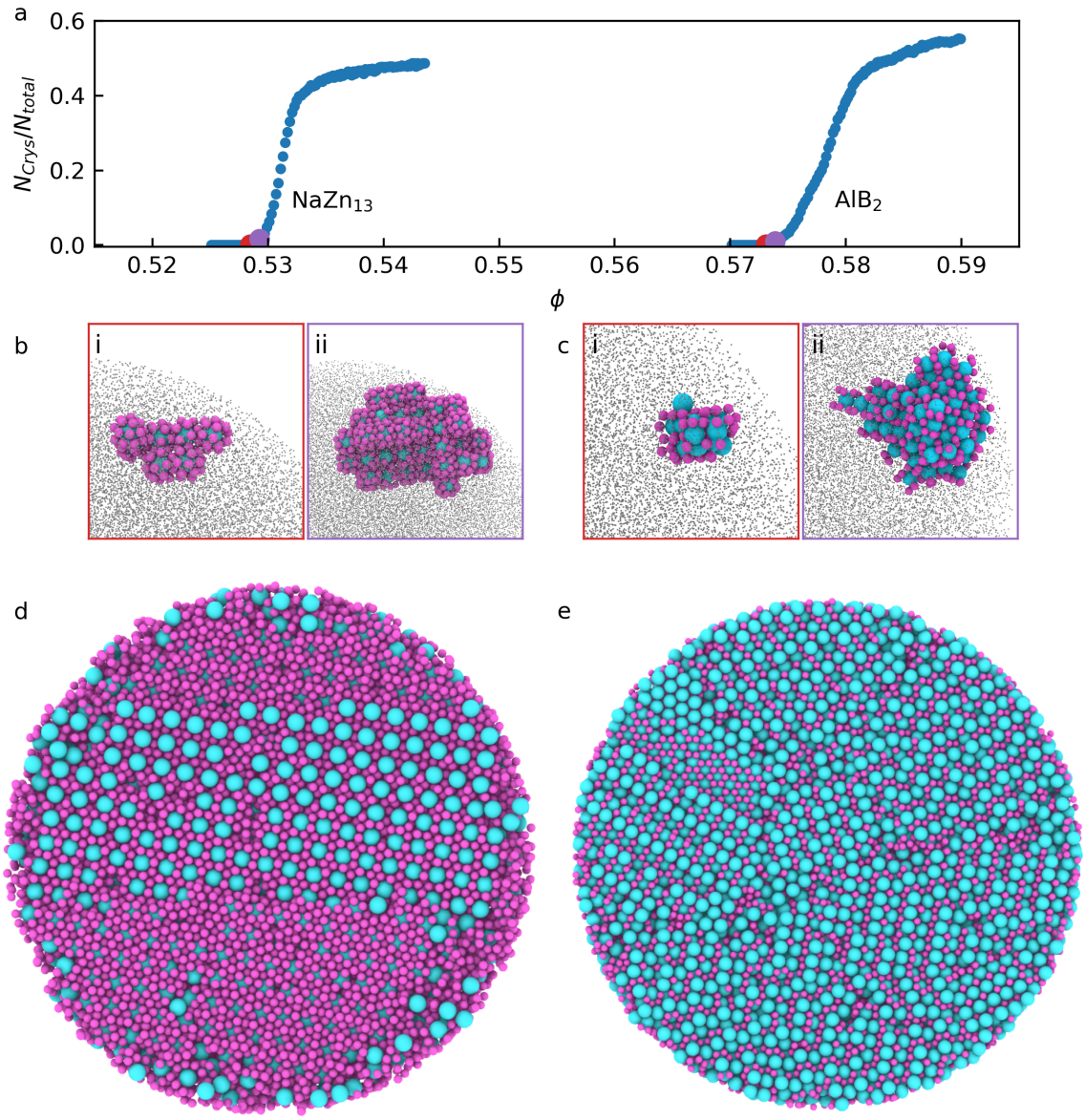

Figure 6.4: The self-assembly of AlB_2 and $NaZn_{13}$ in spherical droplets. In (a) we show the results of attempts to self-assemble AlB_2 and $NaZn_{13}$ with the deepest (2.5 kT), narrow well used in Figure 6.3. The curve labelled "$NaZn_{13}$" was obtained at a stoichiometry of 1:13, while the curve labelled "AlB_2" was obtained at a stoichiometry of 1:2; N_{crys}/N_{total} is the fraction of large particles we identify as $NaZn_{13}$-like or AlB_2-like respectively. In (b) and (c) we show early stages of the growing $NaZn_{13}$ and AlB_2 crystals, respectively. We show two different time points, (i) and (ii); the color of the images' borders match that of the corresponding timepoints in (a) from which they were taken. We show large particles identified as crystalline in blue and small particles neighboring a crystalline large particle in pink; all other particles are reduced in size and colored grey. In (d) and (e), we visualize an inner slice of each droplet at the final time point of our simulations, coloring every particle. Unlike the simulations in Figure 6.2, each species is set to have the polydispersity of the corresponding experimental nanoparticles.

the crystalline nuclei, we color only the NCs identified as being in a crystalline environment, while fluid-like NCs are shown as smaller grey spheres. For both $NaZn_{13}$ and AlB_2 BNSLs, the critical nuclei emerge from the fluid multiple particle diameters away from the surface of the droplet, allowing us to conclude that these BNSLs undergo homogeneous nucleation. Only after nucleation do the crystallites of $NaZn_{13}$ and AlB_2 BNSL spread to the wall. This behavior is unaffected by the size of the droplet, as shown by replacing the spherical walls with flat walls to simulate significantly larger droplets, as shown in Figure 6.9. We find no evidence for exotic pre-nucleation clusters. The final stages of growth result in the crystals shown in Figures 6.4d-e. The $NaZn_{13}$ grains are easily identifiable by the simple cubic arrangement of the larger NCs. A single crystal grain spans most of the spherical superstructure, consistent with the experimental results shown in Figure 6.2. In contrast, multiple grains of AlB_2 are present. This qualitatively agrees with the SAXS measurements showing smaller grains for AlB_2 than $NaZn_{13}$, although specific crystal grains are harder to visualize in the TEM micrographs, making a quantitative comparison between simulation and experiment challenging.

An apparent discrepancy remains between experiment and simulation: experimental results indicate the presence of 20% AlB_2 as a second phase for samples prepared at a NC number ratio of 1:13, while simulations show less than 1% AlB_2. Interestingly, reducing the magnitude of the attraction between smaller NCs results in the coexistence of AlB_2 and $NaZn_{13}$ at a NC number ratio of 1:13, removing the discrepancy as shown in Figure 6.10. This adjustment is consistent with the dependence of van der Waals and superparamagnetic interactions on NC size[195].

6.3 Conclusions

We demonstrate a remarkable correspondence between experiment and simulation of the self-assembly of BNSLs. Under spherical confinement, NCs readily nucleate into binary phases isostructural to AlB_2 and $NaZn_{13}$ without intermediate liquid or crystal

phases. The burst of crystal nucleation is followed by a gradual lattice contraction to result in multifunctional, 3D, dense, crystalline binary phases. We can accurately reproduce these experimental results in simulation by introducing a short-ranged, attractive potential, which we find kinetically promotes self-assembly. This direct link between experiments and simulations reveals that BNSLs nucleate homogeneously and directly, without intermediate solid phases preceding the final crystal. In achieving a closer correspondence between experiment and simulation, and demonstrating the importance of short-range attraction for assembly kinetics, this work represents a crucial first step in a priori prediction of BNSLs towards the deterministic hetero-integration of NCs into multifunctional structures, targeting applications in photonics, excitonics, phononics, and catalysis.

6.4 Methods

Note that we have ommited details on the experiments from this chapter.

We used molecular dynamics (MD) with the HOOMD-Blue simulation toolkit[148] to simulate a binary mixture of NCs with interactions modeled by the Mie (IPL) potential:

$$U_{ij} = \varepsilon_{ij}\left(\frac{n}{n-m}\right)\left(\frac{n}{m}\right)^{m/n-m}\left(\left(\frac{\sigma_{ij}}{r_{ij}}\right)^{n} - \left(\frac{\sigma_{ij}}{r_{ij}}\right)^{m}\right) \tag{6.1}$$

is the energy between two NCs (particles) i and j separated by a distance r_{ij}. The potential is described by four parameters: a measure of the particle's size, σ_{ij}; the power of the repulsive component, n; the magnitude of the interaction, $varepsilon_{ij}$; and the length scale of the attractive interaction, m. We set σ_{ij} to match the effective size ratio of the NCs used in experiment: $\sigma_{SS} = 0.55\sigma_{LL}$, $\sigma_{LS} = (1 + 0.55)\sigma_{LL}/2$, and $\sigma_{LL} = 1$, where L represents the larger NCs and S the smaller NCs. For simplicity, we set the depth of the potential well to be equal for all particle pairs: $\varepsilon = \varepsilon_{LL} = \varepsilon_{LS} = \varepsilon_{SS}$. We also use σ to represent σ_{LL} in the text. For consistency with Chapter V, we set the power n to a value of 50. We analyze systems with m of 6 and 25, which we refer to as "wide well"

Table 6.1: Density Range for Compression Simulations

m	ε/kT	Densities ($\rho\sigma^3$)
25	0.0	2.60-2.70
25	0.5	2.60-2.70
25	1.0	2.52-2.62
25	2.0	2.37-2.47
25	2.5	2.18-2.28
6	0.0	2.60-2.70
6	0.5	2.61-2.71
6	1.0	2.54-2.64
6	2.0	2.44-2.54
6	2.5	2.41-2.51

and "narrow well" respectively. The resulting potentials are shown in Figure 6.3a-b for a well-depth of 1.0 kT . Throughout the paper we manipulate the well depth by changing the temperature, which is inversely proportional to the well depth. We define the units of time as $\tau = \sigma(w/\varepsilon)^{(1/2)}$, where w is mass and set to 1 for every type of particle.

To compute the free energies of different phases in Figure 6.3c-d, we combined thermodynamic integration with the Einstein molecule method[71], a variant of the Frenkel-Ladd method[70], using at least 2,000 particles in every case. The free energies of the gas and liquid phases were computed at a stoichiometry of 1:2. Self-assembly was attempted with 27,000 particles by slowly compressing the particles from an initially disordered fluid state to a crystalline or kinetically arrested amorphous state. In Table 6.1 we give the range of densities compressed over for each well depth and width. The densities were chosen because of their proximity to where crystallization or kinetic occurs. We also compute the diffusion coefficients in the vicinity of kinetic arrest; see Figure reffig:diffusion. We used NVT simulations based on the MTK equations[155] to thermostat our simulations in Figure 6.3e-f and NVT simulations using a Langevin integrator[156] to thermostat our simulations in Figure 6.4.

For the simulations in Figure 6.4, we treat the distribution of particle sizes as a mixture of two normal distributions: one centered at a size of $1\sigma_{LL}$ and one centered at a size of $0.55\sigma_{LL}$. The standard deviations (s) of the normal distributions were chosen to match experiment: s = $0.047\sigma_{LL}$ for that of the larger particles and s = $0.063\sigma_{SS}$ for that of

the smaller particles. We then discretized the distributions, with 13 bins associated with each peak. We placed the particles inside a spherical droplet, whose edges repel the particles with a Weeks-Chandler-Anderson potential. We computed an effective packing fraction by calculating an effective particle size according to the prescription of Barker and Henderson[208]. We scaled the wall's range of interaction by $\sigma_i/2$, which accounts for the different sizes of the particles. We used Steinhardt order parameters[68] in Figures 6.3 and 6.4 to identify crystalline particles. The specific combinations for each crystal are shown in Figure 6.6. The parameters were calculated using the *freud* software library[69]. We used Ovito to visualize our simulations throughout this work[72]. The computational workflow and data management for this publication was primarily supported by the *signac* data management framework[73].

6.5 Supplement

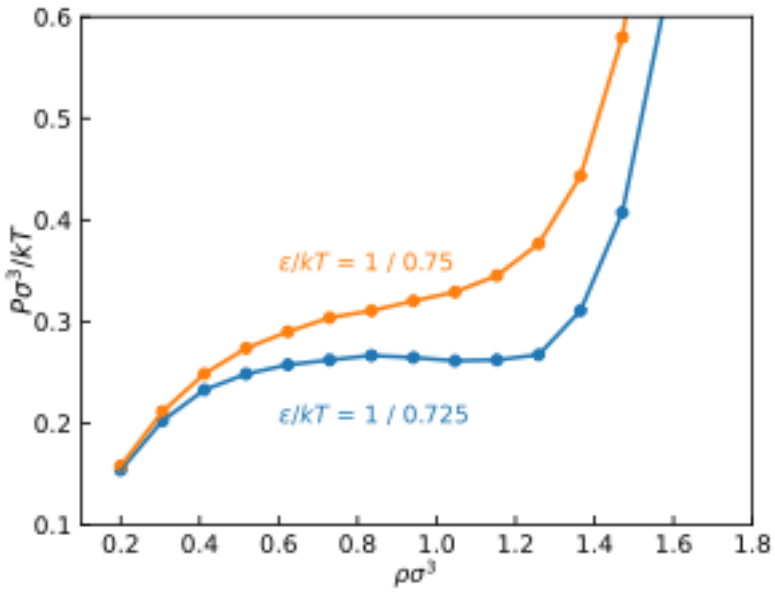

Figure 6.5: Our estimation of the critical point using pressure-volume data. The downward slope between a few points at $\varepsilon/kT = 1/0.725$ indicates that vapor-liquid separation occurs while the lack of a downward slope for $\varepsilon/kT = 1/0.75$ indicates the lack of phase separation. We thus estimated the critical point to be $\varepsilon/kT = 1/0.738$. Note that this estimate is not used in any of our free energy calculations, and thus the estimate's uncertainty does not propagate into those calculations. We collected the pressure-volume data by simulating 8,000 particles for $16{,}000\tau$ at a stoichiometry of 1:2.

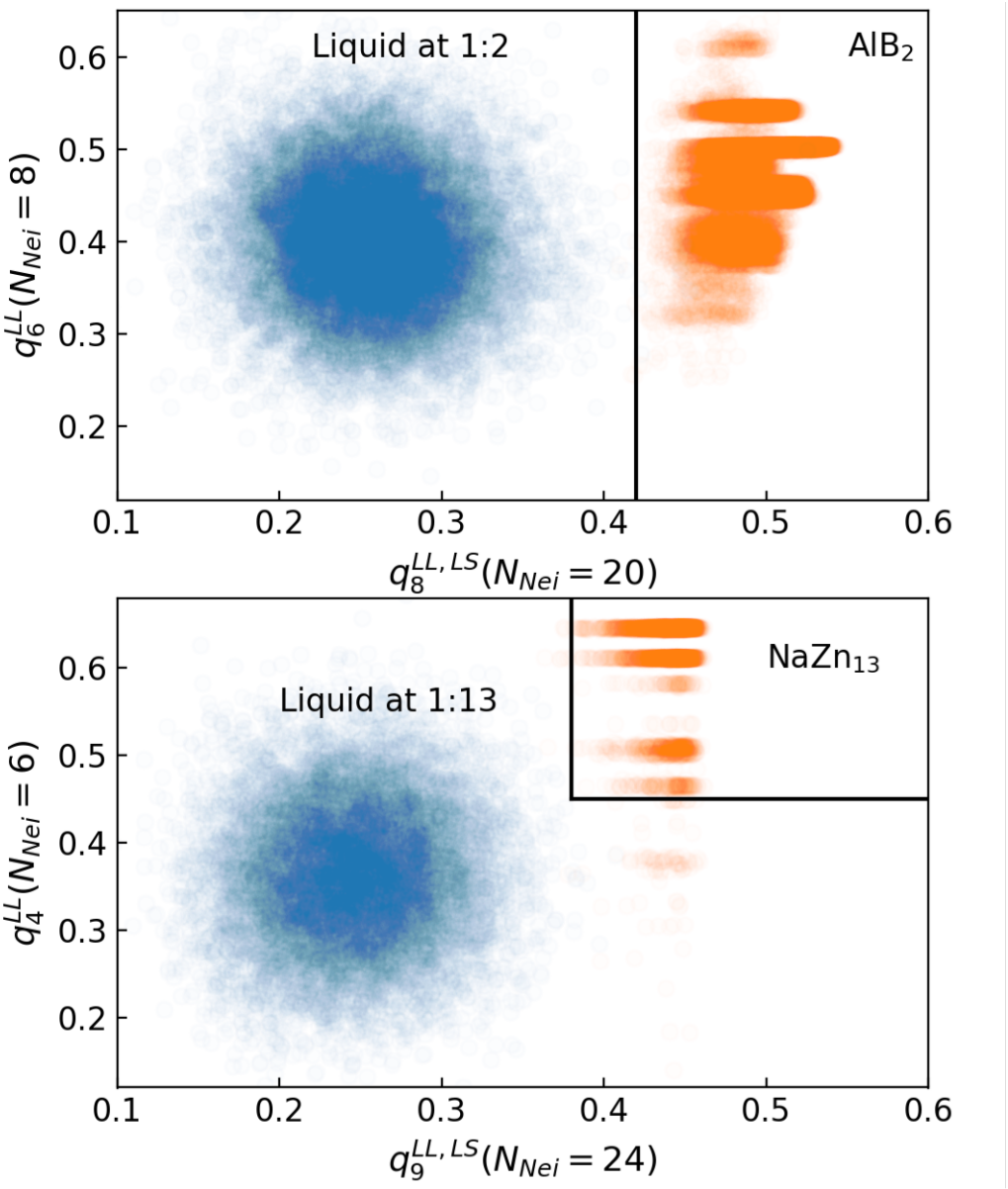

Figure 6.6: The order parameters we used to distinguish between liquid and solid particles. Large particles in the AlB_2 phase can be distinguished using the q_8 using the closest 20 particles (large or small). We also computed the q_6 of the nearest 8 large particles but do not use it identify particles as being in the AlB_2 phase. Large particles in the $NaZn_{13}$ phase can be distinguished using the q_4 using the closest 6 large particles and the q_9 of the closest 24 particles (large or small). The number of neighbors was chosen to match that of particles in the perfect crystal. The results for the liquid phase were taken from the first few frames of our self-assembly simulations shown in Figure 6.4. The results for the solid phases were gathered at $P\sigma^3/\varepsilon = 1$. To account for the fact that our self-assembly results tend to have many defects, we removed about 10% of the particles from each simulation frame of the solid phases before computing the order parameters. The specific bound used to distinguish AlB_2 is $q_8^{LL,LS} > 0.42$. The specific bounds used to distinguish $NaZn_{13}$ are $q_9^{LL,LS} > 0.38$ and $q_6^{LL} > 0.45$.

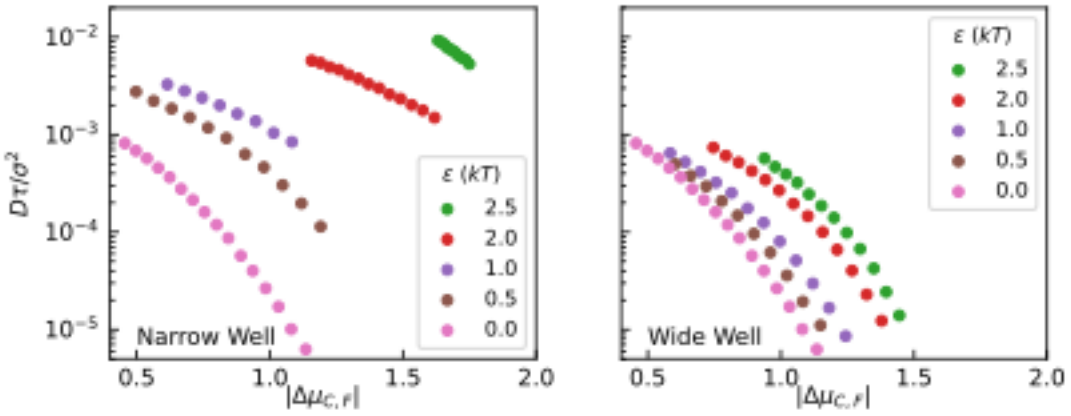

Figure 6.7: The diffusion constant versus the chemical potential driving forces for every pair potential we attempted self-assembly with in Figure 6.3. The chemical potential driving forces are computed as $|\Delta\mu_{C,F}| = |\mu_{AlB_2} - \mu_L/3 - (2/3)\mu_S|$, where μ is computed in the same manner used to generate the phase diagrams in Figure 6.3. Nucleation should be most favorable if a high $|\Delta\mu_{C,F}|$ can be achieved with highly mobile particles, which corresponds to the upper right corner of the graphs. We see a trend towards that corner with increasing well depth, with the trend being much stronger for the narrow well system.

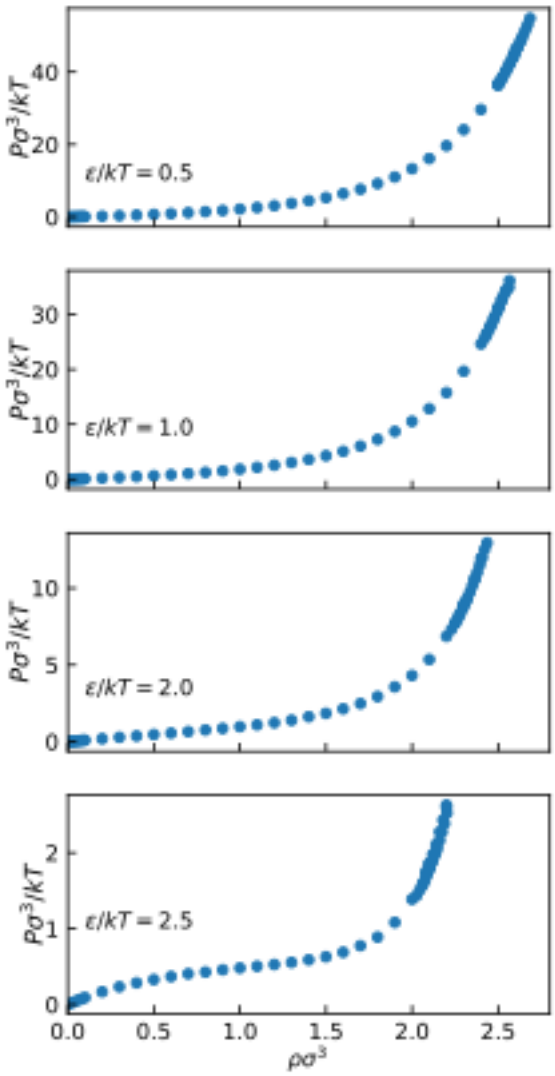

Figure 6.8: Pressure-volume data for the narrow well at the 4 different well depths examined in the text. We do not see a critical point for any well-depth, although the trend in the data indicates that it may form for well-depths only slightly larger 2.5 kT . However, every system self-assembles in our simulations at a number density higher than $2/\sigma^3$ which is much higher than the likely critical density.

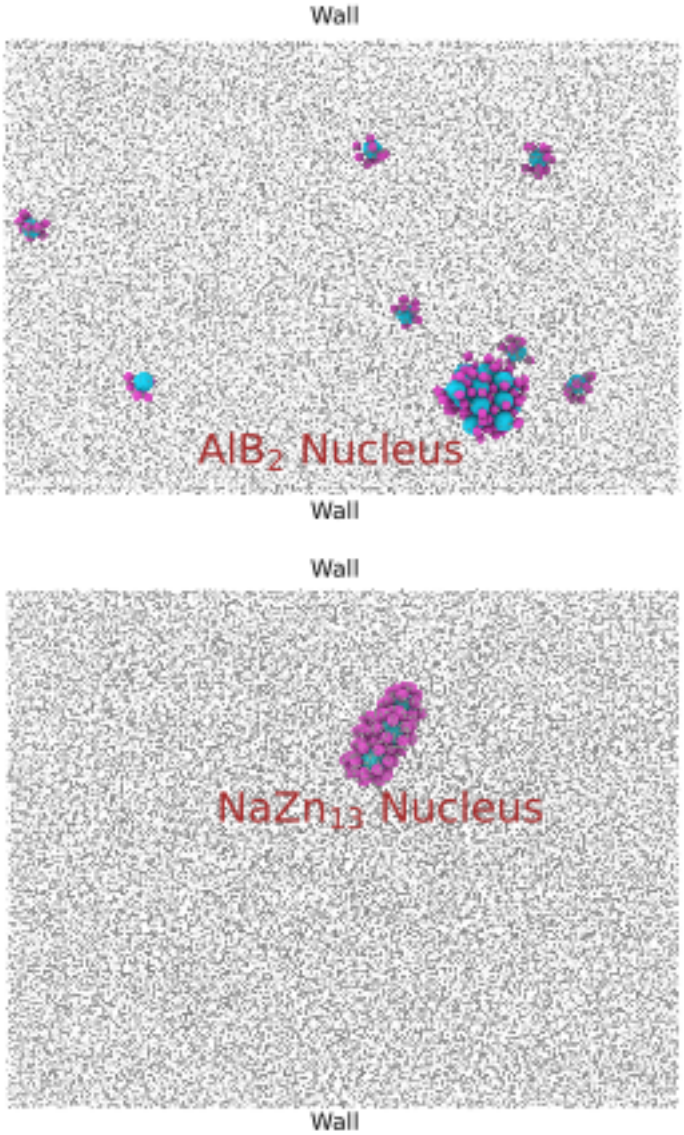

Figure 6.9: BNSL formation with flat walls. We show any large NC identified as crystalline as blue and any small particle neighboring a crystalline large NC as pink; all other NCs are reduced in size and colored grey. The simulations were run under conditions close to those shown in Figure 6.4. The AlB_2 nucleus forms at a stoichiometry of 1:2, while the $NaZn_{13}$ nucleus forms at a stoichiometry of 1:13. In no case does the nucleation begin on the wall.

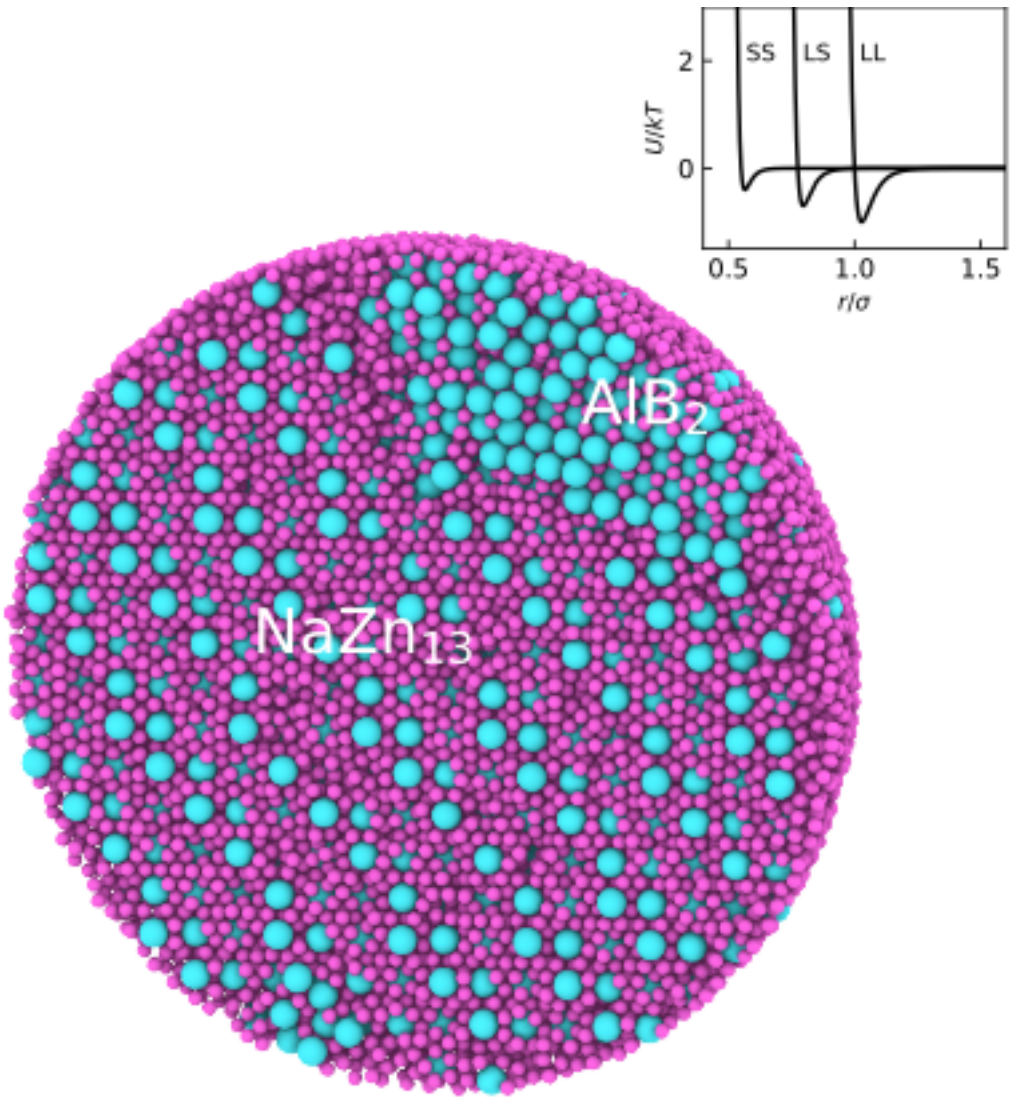

Figure 6.10: Crystal formation with unequal attractive wells. As shown in the plot, the well-depth is 2.5 kT between large particles, 1.75 kT between large and small particles, and 1 kT between small particles. With this pair potential we obtain a small region of AlB_2 alongside a larger region of $NaZn_{13}$ at a stoichiometry of 1:13. We did not use polydisperse particles for this simulation because polydispersity slows equilibration.

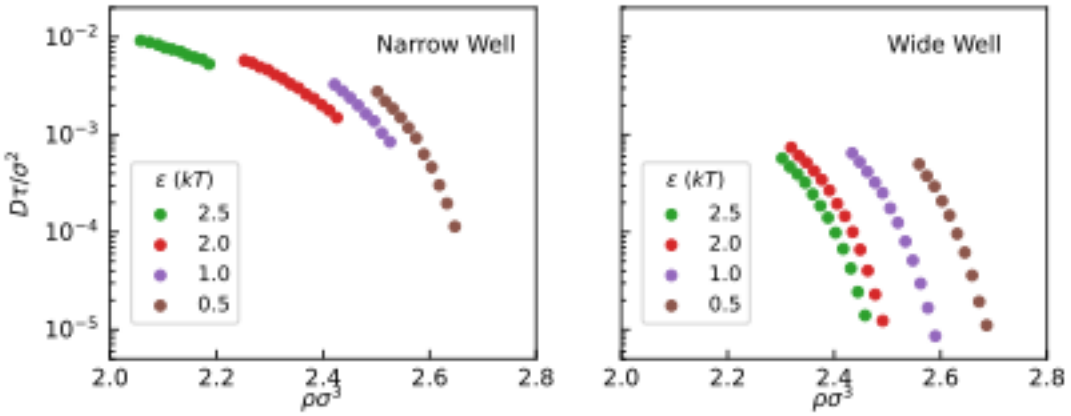

Figure 6.11: The diffusion constants (D) of the large particles as a function of density for different well-depths and well-widths. We computed D from simulations of 27,000 particles at a NC number ratio of 1:2. We could collect data up until crystallization began to occur; thus, we could go to higher densities, and lower diffusion coefficients, for the wide well. Note that we varied well depth by changing the temperature instead of explicitly ε . We expect that changing ε instead would change the diffusion coefficients by less than an order of magnitude.

CHAPTER VII

Guide to Binary Colloidal Self-Assembly with Non-Specific Interactions

7.1 Introduction

Self-assembly is powerful way to prepare binary colloidal crystals.[16, 18, 22, 121, 56, 75, 209] Because the structure of the superlattice can dictate its properties[29, 15, 30, 31, 32, 33, 36], a common goal is to design colloidal particles such that they self-assemble into a desired structures. Doing so requires understanding how the interparticle interactions and system parameters influence self-assembly.

Many previous efforts involve designing "specific" interactions between the colloidal particles such that they bond in a desired manner. These include particles with attractive patches that promote a desired bonding valence[45, 53, 206, 210, 211, 212] and particles which prefer to bond with a specific species of particle[20, 39, 121, 213, 48]. With specifically interacting particles, the structure that self-assembles can frequently be predicted by considering the energetic favorability of different candidate structures[121].

It is more difficult to predict the self-assembly behavior of nonspecifically interacting particles, which include bidisperse mixtures of hard spheres or mixtures of mutually attractive spheres. Nonetheless, many colloids which self-assemble can be classified as interacting non-specifically or near non-specifically[18, 22, 104, 74, 32, 26]. A particularly common idea is that the densest packing structure will self-assemble because at densities below the densest packing the structure will provide the most free volume and therefore maximize the entropy[76]. However, while most crystal phases reported to self-

assemble for nonspecifically interacting particles are very dense (compared to those that self-assemble for patchy particles[206]), phases besides the densest packing are frequently reported to self-assemble[18, 22, 104, 74, 32, 26].

Here we use simulations to map out the self-assembly behavior of bidisperse, non-specifically interacting particles. We examine both hard sphere-like and attractive particles, characterizing their self-assembly as a function of stoichiometry and size ratio. Surprisingly, we find that hard sphere-like and attractive particles self-assemble similar phases, but at different size ratios and stoichiometries. We also find that both sets of particles can self-assemble into a quasicrystal phase, providing further evidence that quasicrystal formation does not require complicated interactions. Our work will function as a guide for those working with these particles.

7.2 Self-Assembly Results

To mimic hard spheres we use the Weeks-Chandler-Anderson (WCA) potential[207] at a low temperature, as shown in Figure 7.1a. The WCA potential is a Lennard-Jones potential truncated and shifted at its minimum to eliminate the attractive interactions:

$$U_{ij} = \begin{cases} 4\epsilon\left(\left(\frac{\sigma_{ij}}{r_{ij}}\right)^{12} - \left(\frac{\sigma_{ij}}{r_{ij}}\right)^{6}\right) + 1 & r_{ij} < 2^{1/6}\sigma_{ij} \\ 0 & r_{ij} > 2^{1/6}\sigma_{ij} \end{cases} \tag{7.1}$$

where U_{ij} is the potential energy between two particles i and j, σ_{ij} represents their diameter, r_{ij} is interparticle distance, and ϵ is the unit of energy. We simulate it at a temperature of 1/200 kT; at that temperature previous reports[110] indicate that it nucleates similarly to hard spheres. For reference, if we evaluate $d(U/kT)/dr$ (a measure of softness) at the interparticle distance corresponding to $U/kT = 1$, we find it maps to an inverse power law potential with an exponent of 164.

We use the Mie potential[201] with a short-ranged attractive well to simulate attractive particles:

$$U_{ij} = 2^{3/2}\epsilon\left(\left(\frac{\sigma_{ij}}{r_{ij}}\right)^{50} - \left(\frac{\sigma_{ij}}{r_{ij}}\right)^{25}\right). \tag{7.2}$$

In Chapter VI we found that narrow attractive wells can self-assemble on much shorter time scales than with wider wells or hard sphere-like particles.

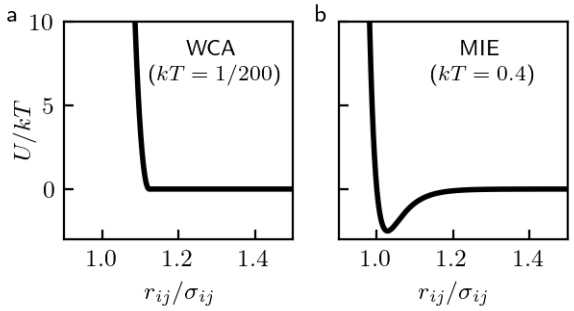

Figure 7.1: The potentials used here. The hard sphere-like WCA potential at $kT = 1/200$ is shown in a), and the attractive Mie potential is $0.4kT$ is shown in b). We always simulated WCA particles at $1/200$ kT, but with Mie particle we slowly dropped the temperature from 0.41 to 0.31 kT.

We used the HOOMD-blue simulation toolkit[148] to conduct molecular dynamics simulation in this work. With WCA particles, we slowly compressed the system in NVT simulations to induce self-assembly. With Mie particles, we slowly dropped the temperature in NPT simulations at low pressure (0.1 ϵ/σ^3) to induce self-assembly. The temperature range examined was $0.41 > kT/\epsilon > 0.31$. This alternative scheme was designed to increase the strength of attraction (which is inversely proportion to kT) at the time of self-assembly. Our simulations had 216,000 particles.

Our results for the self-assembly of the WCA and Mie systems are shown in Figures 7.2a and 7.2b, respectively. We used Steinhardt order parameters[68] to identify if a particle's local environment resembled that of a crystal. If we observed 10 particles with the same local environment within a cluster, we indicate that crystal with a marker in Figure 7.2. We examined a range of stoichiometries between 1:1 and 1:19 (particle number ratio of large to small). We did not look at cases where the large particles outnumber the small particles because the large particles usually self-assemble into single-component crystals in such cases. We suspected more phases might be present for the WCA spheres below a size ratio of 0.54, so we examined those size ratios with a higher resolution. Our suspicion was incorrect.

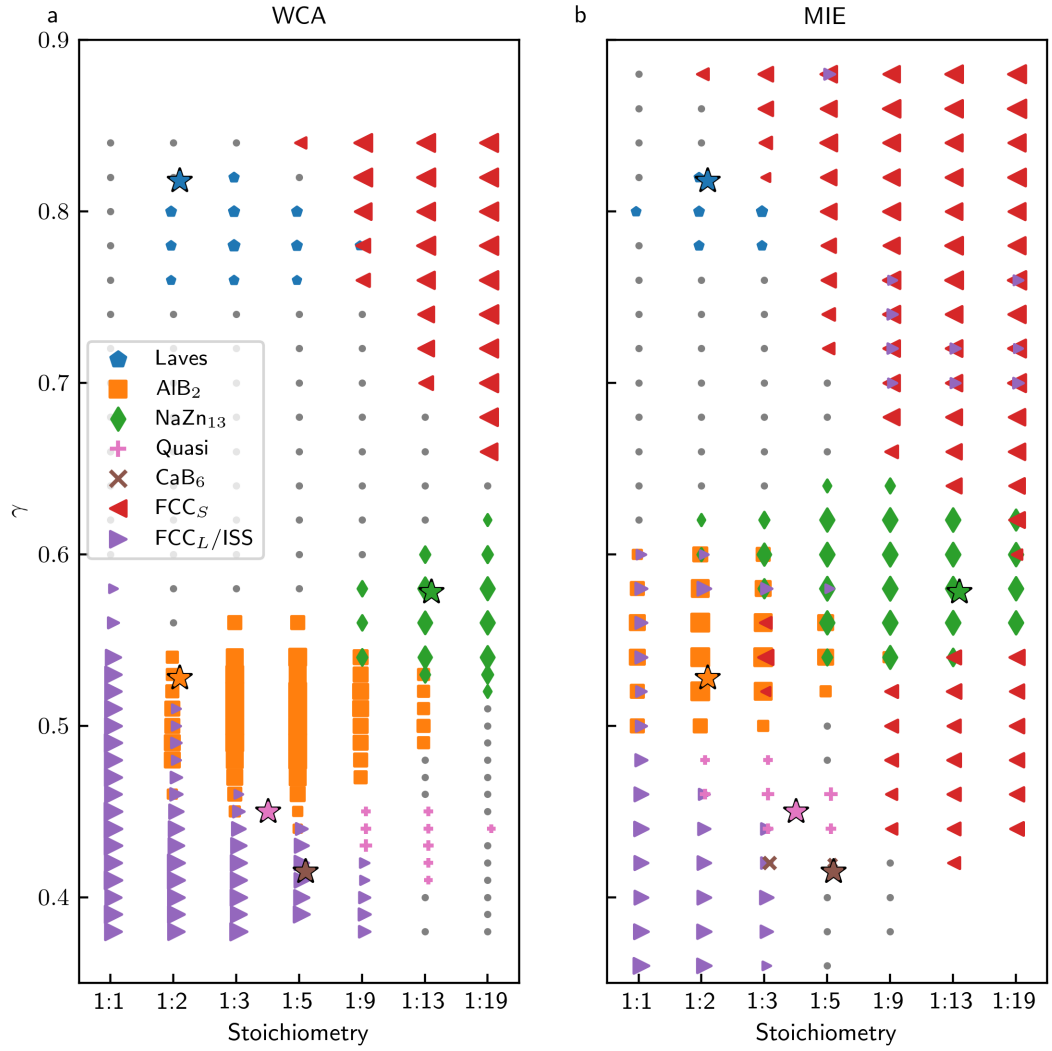

Figure 7.2: The crystal phases self-assembly with a) WCA and b) Mie particles. For a given stoichiometry and size ratio, we report a given crystal as forming if we observe a cluster of 10 particles of that crystal. The size of the marker is proportional to the log of the largest cluster of that crystal in the simulation box. We induced self-assembly through slow compression in a) and slow cooling in b). We indicate the stoichiometry of a crystal and the size ratio where it packs most densely with stars outlined in black.

With the WCA particles we see six distinct phases. These include FCC crystals of the large (FCC_L) and small (FCC_S) particles; three binary crystals reported previously for hard sphere-like particles: the Laves phases, AlB_2, and $NaZn_{13}$; and a quasicrystal phase previously observed in binary nanoparticle superlattices[104]. We note that many of the octahedral voids in FCC_L are occupied by small particles, like in an interstitial solid phase[214] (ISS), but we do not distinguish between the FCC_L and ISS. We do not distinguish between Laves phases, which differ in the stacking of their layers, because we observe a mixture of stackings in our crystallites.

Our detailed sweep of parameter space enables us to better characterize the regions where specific phases self-assemble. It may seem intuitive that a crystal will self-assemble best from a fluid at the crystal's stoichiometry and at the size ratio where the crystal can pack most densely. We indicated these points with stars outlined in black in Figure 7.2. However, with WCA spheres, self-assembly generally occurs most readily with an excess of small particles and at size ratios lower than that at which phase can pack most densely. For example, AlB_2 has a stoichiometry of 1:2 and can pack most densely at $\gamma \approx 0.53$; but the region where it self-assembles is centered around stoichiometries of 1:3-1:5 and $\gamma = 0.5$. We explained the stoichiometry dependence in Chapter V, in which we found that excess small particles promotes mobility and disfavors competing phases with non-attractive particles. The benefit of having smaller particles is less clear, but we suspect it stems from smaller particles having more local free volume (and thus higher entropy).

We observe similar phases with the Mie particles, with the only difference being the appearance of the CaB_6 phase, which has been reported in binary nanoparticle superlattices[106]. This is surprising, as it seemed likely that the attractive well would perturb the system such that multiple new phases self-assemble. Instead, it usually only shifts the size ratios and stoichiometries at which the phases self-assemble. On the phase diagram, the binary phases appear to shift upwards (to higher size ratios) and leftward

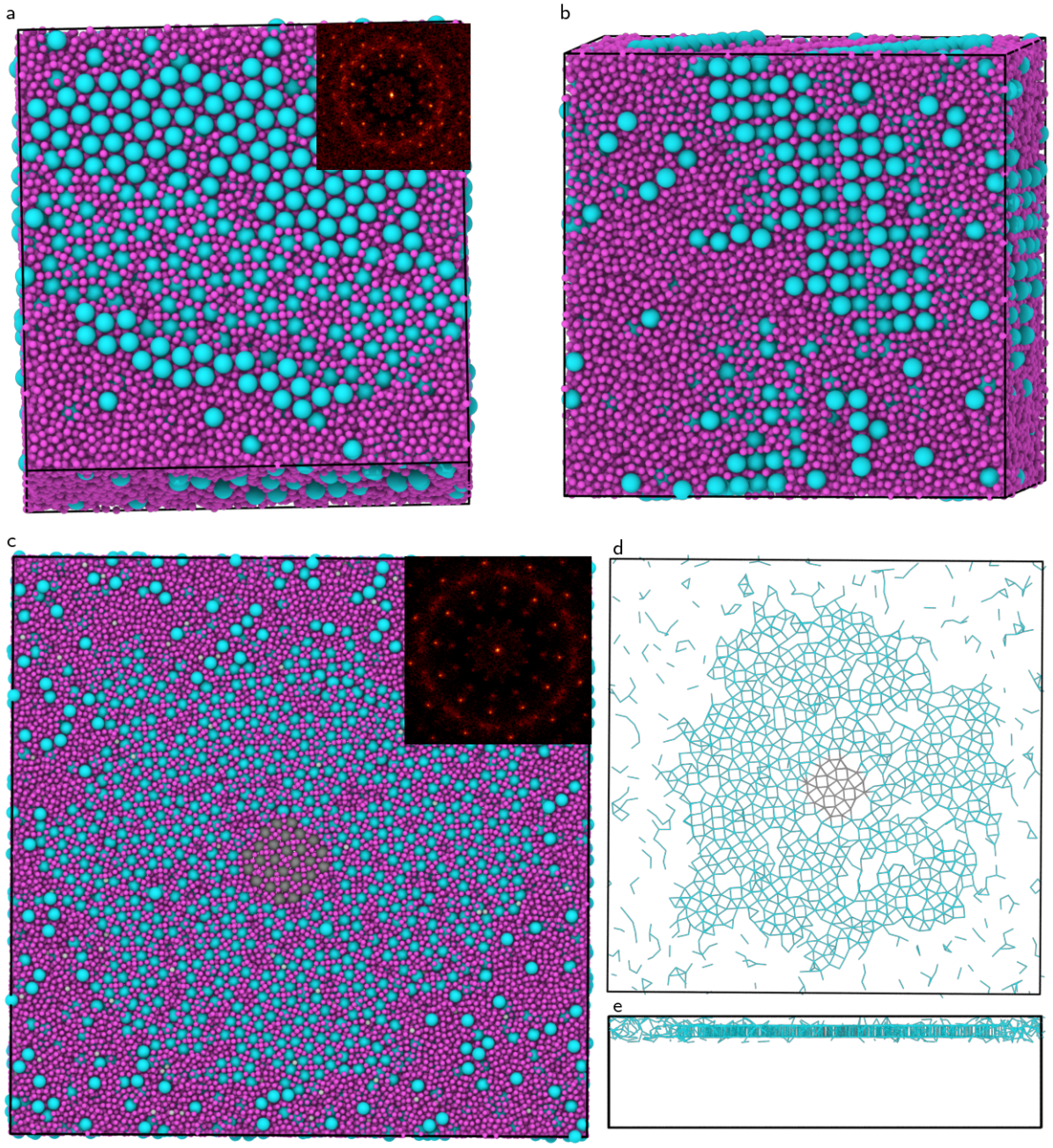

Figure 7.3: The quasicrystal phase self-assembled from WCA particles. In a) and b) we show two perspectives on a quasicrystal spontaneously grown from the fluid a 1:13 and $\gamma = 0.43$. The inset in a) show the 12-fold symmetric diffraction pattern. In c) we show a quasicrystal grown from a fluid phase with a crystalline seed. The grey particle denote the original seed, which was taken from an quasicrystal approximate phase. The 12-fold diffraction pattern shows the quasicrystalline nature of the phase that grew from the seed. In d) we show the bonds between the large particles in c) for a small slice of that simulation. We just show the bonds for two layers, shown by the side view in e), because defects can occur between layers that obscure the triangle-square tiling.

(to fewer small particles), making self-assembly easier at the stoichiometry of the crystal and at or above the size ratio of densest packing.

Better self-assembly at the stoichiometry of the crystal likely stems from less competition from other phases. Removing large particles from the fluid increases the volume available to the remaining particles more so than removing small particles, which can lead to the preferential self-assembly of solid phases richer in large particles than the fluid, as we found in Chapter V. However, when the particles are attractive, the many bonds formed by large particles will decrease their desire to leave the fluid relative to small particles.

Better self-assembly at or above the size ratio of densest packing is likely related to Pauling's first rule[215]: at or above those size ratios, the particles are in contact with more of the neighbors and thus can form more bonds.

It is curious that the same set of phases self-assemble for repulsive and attractive particles. This probably occurs in part because densely packed phases, which tend to be favorable for hard sphere-like particles, tend to have many interparticle contacts, which are favorable for attractive particles. But this does not answer why some phases ($NaZn_{13}$; the Laves phases; the quasicrystal at $\gamma > 0.46$ and $\gamma < 0.45$) that are dense, but not the densest packings, self-assemble for both the WCA and Mie particles. For hard sphere-like particles, the Laves phases[15, 103] and $NaZn_{13}$[87] were found in free energy calculations to benefit from entropy in ways that other phases do not, but it remains to be seen if attractive particles in the same phases also benefit.

7.3 Quasicrystal Formation

The quasicrystal and CaB_6 are the only phases not reported previously for bidisperse particles in simulation[110, 147]. We analyze the self-assembly of the quasicrystal from WCA spheres in more detail due to the novelty of such a complex phase forming from simple interparticle interactions. To grow a larger quasicrystal, we ran a longer simulation

at a stoichiometry of 13:14 and $\gamma = 0.43$. In Figure 7.3a we show a view down the quasicrystalline axis. The inset diffraction pattern shows that it has 12-fold symmetry. In Figure 7.3b, we show a rotated perspective of the same quasicrystal. Many small particles remain in the fluid after the quasicrystal finished growing.

In Figure 7.3c) we show a quasicrystal grown from a columnar seed crystal of an approximate quasicrystal phase. The original seed particles are denoted in grey. We flattened the simulation box to increase the area of the quasicrystalline plane. In Figure 7.3d) we show the bonds between just the large particles of two planes within the structure. The bonds illustrate that the quasicrystal is composed of square and triangle tiles with large particles decorating their vertices. We only show two planes because defects can obscure these tiles; we show a different perspective of these planes and the simulation box in Figure 7.3e). Inline with the quasicrystal reported for binary nanoparticle superlattices[104], the the squares have the same motifs present in a CaB_6 crystal and the triangles have the same motifs present in an AlB_2 crystal.

It is difficult to say whether this quasicrystal is the equilibrium phase, as standard free energy calculations like the Frenkel-Ladd method do not work well on quasicrystals. It is metastable on the time scale of our simulations and grows from the seed of a quasicrystal approximate (as shown in 7.3c). The approximate consists of the square and triangle motifs arranged in a snub-square tiling, which we previously found to be dense packing of binary spheres around size ratios of 0.45 in Chapter IV.

The quasicrystal is notable for being the first quasicrystal reported for hard sphere-like interactions. A quasicrystal approximate (of structure very different from ours) was found for bidisperse hard spheres using type-swap Monte Carlo moves[109]. We did not find their approximate in our simulations, indicating that it is kinetically inhibited.

The quasicrystal observed by Talapin et al.[104] likely does not result from hard sphere-like nanoparticles because (unlike them) we find that a substantial excess of small particles are required to observe it. However, Mie spheres do self-assemble into the quasicrystal at

similar stoichiometries to their experiments. This is consistent with our work in chapter VI, in which we concluded that inter-nanoparticle interactions are characterized by short-ranged attractive forces. Other phases were observed coexisting with the quasicrystal in experiment[104, 216]; we suspect additional forces (like dipole interactions[216]) are responsible their appearance.

7.4 Conclusions

In summary, we constructed a guide for the self-assembly of bidisperse colloidal spheres with nonspecific interactions. We examined both attractive and repulsive particles, finding that they self-assembled similar structures but at different size ratios. We found a quasicrystal phase, indicating that very simple interparticle interactions are required to produce this complex phase of matter.

7.5 Methods

We conducted our simulations using the HOOMD-blue simulation toookit. We truncated interaction range of the WCA spheres at a distance of $2^{1/6}$. All simulations with the WCA spheres were conducted with an NVT integrator based on the MTK equations[155]. We truncated the interaction range of Mie spheres at a distance of 1.7 and shifted the potential by $-7 \cdot 10^{-6}$ such that it is zero at the cutoff. All simulations with the Mie spheres were conducted with an NPT integrator based on the MTK equations[155]. In each case we used 216,000 particles.

We used Steinhardt order parameters and a clustering algorithm[69] to distinguish if particles were in a solid phase. Specifically, we used the Steinhardt order parameters to identify solid-like particles, and then classified a crystal as forming if we detected at least 10 particles of the same crystal in a cluster. In Table 7.1 we give the combinations of parameters used for each crystal.

Table 7.1: Order Parameters for Crystal Identification

N_L:N_S	Sim. Structures
Laves	$(q_4^L < 0.1)(q_6^L < 0.25)(q_6^L > 0.17)(q_9^L < 0.158)(q_8^L < 0.3)$
AlB_2	$(q_4^L < 0.1)(q_8^L > 0.4)(q_9^L < 0.19)(q_{10}^L < 0.23)(q_{12}^L < 0.2)$
$NaZn_{13}$	$(q_6^L < 0.2)(q_9^L > 0.38)$
Quasi	$(q_5^L < 0.09)(q_6^L < 0.09)(q_9^L > 0.16)(q_{10}^L < 0.2)(q_{12}^L < 0.17)$
CaB_6	$(q_4^L > 0.14)(q_6^L < 0.15)(q_9^L < 0.10)(q_{10}^L > 0.18)$
FCC_L/ISS	$(q_8^L > 0.35)(q_9^L < 0.15)(q_{12}^L > 0.25)$
FCC_S	$(q_6^S > 0.45)(q_6^S < 0.6)(q_8^S > 0.35)$

CHAPTER VIII

The Self-Assembly of Atomically Aligned Nanoparticle Superlattices From Heterodimer Nanoparticles

This is a collaborative work with Chris Murray's group at the University of Pennsylvania. Our collaborators in the Murray group performed all experimental work (mostly alluded to in the text).

8.1 Introduction

Multicomponent nanoparticle superlattices, which are composed of two or more species of nanoparticle, have shown promise in integrating nanoparticles made of different materials into the same structure[22, 30, 74, 31, 32, 75, 56, 216, 217, 106, 96]. Typically, these superlattices are synthesized by conducting self-assembly with two distinct types of nanoparticles. An alternative method is to self-assemble conjoined nanoparticles[218, 219], in which the nanoparticles are composed of two different materials segregated into separate lobes. These nanoparticles are called heterodimers[220, 221, 222, 223] and their self-assembly inherently results in a multi-component structure.

The structure of the resulting nanoparticle superlattices can influence their material properties[29, 15, 30, 31, 32, 33, 36]. Phases reported for self-assembling heterodimer particles include a 2D film[218] and an orientationally ordered face-centered cubic crystal (FCC)[219]. Several more structures have been predicted to be stable thermodynamically in simulation[224, 225, 226], although the the lack of experimental reports indicates that their self-assembly may be kinetically limited.

The orientation of the nanoparticles within the superlattice also affects material properties. Particularly interesting are orientations that lead to the long-range alignment between the atomic lattices comprising the nanoparticles. Nanoparticle superlattices exhibiting such order are predicted to have a variety of remarkable properties[227].

Here we show that heterodimer nanoparticles can self-assemble into an atomically aligned nanoparticle superlattice. Our heterodimers are composed of a larger Fe_3O_4 component and a smaller Pt component. Using simulations to guide our efforts, we self-assemble a superlattice in which the Fe_3O_4 components exhibit long-range positional order. Furthermore, the atomic lattices within the Fe_3O_4 components exhibit long-range ordering across the superlattice. We show that the asymmetric shape of our nanoparticles can drive the nanoparticles to adopt a specific orientation, indicating that it is a general method for preparing atomically aligned nanoparticle superlattices.

8.2 Self-Assembly Predictions

To guide our experiments, we first conducted self-assembly simulations examining how the shape of the heterodimers influences their self-assembly behavior. Specifically, we examined the influence of the diameter ratio (γ) of the components and the separation distance (s) between their center of masses. We used a minimal model to simulate the heterodimers, treating each component as hard sphere-like using the Weeks-Chandler-Anderson pair potential[207]. Our model is similar to one used previously[225, 226], but we conduct self-assembly simulations, which capture kinetic limitations, instead of free energy calculations. Our self-assembly simulations consist of a slow compression using molecular dynamics with the HOOMD-blue simulation toolkit[148]. Our results are shown in Figure 8.1a.

We observed the self-assembly of three phases in our simulations: a rotator FCC phase (Figure 8.1c), a NaCl-type phase (Figure 8.1d), and a double FCC phase (Figure8.1e). In the rotator FCC phase, the large components sit at the lattice sites of an FCC crystal

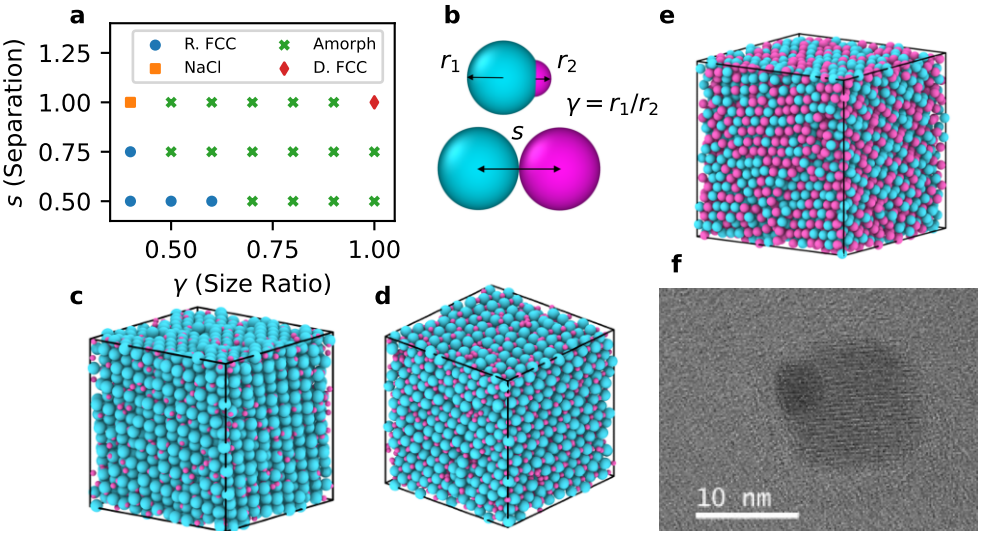

Figure 8.1: Predicting the self-assembly behavior of heterodimer nanoparticles. In a) we show the results of self-assembly simulations conducted at differentcomponent separations (s) and size ratios (γ). We illustrate these two parameters in b). We observe the self-assembly of a c) rotator FCC phase (R. FCC), d) an NaCl phase, and a e) double FCC (D. FCC). We target self-assembly of the rotator FCC phase, so we attempted to synthesize Fe_3O_4-Pt heterodimers at $\gamma = 0.4$ and $s = 0.25$. A transmission electron microscopy image of a single heterodimer is shown in f).

while the small components rotate freely. The NaCl phase is similar, except the small components are confined to octahedral voids formed by the lattice of the large components. We observed these phases when the large component is significantly larger than the small component. In the double FCC phase, both components sit at the lattice site of an FCC crystal. We observed this phase only when the components were equal in size.

Because NaCl and the double FCC phase required separations of 1.0, which are hard to achieve with our nanoparticles, we targeted the experimental self-assembly of the rotator-FCC structure. We synthesized the Fe_3O_4-Pt heterodimer nanoparticles at a target size ratio of 0.4. A transmission electron microscopy image of one of the heterodimers is shown in Figure 8.1f.

8.3 Atomic Alignment

Our experimental collaborators induced self-assembly using the liquid-air interface method. From peaks in the small-angle electron diffraction (SAED), they characterized

the larger Fe_3O_4 component as being in an FCC superlattice, in accordance with the rotator FCC phase. Curiously, they also found distinct peaks within the wide-angle electron diffraction (WAED) pattern, indicating that there is long-range order with regards to the atomic superlattices of each Fe_3O_4 component. Atomic alignment in nanoparticle superlattices has been predicted to have a variety of remarkable properties[227].

The atomic alignment implies that Fe_3O_4 components are orientationally ordered throughout the superlattice and that the position of the Pt component is not random, as we would expect for the rotator FCC phase. Indeed, using the SAED and WAED data, they characterized the Pt component as pointing towards an octahedral void formed by the FCC lattice of Fe_3O_4, contradicting our predictions. The unexpected phase is not NaCl, because each octahedral void is capable of accommodating multiple small components.

We hypothesized that the shape of the heterodimer drives the orientational ordering at high densities. We saw little orientational ordering in our self-assembly simulations, but at higher densities the small components may develop a greater preference for the octahedral voids. We next ran a series of simulations at different packing fractions to quantify this preference. Specifically, we measure the angle θ formed between the orientation vector describing the small component's position and the nearest <100> lattice vector. We initialized this simulations from an already formed rotator FCC phase. In Figure 8.2a, we quantify the probability of a given θ relative to randomly orientated particles.

In Figure 8.2a we clearly see that increasing ϕ drives the smaller component towards the octahedral voids. For example, at $\phi = 0.58$, we find that the small components are ≈ 4 times more likely to point towards the voids than randomly orientated particles, but at $\phi = 0.74$, they are around ≈ 70 times more likely. The increased preference likely results from packing effects, as it is well known that FCC structures can accommodate interstitial species in their octahedral voids (as with NaCl) structure. In driving this orientational alignment, the atomic lattices of different nanoparticles are also driven to

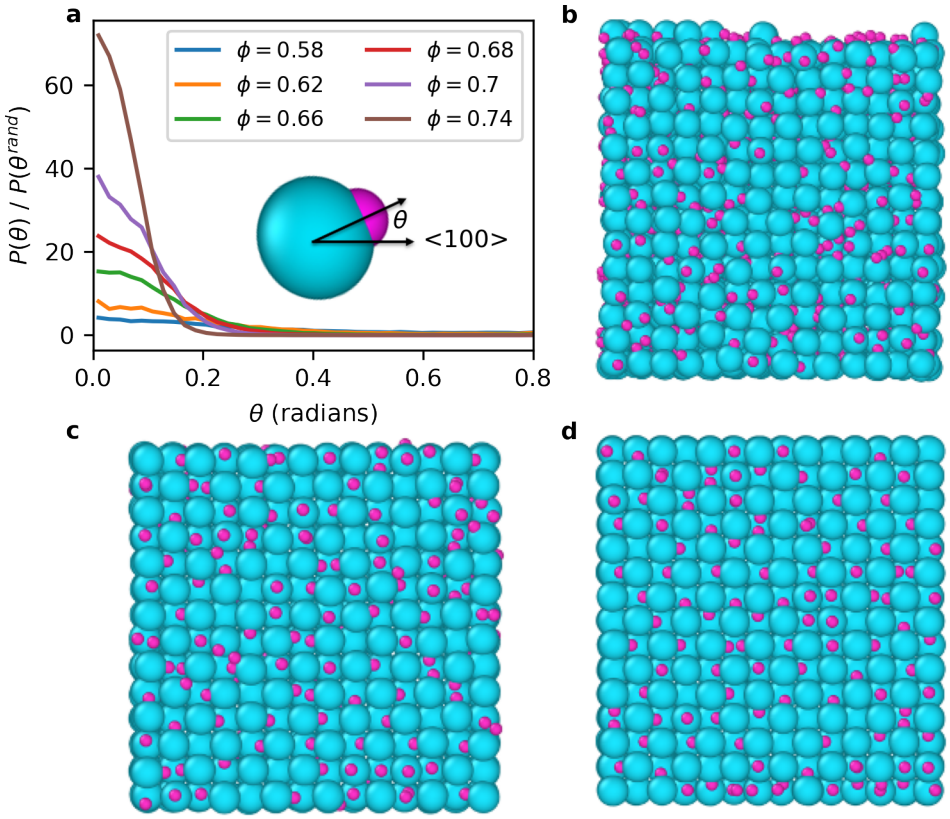

Figure 8.2: Increase in orientational order with packing fraction. In a) we show how the angle θ formed between the orientation vector describing the small component's position and the nearest <100> lattice vector changes with the packing fraction ϕ. The inset illustrates θ. We also show snapshots from our simulations at b) $\phi = 0.58$, c) $\phi = 0.68$, and d) $\phi = 0.74$. The small components are clearly more ordered as ϕ increases.

align.

8.4 Conclusions

In summary, we have self-assembled atomically aligned nanoparticle superlattices from heterodimer nanoparticles. Our nanoparticles were composed of a larger Fe_3O_4 component and a smaller Pt component. We found that the shape of the nanoparticles appears to drive the orientational ordering and consequent alignment between the atomic lattices of the Fe_3O_4 component. The generality of our methods should be useful for future work on self-assembling nanoparticle superlattices with atomic alignment.

8.5 Methods

We conducted all of simulations using the HOOMD-Blue simulation toolkit[148]. We used the Weeks-Chandler-Anderson potential[207] to represent each component of the heterodimer. The distance between the two lobes was constrained by a rigid bond. We simulated our particles at $kT = 0.025$, at which they behave similarly to hard spheres in many aspects[228]. We used the Langevin integrator to thermostat our simulations[156]. In Figure 8.2, we computed the effective packing fraction by approximating the diameter of each component using the prescription given by Barker and Henderson[208].

CHAPTER IX

Conclusions and Outlook

In this dissertation we sought to understand the gaps in our understanding concerning the self-assembly of bidisperse colloids. We have been successful in several respects, but there is still experimental behavior that we cannot explain and questions that we cannot answer.

9.1 Summary

In Chapter IV, we probed the influence of softness on the stability of binary colloidal crystals. We concluded that a very small amount of softness is required to destabilize several dense packings and that several experimentally observed phases are stabilized by softness.

In Chapter V, we demonstrated that stoichiometry could be tuned to promote binary colloidal self-assembly. We found this occurred due to an excess of the smaller component increasing particle mobility and disfavoring competing phases.

In Chapter VI, we collaborated with Chris Murray's group at the University of Pennsylvania to demonstrate that short-ranged attractive forces enabled the self-assembly of binary nanoparticle superlattices. The experimentally observed self-assembly behavior was kinetically limited with the hard sphere models more commonly used to model nanoparticles, but not with particles possessing a narrow attractive well. We then showed that both superlattices observed experimentally formed through homogeneous nucleation in our simulations.

In Chapter VII, we used simulations to construct a guide for the self-assembly of a binary systems with non-specific interactions. We found that hard sphere-like particles and attractive particles self-assemble into similar phases but at different size ratios and stoichiometries. We additionally found a quasicrystal phase, highlighting that complex phases can form for simple interactions.

In Chapter VIII, we again collaborated with the Murray group to examine the self-assembly of heterodimer nanoparticles, which represent a different way to obtain a binary nanoparticle superlattice. We used simulations to guide experiments and explain why an atomically aligned nanoparticle superlattice formed.

9.2 Outlook

Several questions still remain with regards to the self-assembly of bidisperse nanoparticles. Most notable is the formation of phases in experiment that we cannot account for. These include Cu_3Au, Li_3Bi, $Cacu_5$, and BCC-AB_6 phases[22, 56]. We suspect their formation is due to specific and non-additive interactions[99], so exploring these kinds of interactions (particularly dipole interactions[22]) would likely be fruitful. We also note that the work of Alex Travesset[125] concerning the deformation of nanoparticle ligand coronas likely points the way to understanding the formation of some of the remaining the structures.

A second open question is why binary mixtures of shapes typically fail to self-assemble. In this work we revealed that adding an excess of the smaller shape can help in some cases, but many binary mixtures still fail to self-assemble. A colleague, Yuan Zhou, is currently investigating why they are so difficult to self-assemble. Answering this question could lead to new and general ways of designing particles for desirable self-assembly behaviors.

A third open question is why the rate of defect formation is so high in many of the binary crystals we observe. The defects can be observed in every chapter that we attempted self-assembly (Chapters 5 – 8). They include point defects, grain boundaries,

stacking faults, etc. A particularly common defect in systems of IPL and WCA particles is the replacement of a large particle with a cluster of small particles. Here we did not investigate why these defects form, but it would be interesting to examine how varying the parameters of the particles and the system promotes or disfavors these defects.

A fourth open question is why phase separation sometimes occurs in experimental attempts at binary nanoparticle self-assembly. This frequently manifests as the formation of two coexisting nanoparticle superlattices, each containing only one type of nanoparticle[217]. While here we predict phase separation for some types of particles, it can be observed experimentally even for size ratios and stoichiometries where we predict co-crystallization. We could investigate this phenomena by conducting simulations with various combinations of intraspecies and interspecies interactions between particles and seeing where phase separation occurs. Presumably phase separation occurs if intraspecies interactions are more favorable than interspecies interactions, but it would be interesting to quantify the degree of preference necessary to see phase separation and how it is influenced the range and depth of attractive forces.

Finally, it would be interesting to examine the self-assembly of mixtures containing three or more components. Only a few ternary nanoparticle superlattices have been reported in experiment[35], but this may be because fewer researchers have tried ternary self-assembly. It seems intuitive that more components could lead to more structures, as is the case when going from single-component to binary systems, but, as discussed throughout this thesis, co-crystallization can suffer from issues (particularly with regards to the kinetics) that are not present for single-component crystallization. It would be interesting to examine whether a diverse set of colloidal crystals could be obtained in ternary and quaternary systems, as this has large implications for future efforts in obtaining colloidal crystals.

9.3 Concluding Remarks

All things considered, we feel that we pushed past previous boundaries in our knowledge of the self-assembly of bidisperse systems. We expect the principles we elucidated, especially regarding the importance of stoichiometry and short-range attraction, to apply to a wide range of systems beyond those we studied here. We also expect that our guide for self-assembly in nonspecifically interacting systems will be useful for those looking to understand and predict the behavior of their colloidal particles. Finally, it is our hope that others extend our work to conquer the remaining challenges in binary colloidal self-assembly.

APPENDICES

APPENDIX A

The Influence of Thermostats on Nucleation

The contents of this appendix were adapted from a final project report for Professor Yue Fan's course ME 599 in Fall 2018.

A.1 Introduction

In the main text I used a variety of methods to thermostat my simulations. Here I examine the effects of using different thermostatting procedures on nucleation rates for a liquid-solid phase transition. I use brute-force molecular dynamics simulations and a mean first passage time formalism to calculate the nucleation rates. I find that the thermostat can have a large influence on the nucleation rates of a system, but that these differences can be understood largely by examining how the thermostat alters the self-diffusion coefficient of the liquid. My results extend previous work in the literature[229, 230, 228] examining the influence of thermostats on non-equilibrium processes.

A.2 Background

Molecular dynamics (MD) simulations, in which Newton's equations of motion are iteratively solved to produce the time evolution of a system, are commonly used to study dynamic processes such as nucleation. In standard MD simulations, the number of particles, volume, and total energy are conserved. This differs from many experimental systems, for which the energy may vary but the temperature is usually constant, To make better contact with experiment, the dynamics in MD simulations are often altered

to keep the temperature of the simulation constant. These alterations may be designed with the goal of minimizing perturbations to the Newtonian dynamics of a system (e.g. the Nose-Hoover thermostat[231]), or may incorporate other, implicitly simulated phenomena such as Brownian motion to provide thermostatting (Brownian and Langevin Dynamics). At equilibrium in the thermodynamic limit, all thermostats should accurately sample the static properties of a system, which should be identical to those obtained with constant-energy MD. But for dynamic quantities, such as the self-diffusion coefficients, and non-equilibrium processes, such as phase transitions, thermostats may influence measured quantities or even the specific products produced in a reaction. Thus, understanding the influence of thermostats is critical to their application in dynamic simulations. Brief summaries of the thermostats examined here are presented in Figure A.1.

Thermostat	Abbreviation	Brief Description
NVE (None)	NVE	Newton's Laws: $m\ddot{\mathbf{r}} = -\nabla U(\mathbf{r})$
Nose-Hoover $\tau = 2$	NH2	• "Gentle" (e.g. no random forces) • High τ : slower temperature control • Reproduces certain dynamic quantities of NVE simulations (e.g. diffusion)
Nose-Hoover $\tau = 0.2$	NH02	
Langevin $\gamma = 1$	L1	Dampening(γ) + random forces ($R(t)$) to thermalize system: $m\ddot{\mathbf{r}} = -\nabla U(\mathbf{r}) - \gamma\dot{\mathbf{r}} + \sqrt{2\gamma kT}R(t)$
Langevin $\gamma = 10$	L10	
Brownian $\gamma = 1$	B1	Langevin without inertia: $\dot{\mathbf{r}} = \frac{-\nabla U(\mathbf{r}) + \sqrt{2\gamma kT}R(t)}{\gamma}$
Brownian $\gamma = 10$	B10	

Figure A.1: Description of Thermostats Used in this work.

The equations of motion are listed for NVE, Langevin, and Brownian dynamics in Figure A.1. The more complicated dynamics of the Nose-Hoover thermostat can be found in the literature[231]. NVE dynamics are MD without any thermostat, and should reproduce the correct physical behavior of atoms to the degree that atomic interactions

are accurately accounted for in simulation. The Nose-Hoover thermostat is designed to equilibrate a system to a particular temperature with minimal perturbation of the natural dynamics of the system. No random forces are applied to the particles, and certain dynamic properties of NVE simulations are reproduced. The rate at which a simulation equilibrates is controlled by the τ parameter. Langevin dynamics incorporates dampening of the particles velocities and random forces to equilibrate a system. Brownian dynamics is very similar except the particles no longer have inertia, so their momentum returns to zero at the end of every time step. The strength of the random forces in Langevin and Brownian dynamics is controlled by the γ parameter: larger γ will lead to larger random forces and thus stronger perturbations to the natural dynamics.

Crystal nucleation involves an escape from a metastable fluid into a more stable solid. The nucleation of many simpler liquids can be understood qualitatively within the context of classical nucleation theory (CNT)[150]. According to CNT, at any given time the fluid contains many "precritical" nuclei, which are small clusters of particles ordered similarly to the solid. Precritical nuclei continuously form and deform within the fluid. Despite the thermodynamic stability of the solid with respect to the liquid, further growth of the precritical nuclei is disfavored by the interfacial tension between the solid and liquid. However, one precritical nucleus will eventually reach the critical size at which further growth of the crystal will decrease the system's free energy despite the solid-liquid interface. Fluctuations in precritical nuclei are affected by the dynamics of fluid and the particles constituting the nucleus. Thus, it seems reasonable that thermostatting techniques may influence the rate at which crystal nucleation occurs.

A few similar investigations have already been conducted[229, 230, 228] including an examination of the nucleation rates obtained from standard Monte Carlo simulations and MD[230]. In this case the Monte Carlo simulations could essentially be looked at as another form of thermostatting. Inspired by experiment, they found only small deviations from rates calculated with Monte Carlo and MD simulations after normalized their

calculated nucleation rates by the diffusion coefficient of their particles. This indicated that the dynamics differences between the methods only mattered to the degree that it changed the diffusion coefficient of the particles.

A.3 Methodology

MD simulations were conducted with the HOOMD-Blue simulation toolkit[148]. Seven thermostatting schemes were used: (1) no thermostat; Noose-Hoover thermostats[155] with (2) $\tau = 0.2$ and (3) $\tau = 2$; Langevin Dynamics[156] with (4) $\gamma = 1$ and (5) $\gamma = 10$; and Brownian Dynamics[156] with (6) $\gamma = 1$ and (7) $\gamma = 10$. At least 80 independent simulations were conducted with each thermostat. Each simulation consisted of 4000 particles in a cubic box at a number density of 0.78153. Particle interactions were given by a Weeks-Chandler-Anderson[207] (WCA) potential. The simulations would run for $\approx 1.6 \cdot 10^6$ steps at $kT = 1/4$ to produce an equilibrated fluid followed by $\approx 1.6 \cdot 10^7$ steps at $kT = 1/40$ during which we looked for nucleation, where the units of kT are the energy units of the WCA potential. These conditions have been used in previous works to study crystallization[228] and likely correspond to minor (but still present) finite size effects[150]. The self-diffusion rates of the particles were determined from the mean-squared deviation of the fluid in trajectories that did not crystallize. For each thermostat, there were at least 4 such trajectories. At long times, variation in the mean-squared deviation of the particles with time becomes linear; the slope of this relation was used to find the diffusion coefficients. Nucleation rates were determined from the mean-first passage time method (MFPT)[232]. With MFPT, the average time it takes a system to first produce a nucleus of a given size is measured. For a specific nucleus size, the time required to reach nuclei of larger sizes drops very close to zero, and the system rapidly crystallizes. This time is average time needed for nucleation and the inverse of the nucleation rate. We used Steinhardt order parameters[68] to determine the size of the largest crystal nucleus in the system at a given time.

A.4 Results and Discussion

The diffusion coefficients as a function of the thermostat are shown in Figure A.2. The thermostat abbreviations are given in Figure A.1. Standard deviations in the computed values are smaller than the points.

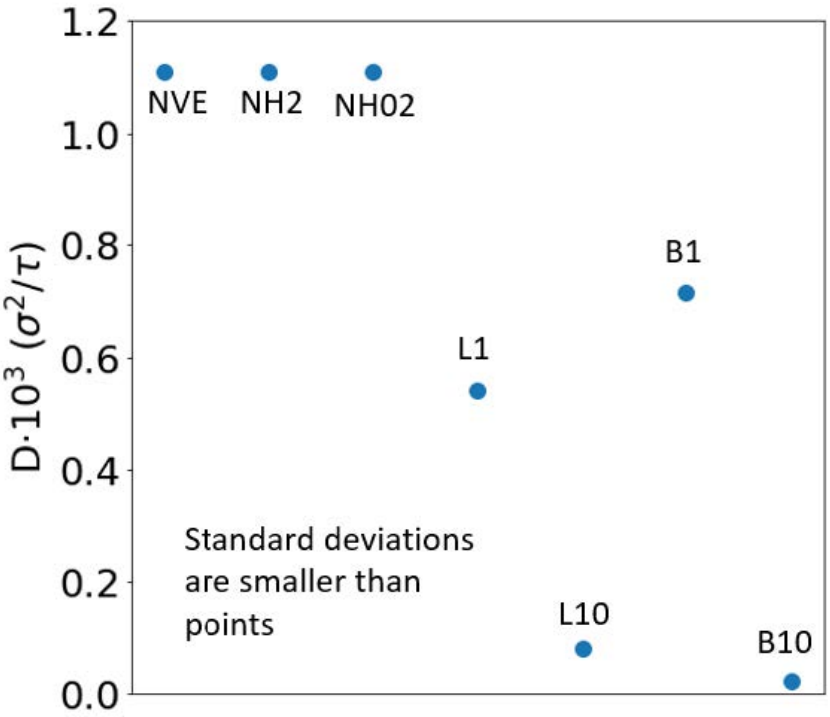

Figure A.2: The self-diffusion constants obtained with the thermostats used in this work.

The diffusion coefficients D for the constant energy and Nose-Hoover thermostats are identical, as is commonly the case. They are also larger than those involving stochastic dampening, as expected. D for the L10 and B10 thermostats, who heavily damp the motion of the particles, are an order magnitude lower than the others. D is a measure of the long-time dynamics of a system, so these differences highlight the large influence that thermostatting can have on a system's dynamic properties.

Calculated nucleation rates as a function of thermostat are shown in Figure A.3. Dividing the "raw" nucleation rates by D may partially account for the influence of the thermostats, so those rates are shown as well. No nucleation events were observed for the B10 thermostat.

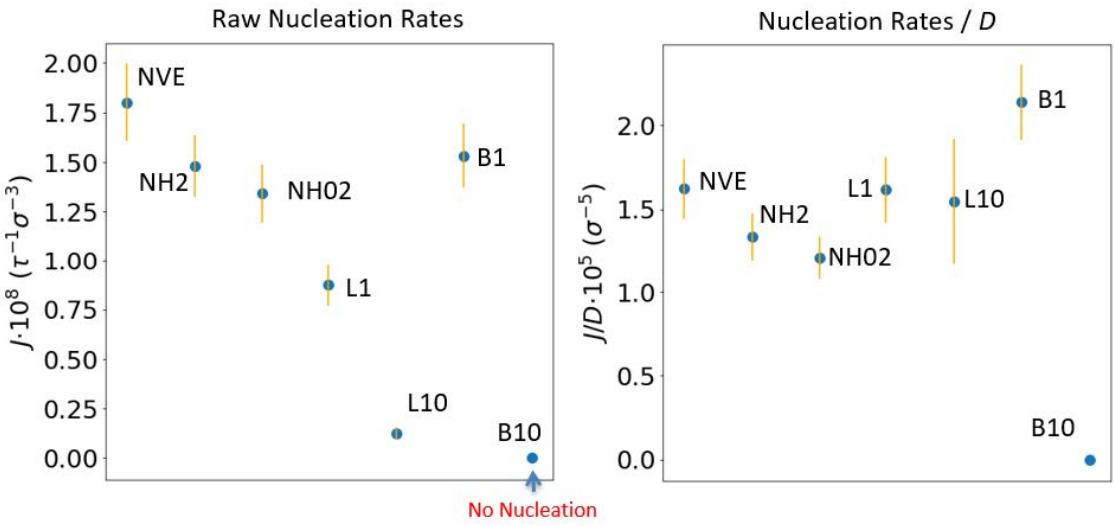

Figure A.3: The nucleation rates obtained with the thermostats used in this work. Raw rates were directly calculated from simulations. The rates in the plot to the right are the raw rates divided by the diffusion coefficients shown in Figure A.2.

The raw nucleation rates shown in Figure A.3 exhibit a clear dependence on the thermostat. NVE has the highest rate, while that of L10 and B10 were much lower. In fact, no nucleation events were observed for B10, demonstrating that thermostatting can have a very large effect on nucleation rates. The other thermostats exhibited nucleation rates only slightly below that of NVE.

Dividing the raw nucleation rates by D generally brings them closer to the NVE rate, as previously reported in similar systems. B10 is an exception because no nucleation events occurred and thus the calculated nucleation rate remained 0. This close correspondence indicates that the long-time diffusion of particles in the system largely controls the nucleation rate.

From these results, we can conclude than any of these thermostats (excepts perhaps B10) are suitable for measuring nucleation rates from experiment, if both computational and experimental nucleation rates are divided by the diffusion coefficient of the particles. Due to the higher raw nucleation rates obtained with the NH thermostats, they seem to be the optimal thermostat when computational costs may be significant.

A.5 Conclusion

Here we have compared MD nucleation rates obtained with a variety of thermostatting schemes. We found that, while the thermostatting scheme affected the "raw" nucleation rate, accounting for the diffusion brought all obtained nucleation rates within 40% of the NVE results. Slight differences do exist in the nucleation rates between different thermostats, which could be the subject of a further study, but the close correspondence in nucleation rates strongly suggests that the thermostatting scheme does not affect the general nucleation pathway taken by the systems under consideration here.

BIBLIOGRAPHY

BIBLIOGRAPHY

[1] M. D. Bentzon, J. van Wonterghem, S. Mørup, A. Thölén, and C. J. W. Koch, "Ordered aggregates of ultrafine iron oxide particles: 'Super crystals'," *Philosophical Magazine B*, vol. 60, pp. 169–178, aug 1989.

[2] C. B. Murray, C. R. Kagan, and M. G. Bawendi, "Self-organization of CdSe nanocrystallites into three-dimensional quantum dot superlattices," *Science*, vol. 270, no. 5240, pp. 1335–1338, 1995.

[3] R. L. Whetten, J. T. Khoury, M. M. Alvarez, S. Murthy, I. Vezmar, Z. L. Wang, P. W. Stephens, C. L. Cleveland, W. D. Luedtke, and U. Landman, "Nanocrystal gold molecules," *Advanced materials*, vol. 8, no. 5, pp. 428–433, 1996.

[4] B. A. Korgel and D. Fitzmaurice, "Condensation of ordered nanocrystal thin films," *Physical review letters*, vol. 80, no. 16, p. 3531, 1998.

[5] S. Sun and C. B. Murray, "Synthesis of monodisperse cobalt nanocrystals and their assembly into magnetic superlattices," *Journal of applied Physics*, vol. 85, no. 8, pp. 4325–4330, 1999.

[6] S. Sun, C. B. Murray, D. Weller, L. Folks, and A. Moser, "Monodisperse FePt nanoparticles and ferromagnetic FePt nanocrystal superlattices," *Science*, vol. 287, no. 5460, pp. 1989–1992, 2000.

[7] P. N. Pusey and W. van Megen, "Phase behaviour of concentrated suspensions of nearly hard colloidal spheres," *Nature*, vol. 320, no. 6060, pp. 340–342, 1986.

[8] H. Senff and W. Richtering, "Temperature sensitive microgel suspensions: Colloidal phase behavior and rheology of soft spheres," *The Journal of chemical physics*, vol. 111, no. 4, pp. 1705–1711, 1999.

[9] T. Palberg, A. Stipp, and E. Bartsch, "Unusual Crystallization Kinetics in a Hard Sphere Colloid-Polymer Mixture," *Phys. Rev. Lett.*, vol. 102, p. 38302, jan 2009.

[10] J. B. JONES, J. V. SANDERS, and E. R. SEGNIT, "Structure of Opal," *Nature*, vol. 204, no. 4962, pp. 990–991, 1964.

[11] J. D. Bernal and I. Fankuchen, "X-ray and crystallographic studies of plant virus preparations: I. Introduction and preparation of specimens II. Modes of aggregation of the virus particles," *The Journal of general physiology*, vol. 25, no. 1, pp. 111–146, 1941.

[12] R. C. WILLIAMS and K. M. SMITH, "A Crystallizable Insect Virus," *Nature*, vol. 179, no. 4551, pp. 119–120, 1957.

[13] D. V. Talapin, J. S. Lee, M. V. Kovalenko, and E. V. Shevchenko, "Prospects of colloidal nanocrystals for electronic and optoelectronic applications," *Chem. Rev.*, vol. 110, pp. 389–458, 2010.

[14] J. I. Martın, J. Nogs, K. Liu, J. L. Vicent, and I. K. Schuller, "Ordered magnetic nanostructures: fabrication and properties," *Journal of Magnetism and Magnetic Materials*, vol. 256, no. 1, pp. 449–501, 2003.

[15] A. P. Hynninen, J. H. Thijssen, E. C. Vermolen, M. Dijkstra, and A. Van Blaaderen, "Self-assembly route for photonic crystals with a bandgap in the visible region," *Nat. Mater.*, vol. 6, pp. 202–205, 2007.

[16] S. Hachisu and S. Yoshimura, "Optical demonstration of crystalline superstructures in binary mixtures of latex globules," *Nature*, vol. 283, p. 188, 1980.

[17] S. Yoshimura and S. Hachisu, "Order formation in binary mixtures of monodisperse latices," *Frontiers in Colloid Science In Memoriam Professor Dr. Bun-ichi Tamamushi*, pp. 59–70, 1983.

[18] P. Bartlett, R. Ottewill, and P. N. Pusey, "Superlattice Formation in Binary Mixtures of Hard Sphere Colloids," *Phys. Rev. Lett.*, vol. 68, pp. 3801–3804, 1992.

[19] F. X. Redl, K.-S. Cho, C. B. Murray, and S. O'Brien, "Three-dimensional binary superlattices of magnetic nanocrystals and semiconductor quantum dots," *Nature*, vol. 423, no. 6943, pp. 968–971, 2003.

[20] M. E. Leunissen, C. G. Christova, A.-p. Hynninen, C. P. Royall, A. I. Campbell, A. Imhof, M. Dijkstra, R. van Roij, and A. van Blaaderen, "Ionic colloidal crystals of oppositely charged particles," *Nature*, vol. 437, no. 7056, pp. 235–240, 2005.

[21] P. Bartlett and A. I. Campbell, "Three-dimensional binary superlattices of oppositely charged colloids," *Physical review letters*, vol. 95, no. 12, p. 128302, 2005.

[22] E. V. Shevchenko, D. V. Talapin, N. A. Kotov, S. O'Brien, and C. B. Murray, "Structural diversity in binary nanoparticle superlattices.," *Nature*, vol. 439, pp. 55–59, 2006.

[23] X. Huang, J. Zhou, M. Fu, B. Li, Y. Wang, Q. Zhao, Z. Yang, Q. Xie, and L. Li, "Binary colloidal crystals with a wide range of size ratios via template-assisted electric-field-induced assembly," *Langmuir*, vol. 23, no. 17, pp. 8695–8698, 2007.

[24] E. C. M. Vermolen, A. Kuijk, L. C. Filion, M. Hermes, J. H. J. Thijssen, M. Dijkstra, and A. Van Blaaderen, "Fabrication of large binary colloidal crystals with a NaCl structure," *Proceedings of the National Academy of Sciences*, vol. 106, no. 38, pp. 16063–16067, 2009.

[25] A. Dong, J. Chen, P. M. Vora, J. M. Kikkawa, and C. B. Murray, "Binary nanocrystal superlattice membranes self-assembled at the liquid–air interface," *Nature*, vol. 466, no. 7305, pp. 474–477, 2010.

[26] N. Schaertl, D. Botin, T. Palberg, and E. Bartsch, "Formation of Laves phases in buoyancy matched hard sphere suspensions," *Soft Matter*, vol. 14, pp. 5130–5139, 2018.

[27] W. Steurer and J. Dshemuchadse, *Intermetallics : structures, properties, and statistics*. Oxford University Press, 2016.

[28] E. V. Shevchenko, D. V. Talapin, C. B. Murray, and S. O'Brien, "Structural characterization of self-assembled multifunctional binary nanoparticle superlattices," *Journal of the American Chemical Society*, vol. 128, no. 11, pp. 3620–3637, 2006.

[29] J. J. Urban, D. V. Talapin, E. V. Shevchenko, C. R. Kagan, and C. B. Murray, "Synergism in binary nanocrystal superlattices leads to enhanced p-type conductivity in self-assembled PbTe/Ag 2 Te thin films," *Nature materials*, vol. 6, no. 2, pp. 115–121, 2007.

[30] E. V. Shevchenko, M. Ringler, A. Schwemer, D. V. Talapin, T. A. Klar, A. L. Rogach, J. Feldmann, and A. P. Alivisatos, "Self-Assembled Binary Superlattices of CdSe and Au Nanocrystals and Their Fluorescence Properties," *Journal of the American Chemical Society*, vol. 130, pp. 3274–3275, mar 2008.

[31] Y. Kang, X. Ye, J. Chen, L. Qi, R. E. Diaz, V. Doan-Nguyen, G. Xing, C. R. Kagan, J. Li, R. J. Gorte, E. A. Stach, and C. B. Murray, "Engineering catalytic contacts and thermal stability: Gold/iron oxide binary nanocrystal superlattices for CO oxidation," *J. Am. Chem. Soc.*, vol. 135, pp. 1499–1505, 2013.

[32] X. Ye, J. Chen, B. T. Diroll, and C. B. Murray, "Tunable plasmonic coupling in self-assembled binary nanocrystal superlattices studied by correlated optical microspectrophotometry and electron microscopy," *Nano Lett.*, vol. 13, pp. 1291–1297, 2013.

[33] J. Chen, X. Ye, S. J. Oh, J. M. Kikkawa, C. R. Kagan, and C. B. Murray, "Bistable Magnetoresistance Switching in Exchange-Coupled CoFe2O4–Fe3O4 Binary Nanocrystal Superlattices by Self-Assembly and Thermal Annealing," *ACS Nano*, vol. 7, pp. 1478–1486, 2013.

[34] C. B. Murray, C. R. Kagan, and M. G. Bawendi, "Synthesis and Characterization of Monodisperse Nanocrystals and Close-Packed Nanocrystal Assemblies," *Annual Review of Materials Science*, vol. 30, pp. 545–610, aug 2000.

[35] M. A. Boles, M. Engel, and D. V. Talapin, "Self-assembly of colloidal nanocrystals: From intricate structures to functional materials," *Chem. Rev.*, vol. 116, pp. 11220–11289, 2016.

[36] R. K. Cersonsky, J. Antonaglia, B. D. Dice, and S. C. Glotzer, "The diversity of three-dimensional photonic crystals," *Nature Communications*, vol. 12, no. 1, p. 2543, 2021.

[37] K. Kremer, M. O. Robbins, and G. S. Grest, "Phase Diagram of Yukawa Systems: Model for Charge-Stabilized Colloids," *Phys. Rev. Lett.*, vol. 57, pp. 2694–2697, nov 1986.

[38] M. O. Robbins, K. Kremer, and G. S. Grest, "Phase diagram and dynamics of Yukawa systems," *J. Chem. Phys.*, vol. 88, pp. 3286–3312, 1988.

[39] R. T. Scarlett, M. T. Ung, J. C. Crocker, and T. Sinno, "A mechanistic view of binary colloidal superlattice formation using DNA-directed interactions," *Soft Matter*, vol. 7, no. 5, pp. 1912–1925, 2011.

[40] P. Varilly, S. Angioletti-Uberti, B. M. Mognetti, and D. Frenkel, "A general theory of DNA-mediated and other valence-limited colloidal interactions," *The Journal of chemical physics*, vol. 137, no. 9, p. 94108, 2012.

[41] H. Lin, S. Lee, L. Sun, M. Spellings, M. Engel, S. C. Glotzer, and C. A. Mirkin, "Clathrate colloidal crystals," *Science*, vol. 355, pp. 931–935, mar 2017.

[42] E. Pretti, H. Zerze, M. Song, Y. Ding, N. A. Mahynski, H. W. Hatch, V. K. Shen, and J. Mittal, "Assembly of three-dimensional binary superlattices from multi-flavored particles," *Soft Matter*, vol. 14, no. 30, pp. 6303–6312, 2018.

[43] Z. Tang, Z. Zhang, Y. Wang, S. C. Glotzer, and N. A. Kotov, "Self-Assembly of CdTe Nanocrystals into Free-Floating Sheets," *Science*, vol. 314, pp. 274–278, oct 2006.

[44] A. Ben-simon, H. Eshet, and E. Rabani, "On the Phase Behavior of Binary Mixtures of Nanoparticles," *ACS Nano*, vol. 7, pp. 978–986, 2013.

[45] Z. Zhang and S. C. Glotzer, "Self-assembly of patchy particles," *Nano Letters*, vol. 4, no. 8, pp. 1407–1413, 2004.

[46] U. Agarwal and F. A. Escobedo, "Mesophase behaviour of polyhedral particles.," *Nature materials*, vol. 10, pp. 230–5, mar 2011.

[47] P. F. Damasceno, M. Engel, and S. C. Glotzer, "Predictive Self-Assembly of Polyhedra into Complex Structures," *Science*, vol. 337, pp. 453 – 457, jul 2012.

[48] N. A. Mahynski, E. Pretti, V. K. Shen, and J. Mittal, "Using symmetry to elucidate the importance of stoichiometry in colloidal crystal assembly," *Nature Communications*, vol. 10, no. 1, p. 2028, 2019.

[49] G. Van Anders, D. Klotsa, A. S. Karas, P. M. Dodd, and S. C. Glotzer, "Digital Alchemy for Materials Design: Colloids and Beyond," *ACS Nano*, vol. 9, no. 10, pp. 9542–9553, 2015.

[50] C. S. Adorf, J. Antonaglia, J. Dshemuchadse, and S. C. Glotzer, "Inverse design of simple pair potentials for the self-assembly of complex structures," *Journal of Chemical Physics*, vol. 149, p. 204102, nov 2018.

[51] W. D. Piñeros, B. A. Lindquist, R. B. Jadrich, and T. M. Truskett, "Inverse design of multicomponent assemblies," *The Journal of Chemical Physics*, vol. 148, p. 104509, mar 2018.

[52] Z. M. Sherman, M. P. Howard, B. A. Lindquist, R. B. Jadrich, and T. M. Truskett, "Inverse methods for design of soft materials," *The Journal of Chemical Physics*, vol. 152, p. 140902, apr 2020.

[53] S. C. Glotzer and M. J. Solomon, "Anisotropy of building blocks and their assembly into complex structures," *Nature Materials*, vol. 6, pp. 557–562, aug 2007.

[54] N. A. Mahynski and V. K. Shen, "Symmetry-derived structure directing agents for two-dimensional crystals of arbitrary colloids," *Soft Matter*, vol. 17, no. 34, pp. 7853–7866, 2021.

[55] T. C. Moore, J. A. Anderson, and S. C. Glotzer, "Shape-driven entropic self-assembly of an open, reconfigurable, binary host–guest colloidal crystal," *Soft Matter*, vol. 17, no. 10, pp. 2840–2848, 2021.

[56] M. A. Boles and D. V. Talapin, "Many-Body Effects in Nanocrystal Superlattices: Departure from Sphere Packing Explains Stability of Binary Phases," *J. Am. Chem. Soc.*, vol. 137, pp. 4494–4502, 2015.

[57] M. A. J.M. Smith, H.C. Van Ness, *Introduction to Chemical Engineering Thermodynamics*. Boston: McGraw-Hill, 7th ed., 2005.

[58] J. W. Gibbs, *Elementary principles in statistical mechanics: developed with especial reference to the rational foundations of thermodynamics*. C. Scribner's sons, 1902.

[59] R. A. LaCour, C. S. Adorf, J. Dshemuchadse, and S. C. Glotzer, "Influence of Softness on the Stability of Binary Colloidal Crystals," *ACS Nano*, vol. 13, pp. 13829–13842, dec 2019.

[60] C. Desgranges and J. Delhommelle, "Controlling Polymorphism during the Crystallization of an Atomic Fluid," *Phys. Rev. Lett.*, vol. 98, p. 235502, jun 2007.

[61] P. G. Debenedetti and F. H. Stillinger, "Supercooled liquids and the glass transition," *Nature*, vol. 410, no. 6825, pp. 259–267, 2001.

[62] E. Sanz, C. Valeriani, D. Frenkel, and M. Dijkstra, "Evidence for Out-of-Equilibrium Crystal Nucleation in Suspensions of Oppositely Charged Colloids," *Phys. Rev. Lett.*, vol. 99, p. 55501, aug 2007.

[63] B. Peters, "Competing nucleation pathways in a mixture of oppositely charged colloids: Out-of-equilibrium nucleation revisited," *Journal of Chemical Physics*, vol. 131, p. 244103, dec 2009.

[64] D. Kashchiev, *Nucleation*. Oxford: Elsevier, 2000.

[65] J. A. Anderson, C. D. Lorenz, and A. Travesset, "General purpose molecular dynamics simulations fully implemented on graphics processing units," *Journal of Computational Physics*, vol. 227, pp. 5342–5359, 2008.

[66] J. Glaser, T. D. Nguyen, J. A. Anderson, P. Lui, F. Spiga, J. A. Millan, D. C. Morse, and S. C. Glotzer, "Strong scaling of general-purpose molecular dynamics simulations on GPUs," *Computer Physics Communications*, vol. 192, pp. 97–107, 2015.

[67] D. Frenkel and B. Smit, *Understanding molecular simulation: from algorithms to applications*, vol. 1. Elsevier, 2001.

[68] P. J. Steinhardt, D. R. Nelson, and M. Ronchetti, "Bond-orientational order in liquids and glasses," *Physical Review B*, vol. 28, pp. 784–805, jul 1983.

[69] V. Ramasubramani, B. D. Dice, E. S. Harper, M. P. Spellings, J. A. Anderson, and S. C. Glotzer, "freud: A software suite for high throughput analysis of particle simulation data," *Computer Physics Communications*, vol. 254, p. 107275, sep 2020.

[70] D. Frenkel and A. J. C. Ladd, "New Monte Carlo method to compute the free energy of arbitrary solids. Application to the fcc and hcp phases of hard spheres," *The Journal of Chemical Physics*, vol. 81, pp. 3188–3193, 1984.

[71] C. Vega and E. G. Noya, "Revisiting the Frenkel-Ladd method to compute the free energy of solids: The Einstein molecule approach," *Journal of Chemical Physics*, vol. 127, pp. 1–12, 2007.

[72] A. Stukowski, "Visualization and analysis of atomistic simulation data with OVITO–the Open Visualization Tool," *Modelling and Simulation in Materials Science and Engineering*, vol. 18, p. 015012, dec 2010.

[73] C. S. Adorf, P. M. Dodd, V. Ramasubramani, and S. C. Glotzer, "Simple data and workflow management with the signac framework," *Comput. Mater. Sci.*, vol. 146, pp. 220–229, 2018.

[74] W. H. Evers, B. D. Nijs, L. Filion, S. Castillo, M. Dijkstra, and D. Vanmaekelbergh, "Entropy-driven formation of binary semiconductor-nanocrystal superlattices," *Nano Lett.*, vol. 10, pp. 4235–4241, 2010.

[75] X. Ye, C. Zhu, P. Ercius, S. N. Raja, B. He, M. R. Jones, M. R. Hauwiller, Y. Liu, T. Xu, and A. P. Alivisatos, "Structural diversity in binary superlattices self-assembled from polymer-grafted nanocrystals," *Nat. Commun.*, vol. 6, p. 10052, 2015.

[76] M. J. Murray and J. V. Sanders, "Close-packed structures of spheres of two different sizes II. The packing densities of likely arrangements," *Philosophical Magazine A*, vol. 42, no. 6, pp. 721–740, 1980.

[77] Z. Chen, J. Moore, G. Radtke, H. Sirringhaus, and S. O'Brien, "Binary nanoparticle superlattices in the semiconductor-semiconductor system: CdTe and CdSe," *J. Am. Chem. Soc.*, vol. 129, pp. 15702–15709, 2007.

[78] X. Ye, J. Chen, M. Engel, J. A. Millan, W. Li, L. Qi, G. Xing, J. E. Collins, C. R. Kagan, J. Li, S. C. Glotzer, and C. B. Murray, "Competition of shape and interaction patchiness for self-assembling nanoplates," *Nat. Chem.*, vol. 5, p. 466, 2013.

[79] B. A. Schultz, P. F. Damasceno, M. Engel, and S. C. Glotzer, "Symmetry Considerations for the Targeted Assembly of Entropically Stabilized Colloidal Crystals via Voronoi Particles," *ACS Nano*, vol. 9, pp. 2336–2344, 2015.

[80] S. Torquato, "Perspective: Basic understanding of condensed phases of matter via packing models," *J. Chem. Phys.*, vol. 149, p. 20901, 2018.

[81] N. J. Lorenz, J. H. Schope, R. Holger, T. Palberg, P. Wette, I. Klassen, D. Holland-Moritz, D. Herlach, and T. Okubo, "Phase behaviour of deionized binary mixtures of charged colloidal spheres," *J. Phys. Condens. Matter*, vol. 21, p. 464116, 2009.

[82] A. P. Kaushik and P. Clancy, "Solvent-driven symmetry of self-assembled nanocrystal superlattices - A computational study," *J. Comput. Chem.*, vol. 34, pp. 523–532, 2013.

[83] R. K. Cersonsky, G. van Anders, P. M. Dodd, and S. C. Glotzer, "Relevance of Packing to Colloidal Self-Assembly," *Proc. Natl. Acad. Sci. U.S.A.*, vol. 115, pp. 1439–1444, 2018.

[84] G. Bryant, S. R. Williams, L. Qian, I. K. Snook, E. Perez, and F. Pincet, "How hard is a colloidal "hard-sphere" interaction?," *Phys. Rev. E*, vol. 66, p. 60501, 2002.

[85] C. P. Royall, W. C. K. Poon, and E. R. Weeks, "In search of colloidal hard spheres," *Soft Matter*, vol. 9, pp. 17–27, 2012.

[86] A. Travesset, "Binary nanoparticle superlattices of soft-particle systems," *Proc. Natl. Acad. Sci. U.S.A.*, vol. 112, pp. 9563–9567, 2015.

[87] M. D. Eldridge, P. A. Madden, and D. Frenkel, "Entropy-driven formation of a superlattice in a hard-sphere binary mixture," *Nature*, vol. 365, pp. 35–37, 1993.

[88] D. Frenkel, "Entropy-driven phase transitions," *Physica A*, vol. 263, pp. 26–38, 1999.

[89] M. Dijkstra, R. van Roij, and R. Evans, "Phase diagram of highly asymmetric binary hard-sphere mixtures," *Physical Review E*, vol. 59, no. 5, pp. 5744–5771, 1999.

[90] A. P. Hynninen, L. Filion, and M. Dijkstra, "Stability of LS and L S2 crystal structures in binary mixtures of hard and charged spheres," *J . Chem. Phys.*, vol. 131, p. 064902, 2009.

[91] W. G. Hoover, M. Ross, K. W. Johnson, D. Henderson, J. A. Barker, and B. C. Brown, "Soft Sphere Equation of State," *J. Chem. Phys.*, vol. 52, pp. 4931–4941, 1970.

[92] J. Hansen and D. Schiff, "Influence of interatomic repulsion on the structure of liquids at melting," *Mol. Phys.*, vol. 25, pp. 1281–1290, 1973.

[93] N. Horst and A. Travesset, "Prediction of binary nanoparticle superlattices from soft potentials," *J. Chem. Phys.*, vol. 144, p. 014502, 2016.

[94] P. I. O'Toole and T. S. Hudson, "New High-Density Packings of Similarly Sized Binary Spheres," *The Journal of Physical Chemistry C*, vol. 115, pp. 19037–19040, oct 2011.

[95] M. D. Eldridge, P. A. Madden, P. N. Pusey, and P. Bartlett, "Binary hard-sphere mixtures: A comparison between computer simulation and experiment," *Mol. Phys.*, vol. 84, pp. 395–420, 1995.

[96] M. I. Bodnarchuk, M. V. Kovalenko, W. Heiss, and D. V. Talapin, "Energetic and entropic contributions to self-assembly of binary nanocrystal superlattices: Temperature as the structure-directing factor," *J. Am. Chem. Soc.*, vol. 132, pp. 11967–11977, 2010.

[97] A. Travesset, "Phase diagram of power law and Lennard-Jones systems: Crystal phases," *J. Chem. Phys.*, vol. 141, p. 164501, 2014.

[98] J. Schneider, M. Wiemann, A. Rabe, and E. Bartsch, "On tuning microgel character and softness of cross-linked polystyrene particles," *Soft Matter*, vol. 13, pp. 445–457, 2017.

[99] C. Batista, R. G. Larson, and N. A. Kotov, "Nonadditivity of nanoparticle interactions," *Science*, vol. 350, p. 1242477, oct 2015.

[100] G. Bergerhoff, R. Hundt, R. Sievers, and I. D. Brown, "The inorganic crystal structure data base," *J. Chem. Inf. Model.*, vol. 23, pp. 66–69, 1983.

[101] A. B. Hopkins, Y. Jiao, F. H. Stillinger, and S. Torquato, "Phase Diagram and Structural Diversity of the Densest Binary Sphere Packings," *Phys. Rev. Lett.*, vol. 107, p. 125501, 2011.

[102] A. B. Hopkins, F. H. Stillinger, and S. Torquato, "Densest binary sphere packings," *Phys. Rev. E*, vol. 85, p. 021130, 2012.

[103] L. Filion and M. Dijkstra, "Prediction of binary hard-sphere crystal structures," *Phys. Rev. E.*, vol. 79, p. 46714, 2009.

[104] D. V. Talapin, E. V. Shevchenko, M. I. Bodnarchuk, X. Ye, J. Chen, and C. B. Murray, "Quasicrystalline order in self-assembled binary nanoparticle superlattices.," *Nature*, vol. 461, pp. 964–967, 2009.

[105] J. K. Kummerfeld, T. S. Hudson, and P. Harrowell, "The densest packing of AB binary hard-sphere homogeneous compounds across all size ratios," *J. Phys. Chem. B.*, vol. 112, pp. 10773–10776, 2008.

[106] X. Ye, J. Chen, and C. B. Murray, "Polymorphism in self-assembled AB6 binary nanocrystal superlattices," *J. Am. Chem. Soc.*, vol. 133, pp. 2613–2620, 2011.

[107] S. R. Ganagalla and S. N. Punnathanam, "Free energy barriers for homogeneous crystal nucleation in a eutectic system of binary hard spheres," *Journal of Chemical Physics*, vol. 138, no. 17, 2013.

[108] P. K. Bommineni and S. N. Punnathanam, "Molecular simulation of homogeneous crystal nucleation of AB2solid phase from a binary hard sphere mixture," *Journal of Chemical Physics*, vol. 147, no. 6, 2017.

[109] P. K. Bommineni, N. R. Varela-Rosales, M. Klement, and M. Engel, "Complex Crystals from Size-Disperse Spheres.," *Phys. Rev. Lett.*, vol. 122, p. 128005, mar 2019.

[110] T. Dasgupta, G. M. Coli, and M. Dijkstra, "Tuning the Glass Transition: Enhanced Crystallization of the Laves Phases in Nearly Hard Spheres," *ACS Nano*, vol. 14, pp. 3957–3968, 4 2020.

[111] S. Prestipino, F. Saija, and P. V. Giaquinta, "Phase diagram of softly repulsive systems: The Gaussian and inverse-power-law potentials," *J. Chem. Phys.*, vol. 123, p. 144110, 2005.

[112] R. Agrawal and D. A. Kofke, "Thermodynamic and structural properties of model systems at solid-fluid coexistence," *Mol. Phys.*, vol. 85, pp. 23–42, 1995.

[113] T. W. Melnyk, O. Knop, and W. R. Smith, "Extremal arrangements of points and unit charges on a sphere: equilibrium configurations revisited," *Can. J. Chem.*, vol. 55, pp. 1745–1761, 1977.

[114] B. W. Clare and D. L. Kepert, "The closest packing of equal circles on a sphere," *Proc. Royal. Soc. Lond. A*, vol. 405, pp. 329–344, 1986.

[115] A. Travesset, "Nanoparticle Superlattices as Quasi-Frank-Kasper Phases," *Phys. Rev. Lett.*, vol. 119, p. 115701, 2017.

[116] D. M. Heyes and A. C. Brańka, "The influence of potential softness on the transport coefficients of simple fluids," *J. Chem. Phys.*, vol. 122, p. 234504, 2005.

[117] E. Lange, J. B. Caballero, A. M. Puertas, and M. Fuchs, "Comparison of structure and transport properties of concentrated hard and soft sphere fluids," *J. Chem. Phys.*, vol. 130, p. 174903, 2009.

[118] S. D. Finlayson and P. Bartlett, "Non-additivity of pair interactions in charged colloids," *J. Chem. Phys.*, vol. 145, p. 34905, 2016.

[119] D. M. Herlach, T. Palberg, I. Klassen, S. Klein, and R. Kobold, "Overview: Experimental studies of crystal nucleation: Metals and colloids," *J. Chem. Phys.*, vol. 145, p. 211703, 2016.

[120] G. I. Kerley, "Equations of state and gas–gas separation in soft-sphere mixtures," *The Journal of Chemical Physics*, vol. 91, pp. 1204–1210, 1989.

[121] R. J. Macfarlane, B. Lee, M. R. Jones, N. Harris, G. C. Schatz, and C. A. Mirkin, "Nanoparticle Superlattice Engineering with DNA," *Science*, vol. 334, pp. 204–208, 2011.

[122] T. Vo, V. Venkatasubramanian, S. Kumar, B. Srinivasan, S. Pal, Y. Zhang, and O. Gang, "Stoichiometric control of DNA-grafted colloid self-assembly," *Proceedings of the National Academy of Sciences*, vol. 112, pp. 4982–4987, 2015.

[123] N. Hunt, R. Jardine, and P. Bartlett, "Superlattice formation in mixtures of hard-sphere colloids," *Phys. Rev. E*, vol. 62, pp. 900–913, 2000.

[124] A. Travesset, "Topological Structure Prediction in Binary Nanoparticle Superlattices," *Soft Matter*, vol. 13, pp. 147–157, 2016.

[125] A. Travesset, "Soft Skyrmions, Spontaneous Valence and Selection Rules in Nanoparticle Superlattices," *ACS Nano*, vol. 11, pp. 5375–5382, 2017.

[126] B. Cabane, J. Li, F. Artzner, R. Botet, C. Labbez, G. Bareigts, M. Sztucki, and L. Goehring, "Hiding in Plain View: Colloidal Self-Assembly from Polydisperse Populations," *Phys. Rev. Lett.*, vol. 116, p. 208001, may 2016.

[127] T. S. Hudson and P. Harrowel, "Structural searches using isopointal sets as generators: densest packings for binary hard sphere mixtures," *J. Phys. Condens. Matter*, vol. 23, p. 194103, 2011.

[128] E. Jones, T. Oliphant, and Others, "Scipy: open source scientific tools for Python," 2001.

[129] D. J. Wales and J. P. K. Doye, "Global Optimization by Basin-Hopping and the Lowest Energy Structures of Lennard-Jones Clusters Containing up to 110 Atoms," *J. Phys. Chem. A*, vol. 101, pp. 5111–5116, 1997.

[130] C. Vega, E. Sanz, J. L. F. Abascal, and E. G. Noya, "Determination of phase diagrams via computer simulation: Methodology and applications to water, electrolytes and proteins," *Journal of Physics: Condensed Matter*, vol. 153101, p. 72, 2009.

[131] C. S. Adorf, J. Antonaglia, J. Dshemuchadse, and S. C. Glotzer, "Inverse design of simple pair potentials for the self-assembly of complex structures," *J. Chem. Phys.*, vol. 149, p. 204102, 11 2018.

[132] W. D. Piñeros, B. A. Lindquist, R. B. Jadrich, and T. M. Truskett, "Inverse design of multicomponent assemblies," *J. Chem. Phys.*, vol. 148, p. 104509, 3 2018.

[133] Z. M. Sherman, M. P. Howard, B. A. Lindquist, R. B. Jadrich, and T. M. Truskett, "Inverse methods for design of soft materials," *J. Chem. Phys.*, vol. 152, p. 140902, 4 2020.

[134] E. Pretti, H. Zerze, M. Song, Y. Ding, N. A. Mahynski, H. W. Hatch, V. K. Shen, and J. Mittal, "Assembly of three-dimensional binary superlattices from multi-flavored particles," *Soft Matter*, vol. 14, no. 30, pp. 6303–6312, 2018.

[135] N. A. Mahynski, E. Pretti, V. K. Shen, and J. Mittal, "Using symmetry to elucidate the importance of stoichiometry in colloidal crystal assembly," *Nat. Commun.*, vol. 10, no. 1, p. 2028, 2019.

[136] Y. Geng, G. van Anders, P. M. Dodd, J. Dshemuchadse, and S. C. Glotzer, "Engineering entropy for the inverse design of colloidal crystals from hard shapes," *Sci. Adv.*, vol. 5, p. eaaw0514, jul 2019.

[137] W. Kob and H. C. Andersen, "Scaling Behavior in the β-Relaxation Regime of a Supercooled Lennard-Jones Mixture," *Phys. Rev. Lett.*, vol. 73, pp. 1376–1379, 9 1994.

[138] L. Berthier and G. Biroli, "Theoretical perspective on the glass transition and amorphous materials," *Rev. Mod. Phys.*, vol. 83, pp. 587–645, 6 2011.

[139] T. Dasgupta, G. M. Coli, and M. Dijkstra, "Tuning the Glass Transition: Enhanced Crystallization of the Laves Phases in Nearly Hard Spheres," *ACS Nano*, vol. 14, pp. 3957–3968, 4 2020.

[140] E. Sanz, C. Valeriani, D. Frenkel, and M. Dijkstra, "Evidence for out-of-equilibrium crystal nucleation in suspensions of oppositely charged colloids," *Phys. Rev. Lett.*, vol. 99, no. 5, pp. 1–4, 2007.

[141] R. T. Scarlett, M. T. Ung, J. C. Crocker, and T. Sinno, "A mechanistic view of binary colloidal superlattice formation using DNA-directed interactions," *Soft Matter*, vol. 7, no. 5, pp. 1912–1925, 2011.

[142] P. Bartlett, "A model for the freezing of binary colloidal hard spheres," *J. Condens. Matter Phys.*, vol. 2, no. 22, pp. 4979–4989, 1990.

[143] C. P. Royall, W. C. K. Poon, and E. R. Weeks, "In search of colloidal hard spheres," *Soft Matter*, vol. 9, pp. 17–27, 2012.

[144] D. Coslovich, M. Ozawa, and L. Berthier, "Local order and crystallization of dense polydisperse hard spheres," *J. Condens. Matter Phys.*, vol. 30, no. 14, p. 144004, 2018.

[145] P. K. Bommineni, M. Klement, and M. Engel, "Spontaneous Crystallization in Systems of Binary Hard Sphere Colloids," *Phys. Rev. Lett.*, vol. 124, p. 218003, 5 2020.

[146] M. R. Khadilkar and F. A. Escobedo, "Self-assembly of binary space-tessellating compounds," *J. Chem. Phys.*, vol. 137, p. 194907, 11 2012.

[147] G. M. Coli and M. Dijkstra, "An Artificial Neural Network Reveals the Nucleation Mechanism of a Binary Colloidal AB13 Crystal," *ACS Nano*, 2 2021.

[148] J. A. Anderson, J. Glaser, and S. C. Glotzer, "HOOMD-blue: A Python package for high-performance molecular dynamics and hard particle Monte Carlo simulations," *Comput. Mater. Sci.*, vol. 173, p. 109363, feb 2020.

[149] V. Ramasubramani, B. D. Dice, E. S. Harper, M. P. Spellings, J. A. Anderson, and S. C. Glotzer, "freud: A software suite for high throughput analysis of particle simulation data," *Comput. Phys. Commun.*, vol. 254, p. 107275, 9 2020.

[150] G. C. Sosso, J. Chen, S. J. Cox, M. Fitzner, P. Pedevilla, A. Zen, and A. Michaelides, "Crystal Nucleation in Liquids: Open Questions and Future Challenges in Molecular Dynamics Simulations," *Chemical Reviews*, vol. 116, pp. 7078–7116, jun 2016.

[151] P. K. Bommineni, N. R. Varela-Rosales, M. Klement, and M. Engel, "Complex Crystals from Size-Disperse Spheres.," *Phys. Rev. Lett.*, vol. 122, p. 128005, 3 2019.

[152] F. A. Escobedo, "Effect of inter-species selective interactions on the thermodynamics and nucleation free-energy barriers of a tessellating polyhedral compound," *J. Chem. Phys.*, vol. 145, p. 211903, 11 2016.

[153] J. A. Anderson, M. Eric Irrgang, and S. C. Glotzer, "Scalable Metropolis Monte Carlo for simulation of hard shapes," *Comput. Phys. Commun*, vol. 204, pp. 21–30, sep 2016.

[154] V. Ramasubramani, T. Vo, J. A. Anderson, and S. C. Glotzer, "A mean-field approach to simulating anisotropic particles," *J. Chem. Phys.*, vol. 153, no. 8, p. 084106, 2020.

[155] G. J. Martyna, D. J. Tobias, and M. L. Klein, "Constant pressure molecular dynamics algorithms," *J. Chem. Phys.*, vol. 101, pp. 4177–4189, 11 1994.

[156] C. L. Phillips, J. A. Anderson, and S. C. Glotzer, "Pseudo-random number generation for Brownian Dynamics and Dissipative Particle Dynamics simulations on GPU devices," *J. Comput. Phys.*, vol. 230, no. 19, pp. 7191–7201, 2011.

[157] P. J. Steinhardt, D. R. Nelson, and M. Ronchetti, "Bond-orientational order in liquids and glasses," *Phys. Rev. B*, vol. 28, pp. 784–805, 7 1983.

[158] G. Konstantatos, I. Howard, A. Fischer, S. Hoogland, J. Clifford, E. Klem, L. Levina, and E. H. Sargent, "Ultrasensitive solution-cast quantum dot photodetectors," *Nature*, vol. 442, no. 7099, pp. 180–183, 2006.

[159] X. Tang, M. M. Ackerman, M. Chen, and P. Guyot-Sionnest, "Dual-band infrared imaging using stacked colloidal quantum dot photodiodes," *Nature Photonics*, vol. 13, no. 4, pp. 277–282, 2019.

[160] J. M. Caruge, J. E. Halpert, V. Wood, V. Bulović, and M. G. Bawendi, "Colloidal quantum-dot light-emitting diodes with metal-oxide charge transport layers," *Nature Photonics*, vol. 2, no. 4, pp. 247–250, 2008.

[161] T. Kim, K.-H. Kim, S. Kim, S.-M. Choi, H. Jang, H.-K. Seo, H. Lee, D.-Y. Chung, and E. Jang, "Efficient and stable blue quantum dot light-emitting diode.," *Nature*, vol. 586, pp. 385–389, oct 2020.

[162] D. V. Talapin and C. B. Murray, "PbSe nanocrystal solids for n- and p-channel thin film field-effect transistors.," *Science (New York, N.Y.)*, vol. 310, pp. 86–89, oct 2005.

[163] Q. Zhao, G. Gouget, J. Guo, S. Yang, T. Zhao, D. B. Straus, C. Qian, N. Oh, H. Wang, C. B. Murray, and C. R. Kagan, "Enhanced Carrier Transport in Strongly Coupled, Epitaxially Fused CdSe Nanocrystal Solids," *Nano Letters*, vol. 21, pp. 3318–3324, apr 2021.

[164] J. M. Luther, M. Law, M. C. Beard, Q. Song, M. O. Reese, R. J. Ellingson, and A. J. Nozik, "Schottky Solar Cells Based on Colloidal Nanocrystal Films," *Nano Letters*, vol. 8, pp. 3488–3492, oct 2008.

[165] A. Swarnkar, A. R. Marshall, E. M. Sanehira, B. D. Chernomordik, D. T. Moore, J. A. Christians, T. Chakrabarti, and J. M. Luther, "Quantum dot-induced phase stabilization of α-CsPbI3 perovskite for high-efficiency photovoltaics.," *Science (New York, N.Y.)*, vol. 354, pp. 92–95, oct 2016.

[166] X. Lan, M. Chen, M. H. Hudson, V. Kamysbayev, Y. Wang, P. Guyot-Sionnest, and D. V. Talapin, "Quantum dot solids showing state-resolved band-like transport.," *Nature materials*, vol. 19, pp. 323–329, mar 2020.

[167] N. S. Mueller, Y. Okamura, B. G. M. Vieira, S. Juergensen, H. Lange, E. B. Barros, F. Schulz, and S. Reich, "Deep strong light–matter coupling in plasmonic nanoparticle crystals," *Nature*, vol. 583, no. 7818, pp. 780–784, 2020.

[168] I. Cherniukh, G. Rainò, T. Stöferle, M. Burian, A. Travesset, D. Naumenko, H. Amenitsch, R. Erni, R. F. Mahrt, M. I. Bodnarchuk, and M. V. Kovalenko, "Perovskite-type superlattices from lead halide perovskite nanocubes.," *Nature*, vol. 593, pp. 535–542, may 2021.

[169] J. Chen, A. Dong, J. Cai, X. Ye, Y. Kang, J. M. Kikkawa, and C. B. Murray, "Collective dipolar interactions in self-assembled magnetic binary nanocrystal superlattice membranes.," *Nano letters*, vol. 10, pp. 5103–5108, dec 2010.

[170] A. Dong, J. Chen, X. Ye, J. M. Kikkawa, and C. B. Murray, "Enhanced Thermal Stability and Magnetic Properties in NaCl-Type FePt–MnO Binary Nanocrystal Superlattices," *Journal of the American Chemical Society*, vol. 133, pp. 13296–13299, aug 2011.

[171] M. Zhang, D. J. Magagnosc, I. Liberal, Y. Yu, H. Yun, H. Yang, Y. Wu, J. Guo, W. Chen, Y. J. Shin, A. Stein, J. M. Kikkawa, N. Engheta, D. S. Gianola, C. B. Murray, and C. R. Kagan, "High-strength magnetically switchable plasmonic nanorods assembled from a binary nanocrystal mixture," *Nature Nanotechnology*, vol. 12, no. 3, pp. 228–232, 2017.

[172] M. Cargnello, A. C. Johnston-Peck, B. T. Diroll, E. Wong, B. Datta, D. Damodhar, V. V. T. Doan-Nguyen, A. A. Herzing, C. R. Kagan, and C. B. Murray, "Substitutional doping in nanocrystal superlattices.," *Nature*, vol. 524, pp. 450–453, aug 2015.

[173] J.-S. Lee, M. V. Kovalenko, J. Huang, D. S. Chung, and D. V. Talapin, "Band-like transport, high electron mobility and high photoconductivity in all-inorganic nanocrystal arrays.," apr 2011.

[174] C. M. Heil and A. Jayaraman, "Computational Reverse-Engineering Analysis for Scattering Experiments of Assembled Binary Mixture of Nanoparticles," *ACS Materials Au*, vol. 1, pp. 140–156, nov 2021.

[175] D. Wang, T. Dasgupta, E. B. van der Wee, D. Zanaga, T. Altantzis, Y. Wu, G. M. Coli, C. B. Murray, S. Bals, M. Dijkstra, and A. van Blaaderen, "Binary icosahedral clusters of hard spheres in spherical confinement," *Nature Physics*, vol. 17, no. 1, pp. 128–134, 2021.

[176] E. Marino, T. E. Kodger, G. H. Wegdam, and P. Schall, "Revealing Driving Forces in Quantum Dot Supercrystal Assembly," *Advanced Materials*, vol. 30, p. 1803433, oct 2018.

[177] F. Montanarella, J. J. Geuchies, T. Dasgupta, P. T. Prins, C. van Overbeek, R. Dattani, P. Baesjou, M. Dijkstra, A. V. Petukhov, A. van Blaaderen, and D. Vanmaekelbergh, "Crystallization of Nanocrystals in Spherical Confinement Probed by in Situ X-ray Scattering," *Nano Letters*, vol. 18, pp. 3675–3681, jun 2018.

[178] M. C. Weidman, D.-M. Smilgies, and W. A. Tisdale, "Kinetics of the self-assembly of nanocrystal superlattices measured by real-time in situ X-ray scattering.," *Nature materials*, vol. 15, pp. 775–781, jul 2016.

[179] J. J. Geuchies, C. van Overbeek, W. H. Evers, B. Goris, A. de Backer, A. P. Gantapara, F. T. Rabouw, J. Hilhorst, J. L. Peters, O. Konovalov, A. V. Petukhov, M. Dijkstra, L. D. A. Siebbeles, S. van Aert, S. Bals, and D. Vanmaekelbergh, "In situ study of the formation mechanism of two-dimensional superlattices from PbSe nanocrystals.," *Nature materials*, vol. 15, pp. 1248–1254, dec 2016.

[180] B. Abécassis, F. Testard, and O. Spalla, "Gold Nanoparticle Superlattice Crystallization Probed In Situ," *Phys. Rev. Lett.*, vol. 100, p. 115504, mar 2008.

[181] S. Narayanan, J. Wang, and X.-M. Lin, "Dynamical Self-Assembly of Nanocrystal Superlattices during Colloidal Droplet Evaporation by in situ Small Angle X-Ray Scattering," *Phys. Rev. Lett.*, vol. 93, p. 135503, sep 2004.

[182] S. Connolly, S. Fullam, B. Korgel, and D. Fitzmaurice, "Time-Resolved Small-Angle X-ray Scattering Studies of Nanocrystal Superlattice Self-Assembly," *Journal of the American Chemical Society*, vol. 120, pp. 2969–2970, apr 1998.

[183] Y. Yu, D. Yu, B. Sadigh, and C. A. Orme, "Space- and time-resolved small angle X-ray scattering to probe assembly of silver nanocrystal superlattices," *Nature Communications*, vol. 9, no. 1, p. 4211, 2018.

[184] L. Wu, J. J. Willis, I. S. McKay, B. T. Diroll, J. Qin, M. Cargnello, and C. J. Tassone, "High-temperature crystallization of nanocrystals into three-dimensional superlattices," *Nature*, vol. 548, no. 7666, pp. 197–201, 2017.

[185] J. Gong, R. S. Newman, M. Engel, M. Zhao, F. Bian, S. C. Glotzer, and Z. Tang, "Shape-dependent ordering of gold nanocrystals into large-scale superlattices," *Nature Communications*, vol. 8, no. 1, p. 14038, 2017.

[186] K. Yue, M. Huang, R. L. Marson, J. He, J. Huang, Z. Zhou, J. Wang, C. Liu, X. Yan, K. Wu, Z. Guo, H. Liu, W. Zhang, P. Ni, C. Wesdemiotis, W.-B. Zhang, S. C. Glotzer, and S. Z. D. Cheng, "Geometry induced sequence of nanoscale Frank–Kasper and quasicrystal mesophases in giant surfactants," *Proceedings of the National Academy of Sciences*, vol. 113, pp. 14195 LP – 14200, dec 2016.

[187] C. Lu, A. J. Akey, C. J. Dahlman, D. Zhang, and I. P. Herman, "Resolving the Growth of 3D Colloidal Nanoparticle Superlattices by Real-Time Small-Angle X-ray Scattering," *Journal of the American Chemical Society*, vol. 134, pp. 18732–18738, nov 2012.

[188] B. de Nijs, S. Dussi, F. Smallenburg, J. D. Meeldijk, D. J. Groenendijk, L. Filion, A. Imhof, A. van Blaaderen, and M. Dijkstra, "Entropy-driven formation of large icosahedral colloidal clusters by spherical confinement.," *Nature materials*, vol. 14, pp. 56–60, jan 2015.

[189] A. Abelson, C. Qian, T. Salk, Z. Luan, K. Fu, J.-G. Zheng, J. L. Wardini, and M. Law, "Collective topo-epitaxy in the self-assembly of a 3D quantum dot superlattice," *Nature Materials*, vol. 19, no. 1, pp. 49–55, 2020.

[190] O. D. Velev, A. M. Lenhoff, and E. W. Kaler, "A class of microstructured particles through colloidal crystallization," *Science*, vol. 287, no. 5461, pp. 2240–2243, 2000.

[191] A. L. Patterson, "The Scherrer Formula for X-Ray Particle Size Determination," *Phys. Rev.*, vol. 56, pp. 978–982, nov 1939.

[192] E. Marino, A. W. Keller, D. An, S. van Dongen, T. E. Kodger, K. E. MacArthur, M. Heggen, C. R. Kagan, C. B. Murray, and P. Schall, "Favoring the Growth of High-Quality, Three-Dimensional Supercrystals of Nanocrystals," *The Journal of Physical Chemistry C*, vol. 124, pp. 11256–11264, may 2020.

[193] Z. Yang, J. Wei, and M.-P. Pileni, "Metal–Metal binary nanoparticle superlattices: a case study of mixing Co and Ag nanoparticles," *Chemistry of Materials*, vol. 27, no. 6, pp. 2152–2157, 2015.

[194] Z. Chen and S. O'Brien, "Structure direction of II VI semiconductor quantum dot binary nanoparticle superlattices by tuning radius ratio," *Acs Nano*, vol. 2, no. 6, pp. 1219–1229, 2008.

[195] K. J. M. Bishop, C. E. Wilmer, S. Soh, and B. A. Grzybowski, "Nanoscale Forces and Their Uses in Self-Assembly," *Small*, vol. 5, pp. 1600–1630, jul 2009.

[196] P. Schapotschnikow, R. Pool, and T. J. H. Vlugt, "Molecular simulations of interacting nanocrystals," *Nano Letters*, vol. 8, no. 9, pp. 2930–2934, 2008.

[197] C. Liepold, A. Smith, B. Lin, J. de Pablo, and S. A. Rice, "Pair and many-body interactions between ligated Au nanoparticles," *The Journal of Chemical Physics*, vol. 150, p. 44904, jan 2019.

[198] Ł. Baran and S. Sokołowski, "Effective interactions between a pair of particles modified with tethered chains," *The Journal of Chemical Physics*, vol. 147, p. 44903, jul 2017.

[199] G. Munaò, A. Correa, A. Pizzirusso, and G. Milano, "On the calculation of the potential of mean force between atomistic nanoparticles," *The European Physical Journal E*, vol. 41, no. 3, p. 38, 2018.

[200] T. Kister, D. Monego, P. Mulvaney, A. Widmer-Cooper, and T. Kraus, "Colloidal stability of apolar nanoparticles: the role of particle size and ligand shell structure," *ACS nano*, vol. 12, no. 6, pp. 5969–5977, 2018.

[201] G. Mie, "Zur kinetischen Theorie der einatomigen Körper," *Annalen der Physik*, vol. 316, no. 8, pp. 657–697, 1903.

[202] M. G. Noro and D. Frenkel, "Extended corresponding-states behavior for particles with variable range attractions," *The Journal of Chemical Physics*, vol. 113, pp. 2941–2944, aug 2000.

[203] P. R. ten Wolde and D. Frenkel, "Enhancement of protein crystal nucleation by critical density fluctuations," *Science*, vol. 277, no. 5334, pp. 1975–1978, 1997.

[204] L. Xu, S. V. Buldyrev, H. E. Stanley, and G. Franzese, "Homogeneous crystal nucleation near a metastable fluid-fluid phase transition.," *Physical review letters*, vol. 109, p. 95702, aug 2012.

[205] J. Wedekind, L. Xu, S. V. Buldyrev, H. E. Stanley, D. Reguera, and G. Franzese, "Optimization of crystal nucleation close to a metastable fluid-fluid phase transition," *Scientific Reports*, vol. 5, no. 1, p. 11260, 2015.

[206] F. Romano, E. Sanz, and F. Sciortino, "Crystallization of tetrahedral patchy particles in silico.," *The Journal of chemical physics*, vol. 134, p. 174502, may 2011.

[207] J. D. Weeks, D. Chandler, and H. C. Andersen, "Role of Repulsive Forces in Determining the Equilibrium Structure of Simple Liquids," *The Journal of Chemical Physics*, vol. 54, pp. 5237–5247, jun 1971.

[208] J. A. Barker and D. Henderson, "What is "liquid"? Understanding the states of matter," *Rev. Mod. Phys.*, vol. 48, pp. 587–671, oct 1976.

[209] F. Lu, K. G. Yager, Y. Zhang, H. Xin, and O. Gang, "Superlattices assembled through shape-induced directional binding," *Nature Communications*, vol. 6, p. 6912, apr 2015.

[210] F. Romano and F. Sciortino, "Patterning symmetry in the rational design of colloidal crystals," *Nature Communications*, vol. 3, no. 1, p. 975, 2012.

[211] Y. Wang, Y. Wang, D. R. Breed, V. N. Manoharan, L. Feng, A. D. Hollingsworth, M. Weck, and D. J. Pine, "Colloids with valence and specific directional bonding.," *Nature*, vol. 491, pp. 51–5, nov 2012.

[212] A. W. Long and A. L. Ferguson, "Nonlinear machine learning of patchy colloid self-assembly pathways and mechanisms," *The Journal of Physical Chemistry B*, vol. 118, no. 15, pp. 4228–4244, 2014.

[213] A. V. Tkachenko, "Generic phase diagram of binary superlattices," *Proceedings of the National Academy of Sciences*, vol. 113, no. 37, pp. 10269–10274, 2016.

[214] L. Filion, M. Hermes, R. Ni, E. C. M. Vermolen, A. Kuijk, C. G. Christova, J. C. P. Stiefelhagen, T. Vissers, A. Van Blaaderen, and M. Dijkstra, "Self-assembly of a colloidal interstitial solid with tunable sublattice doping," *Physical review letters*, vol. 107, no. 16, p. 168302, 2011.

[215] L. Pauling, "THE PRINCIPLES DETERMINING THE STRUCTURE OF COMPLEX IONIC CRYSTALS," *Journal of the American Chemical Society*, vol. 51, pp. 1010–1026, apr 1929.

[216] Z. Yang, J. Wei, P. Bonville, and M.-P. Pileni, "Beyond Entropy: Magnetic Forces Induce Formation of Quasicrystalline Structure in Binary Nanocrystal Superlattices," *Journal of the American Chemical Society*, vol. 137, pp. 4487–4493, apr 2015.

[217] I. Coropceanu, M. A. Boles, and D. V. Talapin, "Systematic mapping of binary nanocrystal superlattices: The role of topology in phase selection," *Journal of the American Chemical Society*, vol. 141, no. 14, pp. 5728–5740, 2019.

[218] D. Jishkariani, Y. Wu, D. Wang, Y. Liu, A. van Blaaderen, and C. B. Murray, "Preparation and Self-Assembly of Dendronized Janus Fe3O4–Pt and Fe3O4–Au Heterodimers," *ACS Nano*, vol. 11, pp. 7958–7966, aug 2017.

[219] H. Zhu, Z. Fan, Y. Yuan, M. A. Wilson, K. Hills-Kimball, Z. Wei, J. He, R. Li, M. Grunwald, and O. Chen, "Self-assembly of quantum dot–gold heterodimer nanocrystals with orientational order," *Nano letters*, vol. 18, no. 8, pp. 5049–5056, 2018.

[220] I. L. Medintz, H. T. Uyeda, E. R. Goldman, and H. Mattoussi, "Quantum dot bioconjugates for imaging, labelling and sensing," *Nature materials*, vol. 4, no. 6, pp. 435–446, 2005.

[221] H. Yu, M. Chen, P. M. Rice, S. X. Wang, R. L. White, and S. Sun, "Dumbbell-like bifunctional Au Fe3O4 nanoparticles," *Nano letters*, vol. 5, no. 2, pp. 379–382, 2005.

[222] J. Gao, H. Gu, and B. Xu, "Multifunctional Magnetic Nanoparticles: Design, Synthesis, and Biomedical Applications," *Accounts of Chemical Research*, vol. 42, pp. 1097–1107, aug 2009.

[223] G. Jiang, Y. Huang, S. Zhang, H. Zhu, Z. Wu, and S. Sun, "Controlled synthesis of Au–Fe heterodimer nanoparticles and their conversion into Au–Fe 3 O 4 heterostructured nanoparticles," *Nanoscale*, vol. 8, no. 41, pp. 17947–17952, 2016.

[224] A. Saric, B. Bozorgui, and A. Cacciuto, "Packing of soft asymmetric dumbbells," *The Journal of Physical Chemistry B*, vol. 115, no. 22, pp. 7182–7189, 2011.

[225] M. Dennison, K. Milinković, and M. Dijkstra, "Phase diagram of hard snowman-shaped particles," *The Journal of chemical physics*, vol. 137, no. 4, p. 44507, 2012.

[226] K. Milinković, M. Dennison, and M. Dijkstra, "Phase diagram of hard asymmetric dumbbell particles," *Physical Review E*, vol. 87, no. 3, p. 32128, 2013.

[227] K. Whitham, J. Yang, B. H. Savitzky, L. F. Kourkoutis, F. Wise, and T. Hanrath, "Charge transport and localization in atomically coherent quantum dot solids," *Nature Materials*, vol. 15, no. 5, pp. 557–563, 2016.

[228] L. Filion, R. Ni, D. Frenkel, and M. Dijkstra, "Simulation of nucleation in almost hard-sphere colloids: The discrepancy between experiment and simulation persists," *The Journal of Chemical Physics*, vol. 134, p. 134901, apr 2011.

[229] A. J. Page, T. Isomoto, J. M. Knaup, S. Irle, and K. Morokuma, "Effects of Molecular Dynamics Thermostats on Descriptions of Chemical Nonequilibrium," *Journal of Chemical Theory and Computation*, vol. 8, pp. 4019–4028, nov 2012.

[230] L. Filion, M. Hermes, R. Ni, and M. Dijkstra, "Crystal nucleation of hard spheres using molecular dynamics, umbrella sampling, and forward flux sampling: A comparison of simulation techniques," *The Journal of Chemical Physics*, vol. 133, p. 244115, dec 2010.

[231] W. G. Hoover, "Canonical dynamics: Equilibrium phase-space distributions," *Phys. Rev. A*, vol. 31, pp. 1695–1697, mar 1985.

[232] J. Wedekind, R. Strey, and D. Reguera, "New method to analyze simulations of activated processes," *The Journal of Chemical Physics*, vol. 126, p. 134103, apr 2007.